



UNIVERSITÀ DI PAVIA
DIPARTIMENTO DI FISICA



SCUOLA DI DOTTORATO DI RICERCA IN FISICA
XXXIV CICLO

**Experimental and computational studies
for an Accelerator-Based Boron Neutron
Capture Therapy clinical facility:
a multidisciplinary approach**

Dissertation submitted by
CHIARA MAGNI

*Submitted to the Graduate School of Physics in partial fulfillment of
the requirements for the degree of
DOTTORE DI RICERCA IN FISICA
DOCTOR OF PHILOSOPHY IN PHYSICS
at the University of Pavia*

Supervisor

PROF. SILVA BORTOLUSSI

Referees

PROF. IGNACIO PORRAS & DR. GUSTAVO A. SANTA CRUZ

Abstract

The work described in this thesis has been carried out in the field of AB-BNCT, Accelerator-Based Boron Neutron Capture Therapy. BNCT is a binary radiotherapy combining the loading of tumour with boron-10 and its subsequent irradiation with low energy neutrons, exploiting the high cross section of neutron capture in boron-10. With a selective accumulation of boron-10 in the tumour by a suitable borated drug, the products of the reaction release a therapeutic dose in the tumour while sparing the surrounding healthy tissues. This biological selectivity makes BNCT a promising therapy for the treatment of diffuse, infiltrated or metastatic tumors.

Recently, the possibility to obtain suitable neutron beams from accelerators has opened a new frontier: AB-BNCT could now become accessible in many hospitals, with improvements in quality of life and clinical outcome for several patients.

The context of this work is the design of a clinical BNCT facility based on a Radio Frequency Quadrupole proton accelerator, manufactured by the Italian National Institute of Nuclear Physics (INFN). Such machine can provide a neutron beam suitable for the treatment of deep-seated tumors when coupled to a beryllium target and a Beam Shaping Assembly whose main constituent is solid lithiated aluminum fluoride. *Alliflu*, densified lithiated aluminum fluoride, is a new material created on purpose at the University and INFN of Pavia through an innovative sintering process on powders of lithium and aluminum fluoride.

The work here presented aimed to cover different aspects from the installation of the facility to its clinical applications, and is characterized by a multidisciplinary approach: it includes studies in the field of material science and engineering for the production and analysis of the new material, computational and experimental nuclear physics for the validation of its moderation properties, radiation protection evaluations for the design of an optimized treatment room, and finally a medical physics application consisting in the treatment planning of a realistic clinical case.

This work presents a contribution to the implementation of a AB-BNCT facility, demonstrating that R&D has great potential to optimize BNCT quality and to promote a new era of clinical applications.

Contents

1	Introduction	1
1.1	Boron Neutron Capture Therapy	1
1.2	Accelerator-based BNCT	4
1.3	Summary of the thesis	6
2	A new neutron moderator: Alliflu	11
2.1	Preliminary studies	14
2.1.1	Neutron activation of the BSA core	17
2.1.2	Density	19
2.1.3	Water absorption and solubility	21
2.2	Morphology	23
2.3	Mechanical resistance	33
2.3.1	First round of measurements	36
2.3.2	Second round of measurements	37
3	Spectrum modification by Alliflu	43
3.1	Materials and methods	43
3.2	Measurements with <i>Alliflu</i> tiles	45
3.2.1	First experimental campaign	46
3.2.2	Second experimental campaign	49
3.3	Measurements with BSA prototype	50
3.3.1	BSA prototype: final configuration	52
4	Treatment room	59
4.1	Neutron activation of the air	60
4.2	Neutron activation of the walls	62
4.3	Neutron activation of the patient	66
4.3.1	Residual radioactivity of urine	66
4.3.2	Residual radioactivity of soft tissue	67

4.4	Patient out-of-field dosimetry	68
4.4.1	Radiation-induced cardiovascular diseases	70
4.5	In-air dosimetry	72
4.5.1	Equivalent dose	73
4.5.2	Ambient dose equivalent	73
4.5.3	Dose from neutron activation	77
4.5.4	Shielding design for residual dose	77
5	Clinical applications	85
5.1	Hadrontherapy with carbon ions	85
5.2	Comparison and combination of BNCT and ¹² C treatments . . .	88
5.2.1	Photon iso-effective dose	91
5.2.2	The IT_STARTS toolkit	92
5.3	Treatment Planning, Dosimetry and TCP calculation criteria . . .	93
5.4	First scenario	95
5.5	Second scenario	98
5.6	Third scenario	100
6	Conclusions and Perspectives	103
	Appendices	106
A	TT_Sinter	109
A.1	Machine overview	111
A.2	Commissioning and tests	114
A.3	Other applications	117
B	BSA prototype	123
B.1	First configuration	123
B.2	Second configuration	127
B.3	Third configuration	131
B.4	Summary and final configuration	138
	Bibliography	140
	List of Publications	155

Introduction

The World Health Organization defines cancer as the second leading cause of death globally [1], responsible for nearly 10 million deaths in the year 2020 (Figure 1.1). According to statistical studies based on US data for the 2015-17 period, about 39.5% of the world population will be diagnosed with cancer at some point in the lifetime [2]. Despite the efforts of medicine, these numbers are destined to rise: by 2040, the number of new cancer diagnoses per year is estimated to reach 29.5 million, and the number of deaths due to it 16.4 million [3]. Nevertheless, thanks to advances in research, promising new techniques have emerged in recent years in the fight against cancer, including unconventional radiotherapy such as hadrontherapy, which exploits the mechanism of energy deposition of the charged particles to deliver a precise and effective dose to the tumour. Charged particles, in fact, deposit the majority of their energy at the end of their path, thus concentrating the dose delivery in the target. Moreover, charged particles are more effective in causing non-reparable damages to the cells, because their interaction in matter is characterised by clustered ionization. Another unconventional modality of radiation therapy is Boron Neutron Capture Therapy, which has shown great potential on a number of oncological diseases.

1.1 Boron Neutron Capture Therapy

Boron Neutron Capture Therapy (BNCT) is an experimental, non-invasive form of radiotherapy for the treatment of cancer [4]. It is a binary modality, based on the synergistic action of a tumour-targeting boron-enriched drug and irradiation with low energy neutrons. BNCT exploits the high cross section of boron-10 (^{10}B), the stable isotope of boron with 19.9% natural abundance, for the capture of *thermal* neutrons, i.e. neutrons with kinetic energy of 0.025 eV, the most probable value at a temperature of 290 K or about 17°C.

Neutron capture [5] is the nuclear reaction that occurs when an atomic nucleus and a neutron merge, forming a heavier nucleus:



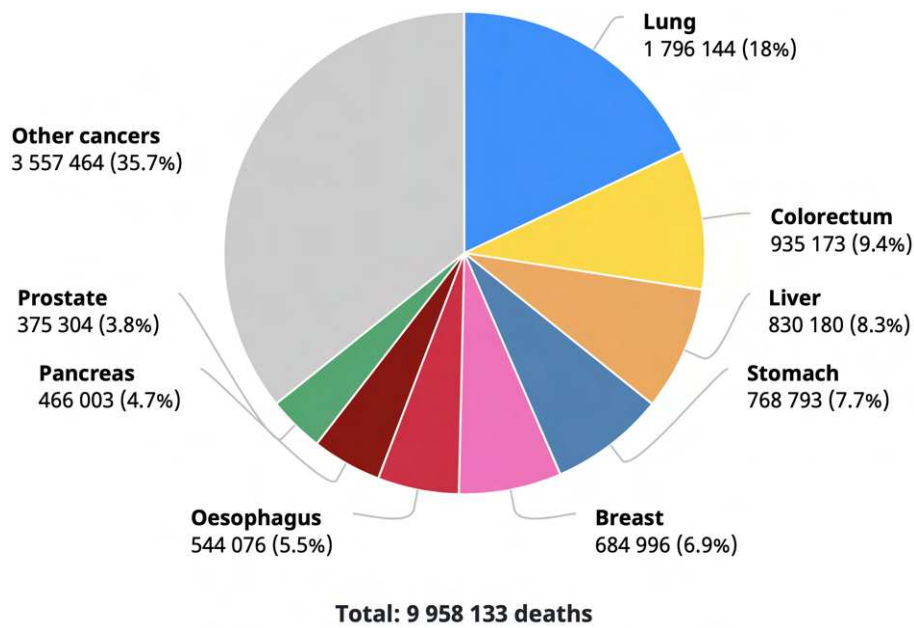


Figure 1.1: Cancer deaths in 2020 for both sexes and all ages, from [1]

The final nucleus subsequently decays by emitting charged particles, whose energy depends on the Q-value of the reaction. The possibility to use neutron capture reactions to treat cancer was first theorized by the physicist Gordon Locher in 1936, just four years after the discovery of the neutron by James Chadwick. Therapies based on neutron capture can be extremely selective, especially when the reaction leads to the creation of charged particles with high LET (Linear Energy Transfer¹) and short ranges in biological tissues. The energy deposited by such particles is high in a limited region of space, within distances comparable with the diameter of a typical cell. As a consequence, neutron capture therapy can be described as an internal hadrontherapy, played by the charged particles created inside the cancer cell. Ideally, the energy deposition is confined within the target cell without affecting the surrounding healthy tissue, enabling a radiotherapy characterized by a cell-level selectivity.

The BNCT treatment is carried out in two steps. First, the patient receives an intravenous infusion of the borated compound designed to accumulate in cancer cells [6]. Then, after a certain time necessary to ensure the best ^{10}B tumour-to-normal tissue concentration ratio, the cancer region is irradiated with a neutron beam of suitable energy spectrum. The probability that a thermal neutron is captured in ^{10}B is much higher compared to the other possible interactions of neutrons with the elements of biological tissue: the neutron capture in ^{10}B has a microscopic cross section of 3837 barns^2 at 0.025 eV , about 2000 times the cross section of the capture in ^{14}N (Table 1.1).

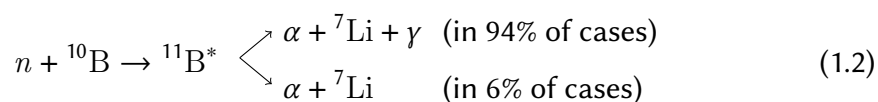
¹LET is the average amount of energy transferred by an ionizing particle per unit path length.

²Nuclear cross sections are usually expressed in terms of barns, with $1 \text{ barn} = 10^{-24} \text{ cm}^2$.

Table 1.1: Thermal neutron capture cross-sections of biological soft tissue elements and their mass percentages [7]

Nuclide	Mass %	σ (b)	Nuclide	Mass %	σ (b)
H	10.0	0.332	P	1.16	0.18
C	18.0	0.0034	S	0.20	0.53
N	3.0	1.82	Cl	0.16	32.68
O	65.0	1.8×10^{-4}	K	0.20	2.1
Na	0.11	0.43	Ca	2.01	0.4
Mg	0.04	0.053	Fe	0.01	2.57

The neutron capture reaction in ^{10}B leads to the generation of $^{11}\text{B}^*$, unstable, which can decay following two different modalities:



In all cases, an alpha particle and a lithium ion are produced, having high ionization density values (164 and 151 keV/um, respectively, averaged over track intersection segments with the cell), and short ranges in tissue (9 and 5 μm , respectively). Being these ranges comparable with the average cellular diameter, the particles will deposit their energy in the cell hosting the reaction causing irreversible damages to the DNA. Given the higher concentration of boron-10 in tumour cells with respect to healthy tissues, the overall effect is the selective deposition of a therapeutic dose in the tumour while sparing the surrounding normal cells. Thanks to this selective effect, based on biological targeting rather than on beam targeting, BNCT is a potential therapeutic option for the treatment of disseminated, infiltrated or non-operable tumours [8].

The first application of BNCT was for the treatment of Glioblastoma Multiforme (GBM), or grade IV astrocytoma, a fast-growing brain tumour that invades the nearby brain tissue [9]. GBM is the most common and aggressive malignant primary brain tumour in humans and has a very poor prognosis, with the death of patients within 14 months from its diagnosis. Due to its resistance to conventional therapies, the migration of malignant cells into adjacent brain tissue and the limited capacity of the brain to repair itself, GBM presents unique treatment challenges.

The history of BNCT for the treatment of GBM began in USA in the '50s, and continued in Japan with the introduction of important innovations such as new borated drugs and the use of more penetrating neutron beams. The outcomes of the first treatments had indeed demonstrated the need for an optimization of both the borated drug and the neutron beam [10]. After several phases of BNCT

clinical research, today this therapeutic option is considered extremely promising, as proven by the work of Kawabata and colleagues, who recently treated 22 GBM patients in a phase II clinical trial at an irradiation facility in Japan [11].

BNCT has been proven an effective therapy not only for GBM but also for other challenging malignancies: recurrent head-and-neck cancer, gliomas, malignant melanomas and more [12]. From the first clinical trial of 1952 [13], BNCT has been performed on several hundred patients in different facilities around the world, and is now facing a new era. In fact, until recently, neutron beams from nuclear research reactors were used as neutron source for BNCT: only these installations allowed the neutron intensity needed for a BNCT irradiation lasting about 1 hour. At present, the latest developments in technology have led to a major turning point in BNCT with the possibility to obtain suitable beams for clinical BNCT using accelerators as neutron source.

1.2 Accelerator-based BNCT

While the typical sources of neutrons for BNCT treatments have been nuclear reactors, the current research in BNCT field is focusing on facilities based on accelerators. It is clearly not trivial to adapt a nuclear reactor to the needs of a clinical treatment, and many aspects such as safety, maintenance, social acceptability, made very difficult the development of BNCT as an established radiotherapy within such environment.

Instead, accelerators are easier to install and maintain also in healthcare settings. The availability of accelerators as neutron source for BNCT can lead to a wider application of this therapy, potentially even in hospital routine.

Thanks to recent technological progress, it is now possible to obtain proper clinical neutron beams for BNCT from high-current proton or deuteron accelerators [14]. Such machines can provide high-intensity neutron beams through the (p,n) or (d,n) reactions on beryllium or lithium targets. The optimal beam for BNCT treatment is obtained by filtering, collimating and moderating the neutron spectrum emerging from the target through the so-called BSA, Beam Shaping Assembly, an appropriately designed structure, built out of suitable materials.

In Italy, an accelerator with the characteristics for producing an intense neutron beam has been designed and manufactured by INFN, the National Institute of Nuclear Physics. It is a Radio Frequency Quadrupole (RFQ) proton accelerator capable to deliver 5 MeV protons with 30 mA current in Continuous Wave (CW) mode (Figure 1.2).

This accelerator coupled to a beryllium target produces neutrons through the reaction (p,n) on Be and can deliver a sufficient neutron flux for BNCT clinical treatments. A BSA (Figure 1.2) has been designed [15] to tailor a proper beam for BNCT of deep-seated tumours. The desired beam is epithermal, with energy spectrum peaked between 1 and 10 keV, so that neutrons can thermalize in the first layers of biological tissue and impinge on the tumour with the suitable energy for the neutron capture reaction. Such a beam still allows to treat also more superfi-

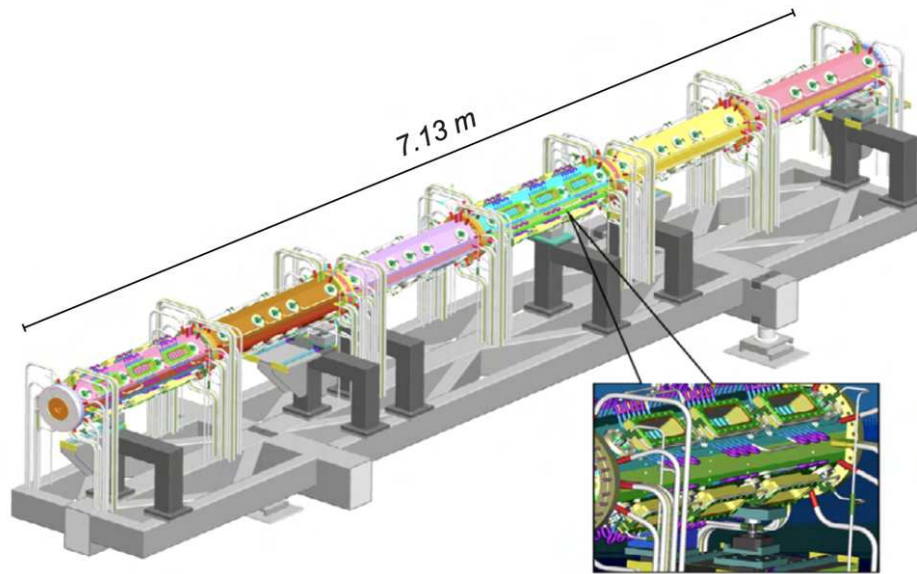


Figure 1.2: A scheme of the RFQ accelerator manufactured by INFN

cial tumours (e.g. melanoma), by moderating neutrons through the employ of a tissue-equivalent material, able to shift the neutron spectrum at the patient skin towards softer energies. The most appropriate material for the core of a BSA ensuring a final beam with the described characteristics has been demonstrated to be lithiated aluminum fluoride ($\text{AlF}_3 + \text{LiF}$) [15], represented in grey in Figure 1.3.

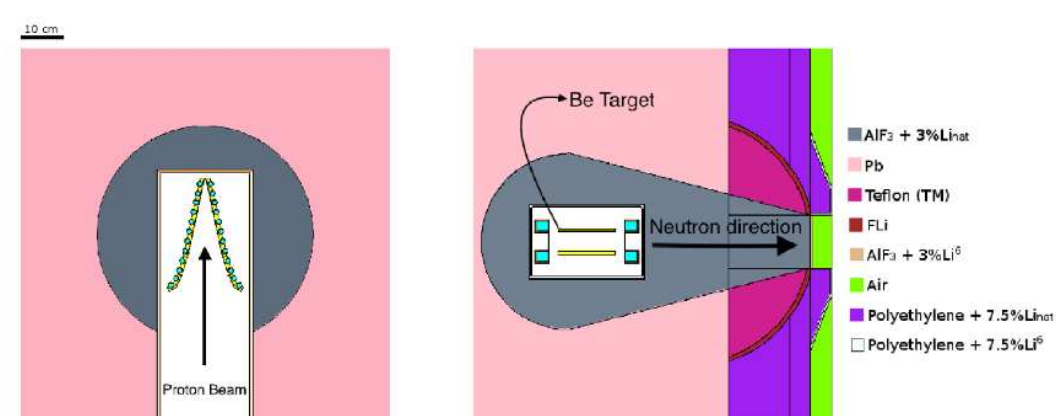


Figure 1.3: Geometry of the BSA designed for the INFN RFQ accelerator

This thesis collects the studies related to the installation and use of a clinical BNCT facility based on the INFN technology. The aim is to produce results useful for the structural and operational optimization of the facility and to anticipate its deployment by simulating realistic clinical treatments. This thesis contributes to the research on Accelerator-Based BNCT (AB-BNCT), particularly relevant today,

as many institutions in the world are dedicating efforts in building this type of facilities. Worldwide several projects are ongoing in this field, but as they are based on a variety of different machines and BSAs, a state-of-the-art is of difficult definition (Figure 1.4).

LOCATION	MACHINE, FACILITY STATUS	TARGET & REACTION
UNIVERSITY OF TSUKUBA, JAPAN	RFQ-DTL: UNDER DEVELOPMENT	BE(P,N)
KURRI, OSAKA MED COLLEGE, TOHOKU HOSPITAL, JAPAN	CYCLOTRON, CLINICAL TRIALS ONGOING	BE(P,N)
NCCENTER - CICS TOKYO, JAPAN	RFQ: UNDER DEVELOPMENT	SOLID $^7\text{Li}(P,N)$
NAGOYA UNIVERSITY, JAPAN	IBA DYNAMITRON, PURCHASED	LIQUID (STATIC) $^7\text{Li}(P,N)$
SOREQ, ISRAEL	RFQ-DTL: UNDER DEVELOPMENT	LIQUID (JET) $^7\text{Li}(P,N)$
BI, RUSSIA	VACUUM INSULATED TANDEM, UNDER DEVELOPMENT	SOLID $^7\text{Li}(P,N)$
CNEA, ARGENTINA	SINGLE ENDED ESQ, UNDER DEVELOPMENT & BUILDING CONSTRUCTION	BE(D,N) THIN $^{13}\text{C}(D,N)$ THICK
HUCH-NT, FINLAND+USA	SINGLE ENDED, DC, UNDER COMMISSIONING	SOLID $^7\text{Li}(P,N)$
BIRMINGHAM UNIVERSITY, UK	DYNAMITRON: UPGRADE DELAYED	SOLID $^7\text{Li}(P,N)$
IHEP, CHINA	RFQ, UNDER DEVELOPMENT	BE(P,N)
INFN, ITALY	RFQ, UNDER DEVELOPMENT	BE(P,N)
NEUBORON+TAE, CHINA+USA	TANDEM ELECTROSTATIC	SOLID $^7\text{Li}(P,N)$

Figure 1.4: A summary of the current projects on BNCT from accelerator

1.3 Summary of the thesis

The results presented in this thesis have been obtained in the context of a research project aimed at building a clinical facility using the RFQ accelerator, the beryllium target and the BSA designed on purpose. The work described in the following chapters contributes to the technological implementation of the BSA, the design of the treatment room and provides an original example of BNCT treatment using the described beam. The goal is to provide a comprehensive study, from preparation and characterization of the material for the BSA core, to dosimetric and neutron activation evaluations in the irradiation room, and finally to an innovative approach regarding the clinical applications of the facility.

The second and third Chapters are devoted to the studies carried out on the material chosen as main constituent of the BSA and developed for the first time in Pavia. In fact, aluminum fluoride only exists in powder, and it has been sintered with a dedicated machine designed and built in Pavia to obtain high-density solid bricks. The new material, consisting in sintered lithiated aluminium fluoride, was named *Alliflu*. From the first prototype of the sintering machine, a new improved version was designed and manufactured at the mechanical workshop of INFN Unit of Pavia. Part of this thesis is dedicated to the test of the new machine and its fine tuning for an optimized production of samples, as described in Appendix A. The densified material has been investigated in detail concerning

its physical characteristics and its moderation properties were studied comparing Monte Carlo simulations and experimental measurements. After a preliminary study aimed at evaluating and quantifying the presence of trace elements in the material, several sintered samples were obtained and analyzed regarding their internal structure, solubility and mechanical resistance. Different production procedures were tested to optimize the uniformity. After the production settings have been fixed, the moderation properties of *Alliflu* were tested in a neutron beam with the same spectral characteristics as the one produced by the RFQ. Finally, a prototype of the whole BSA, characterized by the same materials of the final geometry, was designed and built to be irradiated with the same neutron beam. The second Appendix, Appendix B, addresses this part of the work, describing in detail the different configurations tested.

Chapter Four focuses on the design of the treatment room from the viewpoint of radiation protection issues connected to neutron activation of the irradiated materials, ambient dosimetry and patient out-of-field dosimetry. A Monte Carlo model of the treatment room was created and simulations of clinical treatments were carried out to calculate the value of the relevant variables. Due to the emerging evidences of radiation-induced cardiovascular diseases, published in recent literature, special attention was dedicated to the doses absorbed in the heart. All the investigated quantities have been calculated changing the materials of the walls of the room, to evaluate the role played by the construction materials in the relevant factors for radiation protection. The simulations were performed with different Monte Carlo transport codes (MCNP, FLUKA and PHITS) exploiting their specific features depending on the quantity to evaluate.

In the fifth Chapter an original approach for the clinical applications of such a facility is presented. The focus is on the combination of BNCT and hadrontherapy with carbon ions, a possibility that has never been explored before and with high potential. The precision of the carbon ions and the selectivity of the BNCT could in fact allow to treat in the most effective way a variety of tumours, improving the quality of life and the clinical outcome for several patients. The potential synergy between BNCT and heavy ions therapy was studied, from the point of view of dose distribution and Tumour Control Probability (TCP), in a representative clinical case. This part of the work is characterized by innovative aspects, not only regarding the combination of these two particle therapy techniques: the *photon iso-effective dose* model was employed as a formalism to express the dosimetry of the two treatments in photon-equivalent units, instead of the traditional approach based on fixed weighting factors. Moreover, the analysis was performed using a new computational toolkit for dosimetry and treatment planning, specifically developed in Pavia in the framework of the INFN project IT_STARTS.

Chapter Six, finally, draws the conclusions and delineates the future work.

Research in BNCT field has a multidisciplinary nature, requiring expertise from physicists, chemists, engineers, medical physicist, radiobiologists and medical doctors. This research work was conducted in this cross-fertilization spirit, starting from studies in the field of material science and engineering for the pro-

duction and analysis of *Alliflu*, involving computational and experimental nuclear physics for the study of its moderation properties, moving to radiation protection evaluations for the design of an optimized treatment room, and concluding with a medical physics application consisting in the treatment planning of a real clinical case.

A new neutron moderator: Alliflu

Lithiated aluminum fluoride (AlF_3+LiF) has been proven the best material for the core of the BSA to obtain an epithermal beam for BNCT of deep-seated tumours from the neutrons produced by 5 MeV protons on a Be target [16]. Monte Carlo simulations carried out to tailor the clinical beam have demonstrated that, inserted in the BSA structure around the Be target, AlF_3+LiF can lead to an epithermal flux at the beam-port higher than $10^9 \text{ cm}^{-2} \text{ s}^{-1}$ with acceptable thermal and fast neutron contamination and gamma dose. The final BSA chosen for the clinical facility ensures a *therapeutic potential* comparable with the beam used in Finland to treat hundreds of patient. This was proven using an innovative evaluation method based on the calculation of radiobiological figures of merit such as the Uncomplicated Tumour Control Probability simulating the treatment planning of a real clinical case treated in Finland. Moreover, the BSA was optimized taking into account the *safety* of the beam, i.e., the minimization of the out-of-field dose, absorbed in the peripheral organs [15].

The BSA must be compact, with high, stable and uniform density and good mechanical resistance, but aluminum fluoride is commercially available only in the form of powder. Powder is clearly not ideal for our purposes, being not adequate to build a compact BSA with proper density and mechanical characteristics. In Pavia, a solid material was obtained from AlF_3 and LiF powders through what is termed *sintering* [17].

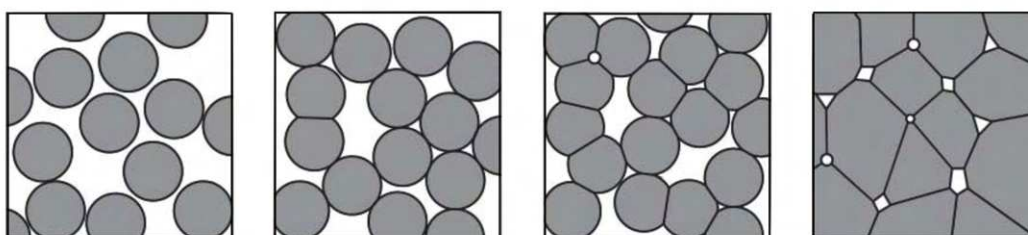


Figure 2.1: Stages of a schematic sintering process

Sintering is a process in which a material with low aggregation becomes a compact solid through the action of high temperatures and pressures. In the process the material does not necessarily melt, as usually the heat and pressure applied are below its liquefaction point. Sintering can be considered as a process of densification of powders with the concurrent reduction of interstitial porosity (Figure 2.1).

The densification can occur via different methods:

- by pressing and subsequent pressure-less heating: *solid-state sintering*
- by means of a limited amount of melting: *liquid-phase sintering*
- by simultaneous application of pressure and heat: *hot-pressing* or *pressure-assisted sintering*

For the compound of our interest, the densification process is complicated by a significant high-temperature volatility. For this reason, a fast, pressure-assisted, sintering process must be applied. A custom Field Assisted Sintering Technique (FAST) apparatus was designed in collaboration between University of Pavia (Department of Chemistry) and INFN Unit of Pavia and prototyped at the local INFN Mechanical Workshop. The technological activity to optimize and build the machine was funded by the National Technology Transfer Commission of INFN, through a R4I (Research For Innovation) project called TT_Sinter. This also became the name of the sintering machine, shown in Figure 2.2.



Figure 2.2: The sintering machine named “TT_Sinter”

Field Assisted Sintering Technique [18] is a process based on a modified hot-pressing. In the latter, external heaters are used, while in FAST the electric current runs directly through the pressing die, generating heat by Joule effect. With this technique, short heating times and rapid cycles are achieved, and thanks to the pulsed current and the so-called “spark plasma effect” a good optimization of the sintered material compared to other techniques can be obtained [19].

The produced densified AlF_3+LiF material has a density ranging from 70 to 99% of the theoretical one and it was proven to be easily workable. It was named *Alliflu* (Figure 2.3).



Figure 2.3: A sample of the new solid material named “Alliflu”

To produce *Alliflu*, an appropriate mix of AlF_3 and LiF powders is placed into a graphite die. The die is then inserted into the vacuum chamber of the TT_Sinter apparatus, between two graphite punches. Figure 2.4 illustrates the set-up inside TT_Sinter chamber. The die is then heated following a user-defined program, with a customized heating rate, by the passage of current between the two punches. When the desired temperature is reached, the die is compressed for a specified interval of time, while keeping constant the temperature. All the steps of the process are selected using the software, as better explained in Appendix A.

The steps for the production of *Alliflu* can be summarized in the following way:

- preparation of the powders
- filling of the graphite die

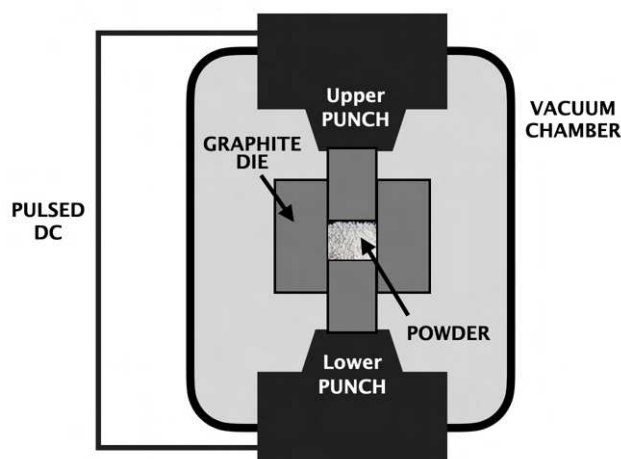


Figure 2.4: Simplified representation of a FAST apparatus

- positioning of the die in the vacuum chamber
- heating up to the desired temperature
- compression with the desired pressure
- cooling and extraction of the sintered sample

Later in this Chapter (Section 2.2) different ways to prepare the powders for sintering will be presented, tested to select the most appropriate procedure to optimize the microstructure of the solid material. Then the following sections will illustrate the characterization of the final *Alliflu*. Before starting the production, preliminary studies have been devoted to select the most suitable powder. The next section presents these measurements.

2.1 Preliminary studies

Preliminary studies were carried out on two kinds of aluminum fluoride powders to select the best one to use for building the BSA core. The two candidates were a chemical-grade powder (origin VWR, supplier Alpha Aesar" with a declared purity higher than 99.99% in metals) and an industrial-grade one (with a declared purity 90%, from the Italian chemical company Fluorsid, Cagliari).

First, the composition of the two powders was assessed by Neutron Activation Analysis (NAA). The detection and quantification of trace elements is in fact critical to predict the activation of the material due to the exposure to the high neutron fluence of the clinical facility.

NAA is a non-destructive analytical technique used to perform multi-element

2.1. Preliminary studies

analyses with minimum detection limits in the sub-ppm¹ range [20]. Its accuracy is around 5%, and often its relative precision is better than 0.1%. In NAA, the sample is irradiated with neutrons which cause the elements to form radioactive isotopes. Since the radioactive emissions and radioactive decay paths for each element are well known, by studying the emission spectra of the radioactive sample is possible to determine the concentrations of the elements within it.

Small amounts of the two powders were weighed with a precision of 0.01 mg and inserted into suitable plastic containers made of polyethylene. The samples were then activated through exposure to neutrons at L.E.N.A. (*Laboratorio di Energia Nucleare Applicata*) of University of Pavia, equipped with the research nuclear reactor TRIGA Mark II operating at a maximum power of 250 kW. The irradiations were carried out in the Central Thimble and in the Rabbit System of the reactor (Figure 2.5), where the total flux at maximum power is $1.39 \times 10^{13} \text{ cm}^{-2} \text{ s}^{-1}$ and $8.37 \times 10^{12} \text{ cm}^{-2} \text{ s}^{-1}$ respectively [21]. The Central Thimble is the channel located at the center of the reactor core, providing space for the placement of specimen capsules at the point of maximum flux, and here the samples were irradiated for 2 hours to detect long-lived isotopes. Instead, the Rabbit System is a pneumatic transfer facility [22] that brings the activated sample from the reactor directly to the radiochemistry laboratory, and was employed for very rapid irradiations (30 sec) to detect short-lived isotopes.

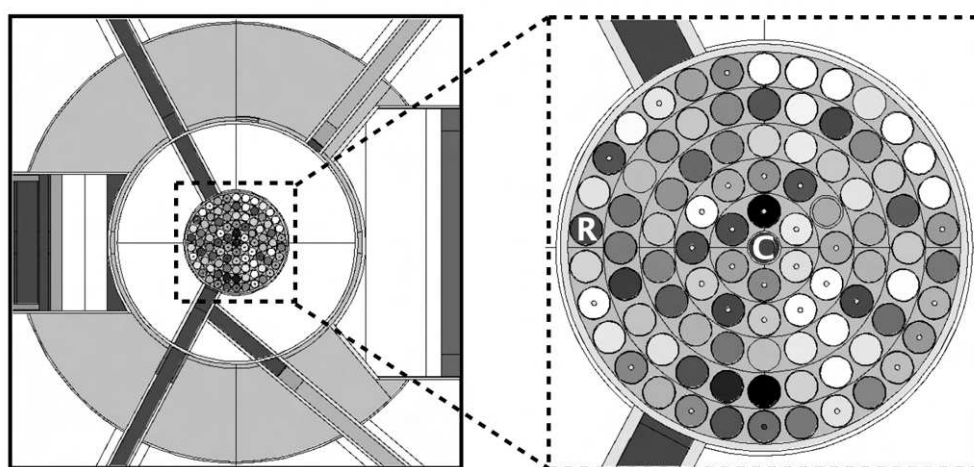


Figure 2.5: Horizontal section of a Monte Carlo model of the TRIGA Mark II reactor. On the right, a magnification of the core with R and C indicating respectively the Rabbit and the Central Thimble irradiation positions

Once the residual radioactivity allowed handling the samples, their emission spectra were acquired with a HPGe (hyper-pure germanium) detector. The analysis of the spectra with the ORTEC software *GammaVision* [23] led to the quantification of the trace elements present in the samples, through the activation

¹The term “ppm” stands for parts per million, a dimensionless unit of measurement indicating a ratio of homogeneous quantities of one to one million. Thus, for the mass, 1 ppm = 1 mg/kg.

reaction rates evaluated from gamma spectroscopy [24]. The mass percentages of these impurities is determined starting from the number of activated nuclei N_{act} . At the end of an irradiation of duration t_{irr} this number is given by:

$$N_{act} = \frac{R}{\lambda}(1 - e^{-\lambda t_{irr}}) = \frac{\phi\sigma N}{\lambda}(1 - e^{-\lambda t_{irr}}) \quad (2.1)$$

where $R = \phi\sigma N$ is the reaction rate (being ϕ the neutron flux, σ the cross section of the reaction involved, both at a fixed neutron energy E , and N the number of interaction centers in the irradiated volume) and λ is the decay constant of the isotope created by activation.

The number of activated nuclei can be estimated from the number of counts ΔC which the software *GammaVision* returns as the integral of a peak. The software in fact allows the calibration in intrinsic and geometric efficiency, compares the energies of the experimental peaks with a library of emissions, and returns for each peak the number of counts, i.e. the peak area. The number of decays in the interval of time between the start (t_1) and the stop (t_2) of the spectrum acquisition is:

$$N_{act} = \frac{\Delta C}{(e^{-\lambda t_1} - e^{-\lambda t_2})} \cdot \frac{1}{\varepsilon} \cdot \frac{1}{B} \quad (2.2)$$

where ε is the efficiency of photon detection at the energy of the considered peak, and B indicates the branching fraction² of the studied emission. The reaction rate is thus given by:

$$R = \frac{\lambda}{(1 - e^{-\lambda t_{irr}})} \cdot \frac{\Delta C}{(e^{-\lambda t_1} - e^{-\lambda t_2})} \cdot \frac{1}{\varepsilon} \cdot \frac{1}{B} \quad (2.3)$$

Therefore, N can be calculated through the equation

$$R = N \int_{E_{min}}^{E_{max}} \phi(E)\sigma(E)dE \quad (2.4)$$

to take into account the dependence of cross sections on energy. As the integral is not easily computed, the quantification is usually obtained by comparison with the activation of standards, i.e. samples with known number of activation centers: considering the same reaction (thus the same cross section) and irradiating the standard in the same neutron field, it is possible to equal $\phi\sigma$ from $R = N\phi\sigma$, obtaining:

$$N_{sample} = N_{STD} \frac{R_{sample}}{R_{STD}} \quad (2.5)$$

where N_{STD} and R_{STD} are the number of interaction centers and the reaction rate of the standard, and N_{sample} and R_{sample} the same quantities for the sample investigated.

²In branching decays, i.e. nuclear decays which can proceed in two or more different ways, branching fraction or branching ratio is the fraction of nuclei which decay by a certain mode [25]

Without standards, the quantification of elements can be obtained from the reaction rate approximated thanks to the Høgdahl convention [26]:

$$R = N(\phi_0\sigma_0 + \phi_e I_0(\alpha)) \quad (2.6)$$

being σ_0 is the thermal cross section, ϕ_0 and ϕ_e the conventional thermal and epithermal neutron fluxes respectively, and $I_0(\alpha)$ the resonance integral corrected by the parameter α , which accounts for the deviation of epithermal flux from ideal trend $1/E$:

$$I_0(\alpha) = \sigma_0 \left((Q_0 - 0.429) E_r^{-\alpha} + \frac{0.429}{0.55^\alpha (2\alpha + 1)} \right) \quad (2.7)$$

where E_r is the resonance energy and $Q_0 = I_0/\sigma_0$ the resonance integral to thermal cross section ratio. I used values for α , ϕ_0 and ϕ_e coming from [27], for Q_0 and E_r from [28] and for cross sections from [29]. Eq. 2.6 has been applied to determine the interaction centers N of impurities in AlF_3 , using the reaction rates obtained from spectrometry. To improve the precision, the peak associated to the highest branching fraction was chosen for each decay.

Considering that the maximum energy of neutrons from the INFN RFQ accelerator is about 3.2 MeV, only the isotopes with an activation threshold less than this value were considered. The neutron spectrum in the reactor is in fact different from that of the RFQ coupled to the beryllium target (see Figure 2.6). For this reason the *Alliflu* activation in the facility was not directly inferred from the measurements in the reactor, but rather evaluated by implementing the NAA-determined composition in Monte Carlo simulations, as better explained in section 2.1.1.

Table 2.1 summarizes the results of the NAA study on the two AlF_3 powders, showing the detected isotopes with their calculated mass percentages in industrial and chemical-grade powder and the half-lives of their activation products.

The results of the NAA showed that industrial-grade powder has a higher concentration of trace elements, but these impurities generate activation products with shorter half-lives than in chemical-grade powder [30]. Moreover, the impurities in industrial-grade powder seem to facilitate the sintering process. In fact, by using this powder it is easier to obtain a material with higher relative densities, closer to the maximum nominal density of about 3 g/cm^3 . For these reasons, industrial-grade powder has been chosen for the sintering process to create the main constituent of the BSA core.

2.1.1 Neutron activation of the BSA core

The BSA with AlF_3 containing the trace elements measured in the powder was simulated with the Monte Carlo code MCNP6 [31]. The neutron source was implemented with uniform distribution in the Be target as described in [16], taking into account the experimental double differential spectrum emerging from the

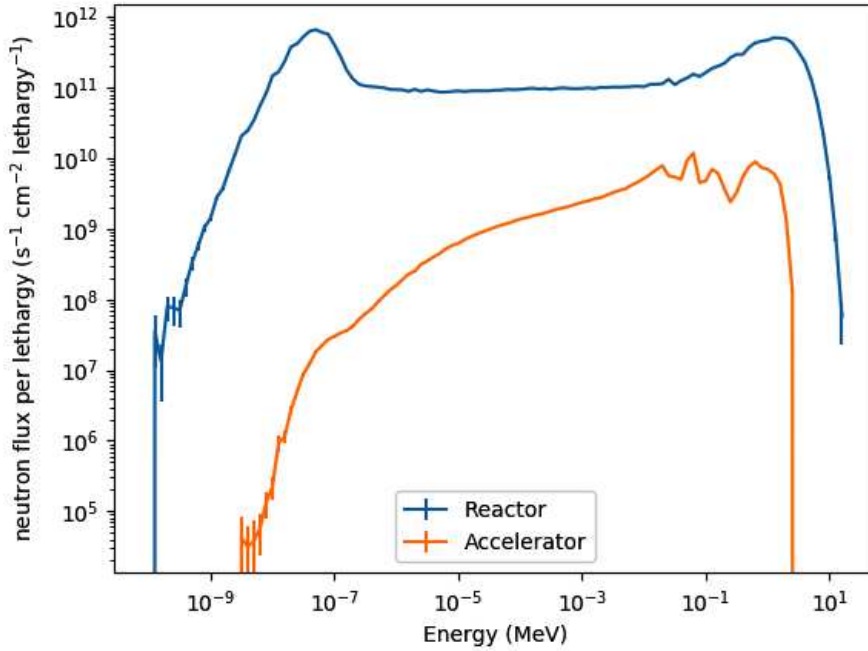


Figure 2.6: Comparison between neutron spectra in the LENA reactor and in the INFN RFQ accelerator

(p,n) reaction in Be for 5 MeV protons [32]. A simulation with coupled neutron-photon transport was run to estimate the residual activity of BSA after a clinical irradiation.

The reaction rates generating the radionuclides of interest were calculated. Reaction rates are obtained in MCNP6 scoring the neutron flux (F4-type *tally*), combined with an instruction indicating the nuclear reaction of interest and the isotope involved. Finally, the activity A at the end of the irradiation can be evaluated from the simulated reaction rate R using:

$$A = R(1 - e^{-\lambda t_{irr}}) \quad (2.8)$$

where λ is the decay constant of the radioisotope created by activation and t_{irr} the patient irradiation time, taken equal to 2 hours. The calculation is conservative, since the typical duration of a BNCT treatment is about 1 hour.

The simulated reaction rates in the BSA core are listed in Table 2.2, with the specific activities after a 2-hours irradiation (calculated through Eq. 2.8, dividing by the mass). To ensure a good convergence of the simulations, they run for a time sufficient to obtain a statistical relative error lower than 0.1%. The errors associated to the results come from the uncertainty of impurities percentages, when evaluated by NAA with the Høgdahl convention. In the case of sodium, for which a standard was used, the error depends on the precision with which the cross section is known.

Table 2.1: Results of the NAA study on the samples of AlF_3 powders.

Isotope	Industrial-grade [mass %]	Chemical-grade [mass %]	Product half-life
As-75	1.1×10^{-4}	1.2×10^{-7}	1.0778 d
Br-81	4.3×10^{-7}	6.5×10^{-7}	35.30 h
Cl-37	-	1.7×10^{-5}	37.24 min
Co-59	9.5×10^{-6}	1.18×10^{-5}	5.2714 y
Cr-50	-	9.8×10^{-8}	27.7025 d
Fe-58	4.3×10^{-7}	-	44.503 d
Ga-71	5.8×10^{-6}	-	14.10 h
La-139	-	3.0×10^{-7}	1.6781 d
Sb-121	1.1×10^{-7}	1.2×10^{-5}	2.7238 d
Sb-123	1.8×10^{-7}	2.7×10^{-5}	60.20 d
Sc-45	2.1×10^{-8}	3.2×10^{-7}	83.79 d
Se-74	-	2.9×10^{-8}	119.779 d
Zn-64	1.6×10^{-5}	-	244.26 d

As expected, the major contribution to the induced radioactivity is due to the activation of aluminum. However, as the radioisotope Al-28 decays rapidly with a half-life of about 2 minutes, it does not represent the major concern for the facility management. Activation products with half-lives longer than 10 days, such as Co-60, Fe-59, Sb-124, Sc-46 and Zn-65, give specific activities smaller than 1 Bq per gram at the end of irradiation.

Other preliminary studies were carried out on the material regarding its density, water absorption and solubility, as described below.

2.1.2 Density

The buoyancy technique was used to precisely determine the density of solid *Al-flu*, when difficult to establish with other methods. In fact, the determination of the density is not correctly derivable through the geometric calculation for small and highly irregular samples. Moreover, the geometric calculation would not take into account the porosity of the material. Instead, this can be relevant for the study of the density compared to the nominal value.

The buoyancy technique [33] is a gravimetric method for the determination of the density based on the Archimedes principle: it uses the fact that the weight of a body immersed in a fluid undergoes a decrease equal to the weight of the volume of fluid displaced. Thus, in this technique, the sample is weighed both in air and completely immersed in an auxiliary fluid of well-known density.

Indicating with m_A the weight of the sample in air, with m_F the weight of the sample in the fluid, and with ρ_A and ρ_F the densities of air and fluid respectively,

Table 2.2: Simulated reaction rates and specific activities of the BSA core constituents after 2h of irradiation

Isotope	Half-life	R [s ⁻¹ g ⁻¹]	a [Bq/g]
Al-28	2.414 min	(2.9±0.3) × 10 ⁶	(2.9±0.3) × 10 ⁶
As-76	1.0778 d	(2.9±0.6) × 10 ⁵	(7.7±1.5) × 10 ³
Br-82	35.30 h	(7.9±1.6) × 10 ²	15±3
Co-60	5.2714 y	(3.2±0.6) × 10 ⁴	(4.8±1.0) × 10 ⁻¹
Fe-59	44.503 d	37±7	(2.4±0.5) × 10 ⁻²
Ga-72	14.10 h	(8.4±1.7) × 10 ⁴	(4.0±0.8) × 10 ²
Mg-27	9.458 min	(6.7±1.3) × 10 ⁴	(6.6±1.3) × 10 ⁴
Na-24	14.9590 h	(2.1±0.2) × 10 ⁴	(9.5±1.9) × 10 ²
Sb-122	2.7238 d	(3.0±0.6) × 10 ²	3.2±0.6
Sb-124	60.20 d	(4.9±1.0) × 10 ²	(2.4±0.5) × 10 ⁻¹
Sc-46	83.79 d	8.7±1.7	(3.0±0.6) × 10 ⁻³
Zn-65	244.26 d	(1.9±0.4) × 10 ³	(2.3±0.4) × 10 ⁻¹

the density ρ of the sample can be calculated as follows:

$$\rho = \frac{W_A}{W_A - W_F}(\rho_F - \rho_A) + \rho_A \quad (2.9)$$

The precision of the density measurement in this case strongly depends on the precision of the weight measurement. Therefore, an analytical balance with high precision is needed. For the measurements of this study I used the laboratory balance available at the Chemistry Department of University of Pavia, model METTLER AE 163 [34], equipped with a special support for the positioning of the sample both for the measurement in air and in a fluid. Figure 2.7 shows the experimental set-up. Each sample was measured independently four times in each position, and the density was calculated through the mean of the resulting values.

For the mass measurements with the sample immersed in a fluid, pure ethanol (density 0.8 g/cm³ at 15°C) was used. In cases where the fluid is able to penetrate into the material due to the open pores, an escape of air bubbles from the sample can be noted together with a variation in the measured weight. In the described measurements this did not occur, indicating that there were no exposed cavities of sufficient size for the fluid to penetrate with its surface tension. In any case, a reasonable time was waited for each measurement in ethanol, to verify the stability of the mass value.

The density measurements conducted showed a remarkable variability of density among samples prepared with the same powder and sintering process. This required an optimization of the sintering machine and sintering program, as illustrated in Appendix A.



Figure 2.7: Analytical balance in the experimental set-up used for the density measurements with the buoyancy technique

2.1.3 Water absorption and solubility

The water absorption and solubility of the new *Alliflu* material were investigated as well. These aspects could in principle be relevant for the use of *Alliflu* for a long time in the facility, since the combination of high water absorption and high solubility could result in an undesired loss of material from the BSA. In addition to the extraction of water-soluble components, absorbed moisture could also lead to dimensional/mass alterations or to changes in the mechanical properties of the material.

The water or moisture absorption is the capacity of a material to absorb moisture from its environment [35]. Water absorption can be expressed as the increase in weight percent of a specimen under different testing procedures. The moisture content can be evaluated through:

$$M_c = \frac{W_c - W_0}{W_0} \times 100\% \quad (2.10)$$

where W_0 represents the dry weight of the specimen and W_c its weight under the particular testing condition.

Since the BSA is not expected to come in contact with water, we evaluated the moisture absorption at equilibrium: in this case the sample is exposed to a humid environment at a specified temperature for 24 hours.

A set of 15 *Alliflu* samples with variable density was kept for 24 hours at room temperature and subsequently weighed with high precision. I used the aforementioned METTLER balance, measuring four times independently the mass of each sample and calculating the average value. Then, the samples were placed to dry in a thermostatic oven (Fratelli Galli® G-THERM [36]) at 100°C for 22 hours. Once removed from the oven, the samples were weighed again, also in this case four times independently.

The mean moisture absorption resulting from the described procedure by applying Eq. 2.10 is very low, less than 0.05%. To make a comparison, according to the standard of ASTM International (formerly *American Society for Testing and Materials*) [37] a material defined as *impervious* has a water absorption lower than 0.5%.

To carry out the solubility test, the oven-dried specimens were subsequently immersed in UPW, ultrapure water [38]. UPW is a water purified at the highest levels for all contaminant types: a microbiologically pure water containing no substance capable to interfere with a laboratory procedure influencing the results.

The 15 *Alliflu* specimens were kept at room temperature totally immersed in 30 mL of UPW, each one separately, for 7 days. After this time, they were dried again in the G-THERM thermostatic oven, at 100°C for 22 hour, and then weighed once more. The difference between the dry weight before and after the immersion in UPW is due to the loss of material that dissolved in water and it is thus a measure of the solubility. Solubility is indeed the maximum amount of a substance that will dissolve in a given amount of solvent at a specified temperature [39].

Averaging the dry-weight differences over the set of samples and dividing by the 30 mL volume of UPW used, a solubility value of 0.4 mg/mL was obtained. This indicates a slightly soluble material, as can be seen referring to the different degrees of solubility listed in Table 2.3.

The obtained values of moisture absorption and water solubility suggest that the use of *Alliflu* for the BSA core under standard operating conditions of temperature and humidity does not raise any concern.

Table 2.3: Definition of different levels of solubility, from [40]

Descriptive degree of solubility	Solvent parts needed for 1 part of solute	Solubility [mg/mL]
very soluble	<1	>1000
freely soluble	1-10	100-1000
soluble	10-30	33-100
sparingly soluble	30-100	10-33
slightly soluble	100-1000	1-10
very slightly soluble	1000-10000	0.1-1
insoluble	>10000	<0.1

2.2 Morphology

Ideally, the final solid material should be perfectly homogeneous and uniform. To investigate the microstructure of *Alliflu*, several samples with variable density have been produced to be analyzed through SEM microscopy [41].

SEM stands for Scanning Electron Microscope, a type of microscope that produces images by scanning the surface of a sample with a focused beam of electrons. The image is produced by the position of the electron beam, scanned in a raster scan pattern, combined with the intensity of the detected signal. The interaction of the electrons with the atoms in the specimen generates different signals, containing information not only about the topography of the surface but also about the composition of the sample:

- Visible light: luminescence;
- Backscattered electrons: high energy electrons of the incident beam almost entirely inelastically scattered through the material;
- Secondary electrons: low energy (<50 eV) valence electrons ejected via inelastic scattering;
- Characteristic X-rays: X-rays generated via inelastic collisions.

The signal that contributes to the SEM imaging of the microstructure comes from backscattered and secondary electrons.

A good preparation of the specimen is pivotal to achieve a satisfactory SEM imaging [42]. To obtain the best results for microstructure analysis, samples are often cut and embedded in epoxy resin with a face exposing the material section ground and polished. The grinding is performed with fixed abrasives, usually abrasive particles bonded in sandpapers, for an initial leveling and cleaning of the surface at the cutting point. The process is based on the use of increasingly abrasive particles to progressively remove material from the surface until the desired result is obtained. The subsequent polishing removes the artifacts of the grinding by the action of abrasive particles contained in a liquid, suspended on a cloth. A minimum amount of material is lost during the operation, the overall integrity of the sample is ensured thanks also to the protection provided by the resin embedding. When correct grinding and polishing is carried out, the microscopy allows the visualization of the true microstructure of the examined material.

To this end, *Alliflu* samples were first subjected to cross-sectional cutting, in order to expose an area representative of the entire thickness of the material, and then inserted into special plastic molds with the section in contact with the bottom (Figure 2.8). In the meantime, an appropriate epoxy compound has been obtained by combining epoxy and hardener at the right mix ratio (~8:1 in mass) stirring thoroughly for one full minute while paying attention to avoid the formation air bubbles. The mold containing the sample was then filled with this mixture, taking care to cover the entire *Alliflu* section. The mold was finally left for at least 24

hours at room temperature to let dry the epoxy compound. The resin puck so obtained was then ground and polished to achieve a perfectly smooth and reflective surface on the face showing the *Alliflu* section.

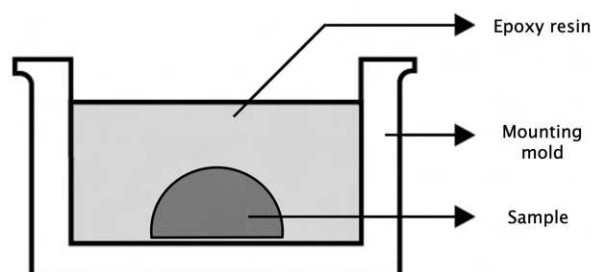


Figure 2.8: Scheme of the components of a resin mounted specimen

A grinding/polishing machine (BUEHLER® model PHOENIX ALPHA, equipped with Vector™ Power Head [43] and automatic water flushing) was used for the mechanical preparation of the specimen surface. For the grinding steps, sandpapers with progressively raised grit were used. The grit or grade of sandpaper is a number referring to the size of its abrasive particles: the higher this number, the deeper is the sanding achieved.

We started with P600 grit sandpaper (measured according to the FEPA standard, of the *Federation of European Producers of Abrasives*). It was used to equalize the faces and remove the surface layer of resin in contact with the sample. Then, once obtained the exposure of a reasonable amount of *Alliflu* section from the resin, we used sandpapers with grades: P800, P1000, P1200, P2500 and P4000, for at least 0.5, 1, 1.5, 2 and 4 minutes, respectively. The minimum time required derives from experience with this type of mechanical preparation, in any case continuous visual checks served to verify the progress of the surface finishing.

In the last phase of surface finishing, once deactivated the water flushing and replaced the sandpaper with a cloth, colloidal silica and liquid diamond suspension were used for 4 minutes each. Both were added directly on the rotating cloth, previously moistened with the solution, at intervals of about 1 minute. In this way, through the combination of chemical action with fine abrasive effect, scratch-free and deformation-free samples are achievable.

After the surface was as desired, the preparation for SEM examination of the resin puck continued with the application of a support for the imaging with a small layer of conductive tape connecting this to the *Alliflu* section, and a carbon coating. The specimen needs in fact to be conductive to enable the SEM imaging. This can be achieved via the sputtering on the sample of metals such as Cr, Au or Pt, which also improve the signal-to-noise ratio by increasing the amount of secondary electrons detectable from the surface of the specimen. We used instead carbon because it can be easily deposited in a finer layer and avoids the contamination of SEM imaging due to the grains of metallic coatings. Fine carbon layers are transparent to the electron beam but conductive, allowing to carry



Figure 2.9: Example of preparation of an Alliflu sample for SEM examination. (From left to right: cutting of the sample, sample embedded in resin and sample after the polishing)

out the X-ray spectroscopy that will be introduced later. The last step of the sample preparation was thus the uniform coating of the specimen with a thin layer of C (a few Å) by using the CRESSINGTON Carbon Coater model 208carbon [44] present at the Arvedi Laboratory of CISRiC³, University of Pavia. The machine exploits the thermal evaporation of carbon: a carbon source is heated in vacuum between two high-current electrical terminals, and once reached its evaporation temperature a fine layer of C is deposited on the specimens.

To summarize, the samples were prepared for SEM microscopy by the following procedure:

1. cross-sectional cutting
2. embedding into epoxy resin
3. grinding with progressively finer sandpapers
4. polishing with colloidal silica and liquid diamond
5. application of the support
6. carbon coating

The SEM analysis was carried out with the high resolution SEM of the TESCAN Mira3 XMU series [45] present at the CISRiC Arvedi Laboratory. Figure 2.10 shows the results of SEM analysis on three different *Alliflu* samples with increasing density.

³Centro Interdipartimentale di Studi e Ricerche per la Conservazione del patrimonio culturale

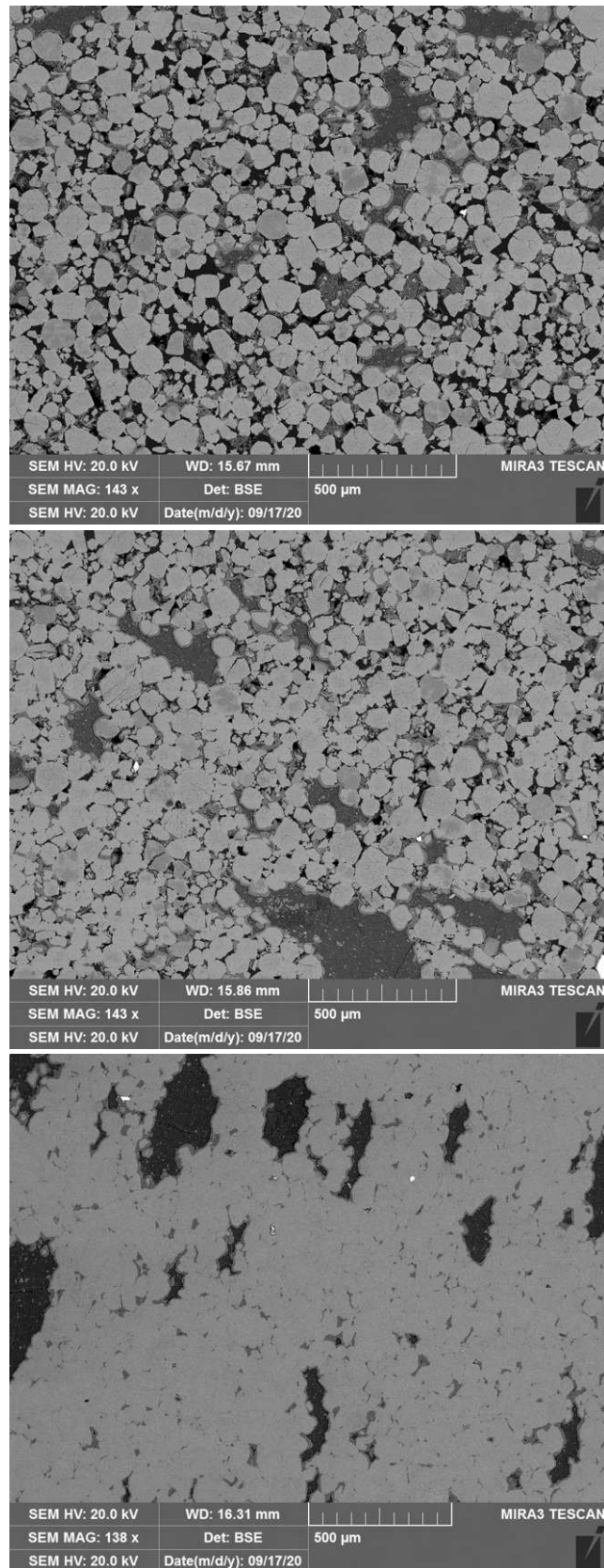


Figure 2.10: SEM imaging of 3 different Alliflu samples (with increasing density from top to bottom) created with the original production procedure

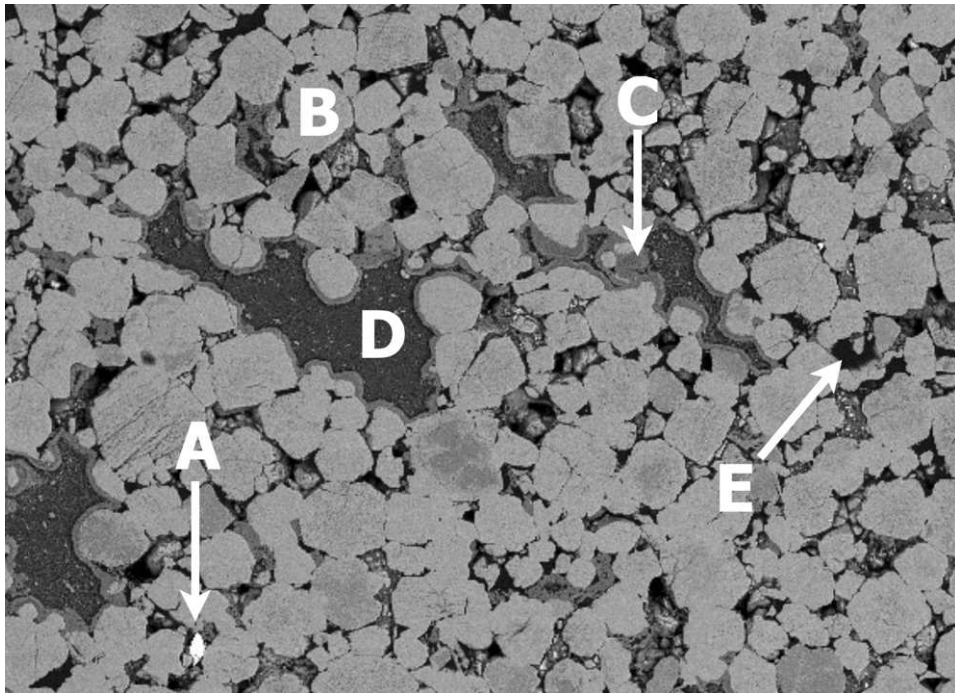


Figure 2.11: Different components in Alliflu microstructure (magnification of the second SEM image of Figure 2.10)

At least 5 different components can be distinguished in the microstructure of the material, based on the color with which they appear in the SEM image. An Energy Dispersive X-ray (EDS or EDX) Spectroscopy microanalysis [46] helped to correctly discriminate the components identifying their composition. The SEM available at CISRiC Arvedi Lab of University of Pavia is in fact a SEM/EDS system, equipped with an Energy Dispersive X-ray Spectroscopy facility.

Energy Dispersive X-ray Spectroscopy is an elemental microanalysis technique allowing the identification and quantification of all the elements of the periodic table except for H, He, and Li. The principle of this technique is based on the emission of X-rays from a sample due to its interaction with the electron beam: if any material with atomic number higher or equal than four is examined with electron microscope, X-rays are generated from just below the surface. The X-ray spectrum is characteristic and known for each element, thus the elemental composition of the sample can be inferred from the detected X-rays. X-ray microanalysis systems are of two types: energy-dispersive X-ray spectroscopy (EDS) and wavelength-dispersive spectroscopy (WDS). EDS measures the energies of X-rays and provides the concurrent analysis of all the detectable elements together. By contrast, WDS measures the wavelengths of X-rays with individual crystals, each focusing on one element at a time. WDS has a better resolution than EDS but it is more complex to use. The limit of detection of EDS is typically for a mass fraction about 0.001–0.003, depending on the element, the matrix containing it, and the operating conditions of the instrument.

Applying the EDS method, the composition of the areas appearing with different colors in the SEM imaging of *Alliflu* was analyzed. Naming them alphabetically from the lightest to the darkest (the magnification shown in Figure 2.11 can be used as a reference):

- A: (white) steel, probably processing residual
- B: (light grey) grains of AlF_3
- C: (grey) LiF that reacted with AlF_3
- D: (dark grey) agglomerates of LiF
- E: (black) porosity

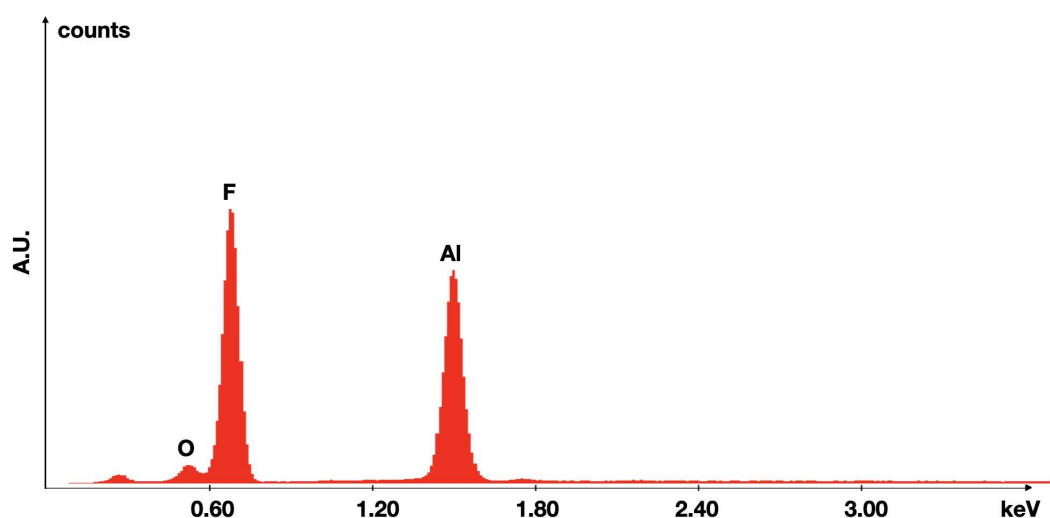


Figure 2.12: Energy Dispersive X-ray spectrum (EDS) of the “B” phase (Figure 2.11) of *Alliflu* microstructure

Figures 2.12, 2.13 and 2.14 show representative EDS spectra collected by scanning in the areas B, C and D, respectively. The second spectrum (C) clearly shows a higher presence of fluorine compared to the first one (B), while in the third spectrum (D) there is practically no aluminum.

As expected, SEM analysis confirmed that higher density corresponds to a tighter bound of the powder grains, but showed a not satisfactory uniformity of the material even in the densest samples. In fact, the darker spots corresponding to lithium fluoride indicated that Li was not evenly distributed in the volume of the densified material. In view of the construction of the BSA from *Alliflu* bricks, the uniformity detected did not appear adequate: lithium lowers the thermal component of the beam by neutron capture on ${}^6\text{Li}$, and it is clearly preferable to have

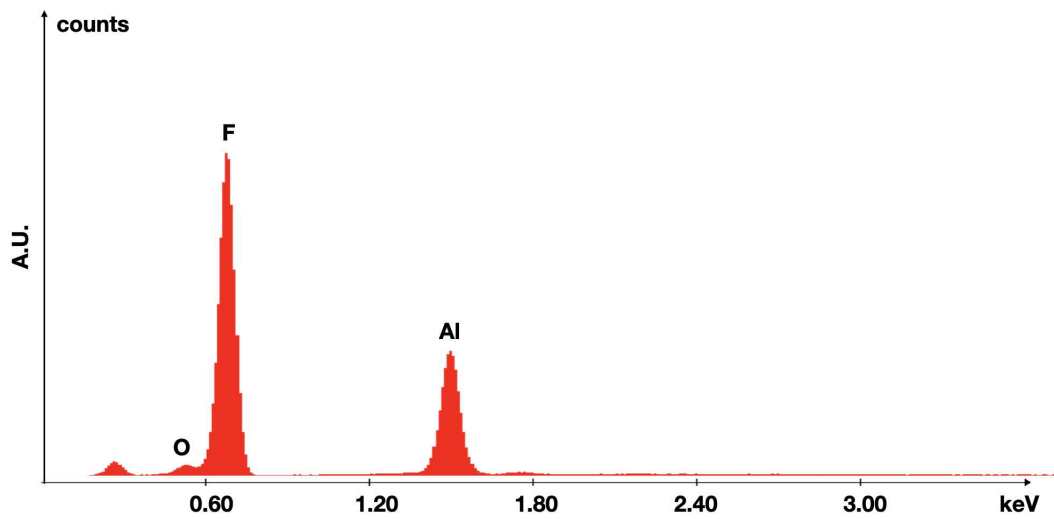


Figure 2.13: Energy Dispersive X-ray spectrum (EDS) of the “C” phase (Figure 2.11) of Alliflu microstructure

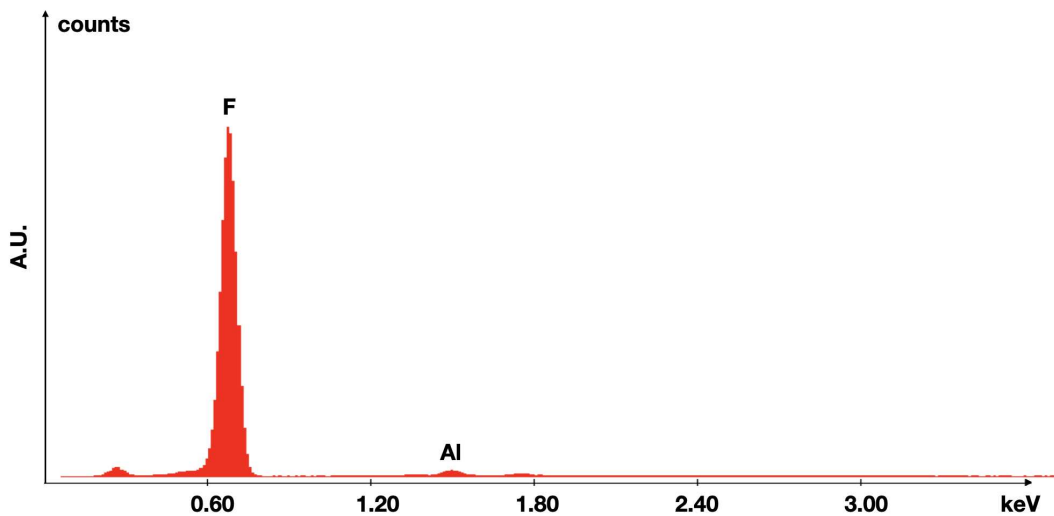


Figure 2.14: Energy Dispersive X-ray spectrum (EDS) of the “D” phase (Figure 2.11) of Alliflu microstructure

the capture centers uniformly distributed throughout the BSA. Furthermore, such non-homogeneity could cause differences in the mechanical characteristics between one brick and another and should therefore be avoided.

The conclusions of this first set of measurements required an optimization of the production process to obtain a satisfactory configuration of *Alliflu* microstruc-

ture. We tested three different new procedures:

1. with a new method to mix the powders of AlF_3 and LiF ;
2. as 1, but with the re-cooking of the sintered material;
3. as 1, but using a LiF powder previously micro-ground.

In the following, the three tested procedures are described in more detail.

In the first case, the initial production process was modified for what concerns the mixing of the powders of aluminum fluoride and lithium fluoride. To improve the homogeneity of the mixture of $\text{AlF}_3 + \text{LiF}$, a mixing machine named TURBULA[®] was used (Figure 2.15).



Figure 2.15: The 3D shaker mixer named TURBULA[®] used to optimize the mixing of AlF_3 and LiF powders

TURBULA[®] is a three-dimensional, highly effective, shaker mixer [47]. It is composed by a basket where any form of container with volume up to 2 liters can be fastened via twisted interlaced rubber rings. The functioning of TURBULA[®] is based on the combination of rotation, translation and inversion throughout the mixing process. Thanks to the ever-changing motion of the container, an excellent homogeneity of the mixture is achievable even with short mixing times.

To further favor the homogeneity of the mixture, only small quantities of powders were added in the TURBULA[®] at a time. We started with about 5 grams of $\text{AlF}_3 + \text{LiF}$, placed in a 50 ml plastic container together with 3 tungsten carbide balls

2.2. Morphology

to help the mixing. Each container was mixed in TURBULA[®] for at least 1 hour and a half.

Then, in order to optimize the production efficiency, a special holder was engineered to accommodate multiple vials together, allowing the mixing of a higher amount of powder but subdivided in small quantities. The holder was designed at the Mechanical Workshop of INFN Pavia and manufactured with the 3D printer locally available.

The imaging SEM of an *Alliflu* sample created with this procedure is shown in Figure 2.16. The uniformity in the lithium distribution was better in these samples compared to the first ones, but the microstructure could still be improved.

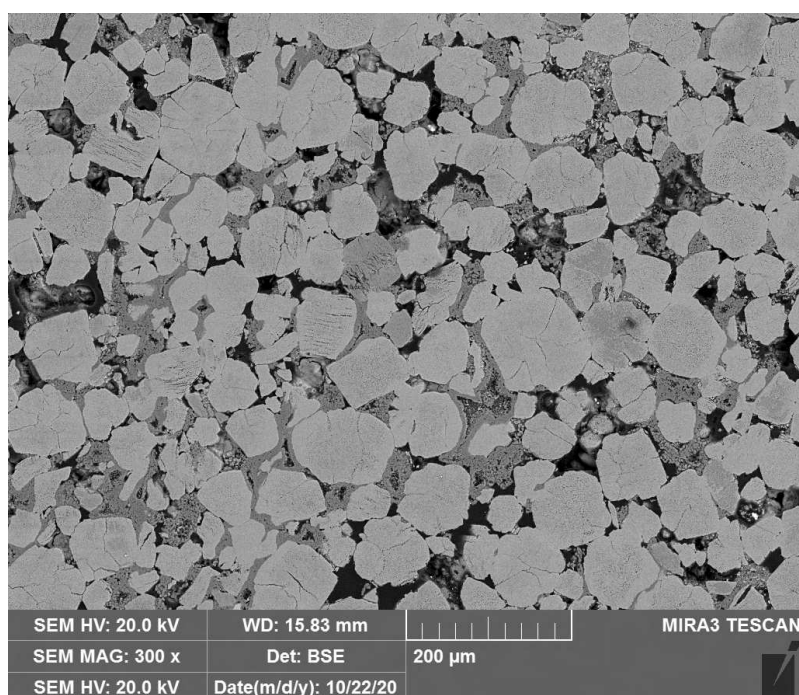


Figure 2.16: SEM imaging of an *Alliflu* sample created following the first of the new tested procedures to optimize the microstructure

We thus tested the second new procedure, in which the mixing with TURBULA[®] was accompanied by a re-heating of the sintered material. Sintered *Alliflu* samples produced with the powders mixed via TURBULA[®] were placed in a thermostatic oven. The samples were heated at 800°C for 2 hours. The SEM imaging on one of such samples is shown in Figure 2.17. It appears that a sort of crystallization occurred in the material, with an unsatisfactory result as regards the final microstructure.

In the third procedure, an attempt was made to reduce the size of the LiF grains to mix with TURBULA[®], by means of a prior micro-grinding of the lithium fluoride powder.

We used the FRITSCHE Planetary Micro Mill model PULVERISSETTE 7 (Figure 2.18). Such machine has 2 grinding stations, each of which houses a grinding

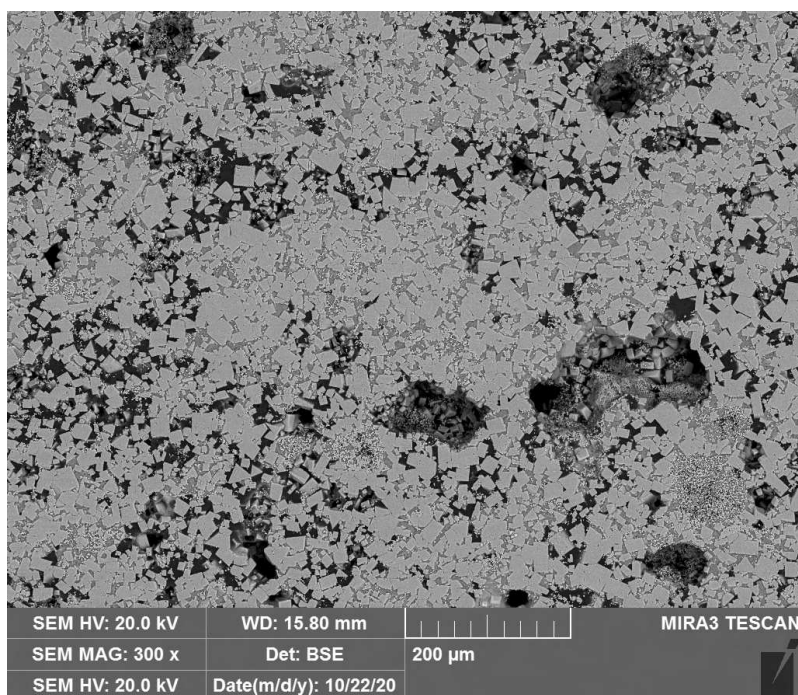


Figure 2.17: SEM imaging of an Alliflu sample created following the second of the new tested procedures to optimize the microstructure

bowl with tungsten carbide interior. The powder is inserted into the bowl together with a certain number of grinding balls. The machine works by making the grinding bowl rotate around its own axis on a main disk which, in turn, rotates in the opposite direction. The combination between the high-energy impact of grinding balls and the friction between the balls and the bowl wall produces the comminution of the powder [48].

Due to the capacity of the bowls, we ground only up to 3.5 grams of LiF at a time, with the add of an amount of grinding balls corresponding to about 10 times the mass of the powder. Based on previous experience with similar powders, the mill was set to work 25 minutes at 300 rpm for 2 cycles separated by a 3-minute pause. The obtained micro-ground powder was then used to sinter *Alliflu* samples, after mixing with AlF_3 in TURBULA[®].

The microstructure of the material so produced (SEM imaging in 2.19) appears more uniform compared to the other procedures: in this case the AlF_3 grains are almost completely surrounded by a layer where LiF and AlF_3 reacted. At the same time, the porosity has decreased with respect to the one shown in Figure 2.16.

The third procedure, producing a quite uniform sample with lithium fluoride well distributed in the volume, was thus selected as the most adequate protocol for the preparation of the material.

Based on this result, we tried also a fourth procedure consisting in the micro-grinding of both LiF and AlF_3 . The obtained homogeneity was better (Figure 2.20), however the process required much longer preparation times due to the capacity



Figure 2.18: The FRITSCH Planetary Micro Mill model PULVERISETTE 7 used for the grinding of the LiF powder

of the mixing bowls. This procedure was thus discarded based on the cost/benefit balance, in view of a massive production of *Alliflu* for the construction of the clinical BSA.

Moreover, we ensured that the simulation of a uniform AlF_3+LiF material reliably represented the effect of the microstructure obtained in the third procedure. This test was made by simulating the interaction of neutrons with uniform AlF_3+LiF and with a lattice of AlF_3 grains surrounded by Li_3AlF_6 . The dimensions of the lattice elements were set to reproduce as faithfully as possible the microstructure of the third procedure detected via SEM and the mass ratio of the elements (Figure 2.21). The comparison of the tallies in the two situations showed a very good agreement over almost the entire energy range, confirming that a uniform material and the material obtained with the third procedure behave in the same way regarding neutron interaction, and that the simulation of a uniform material is a good model of the final structure.

2.3 Mechanical resistance

An important evaluation for BSA concerns the mechanical resistance of its *Alliflu* core. Any loss of material is highly undesirable, and not only because of the possible residual radioactivity of the material due to neutron activation, but also because in this way the moderation of neutrons could be modified. A change in the geometry of the BSA could affect the spectral characteristics of neutrons, possibly decreasing the quality of the clinical beam. A good mechanical resistance of the main BSA material is thus an important aspect to ensure, both for staff and patient safety.

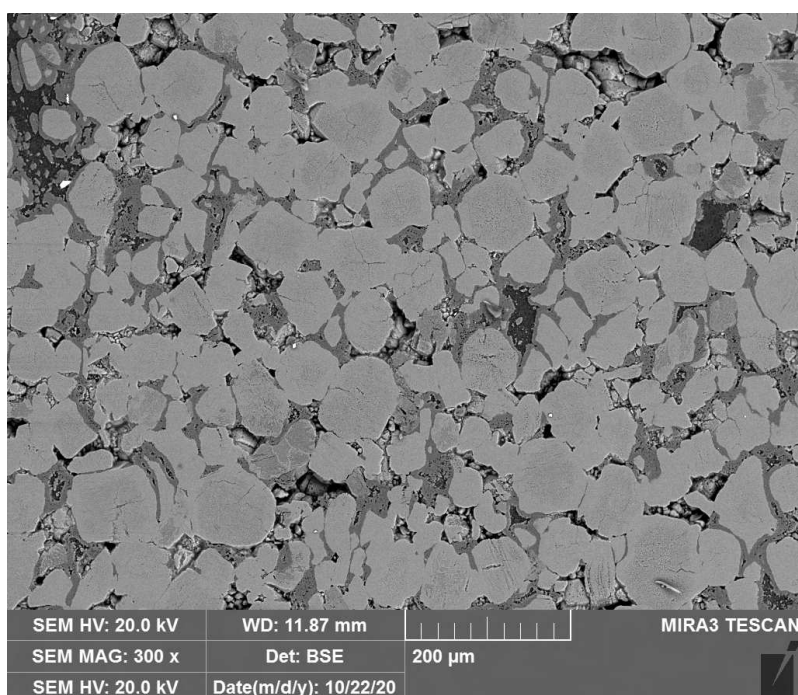


Figure 2.19: SEM imaging of an Alliflu sample created following the third of the new tested procedures to optimize the microstructure

Moreover, the BSA is expected to receive a high dose of radiation during the lifetime of the clinical BNCT facility, in particular the neutron flux at the beryllium target is higher than $10^9 \text{ n cm}^{-2} \text{ s}^{-1}$. As neutrons interact with *Alliflu*, some are captured by Li-6 emitting charged particles, and these can possibly generate changes in the microstructure, for example causing cracks. For this reason it is important to study the mechanical properties of the new material before and after the exposure to neutrons.

Summarizing, two are the aims of the study on the mechanical resistance of *Alliflu*. The first, is to verify that the new material *Alliflu* is able to support its own weight without any break or crack occurring. The second, is to understand how a high neutron fluence can possibly affect this property.

To investigate these aspects, *Alliflu* samples were prepared to be studied by means of compression tests. The study was based on the compression of irradiated and non-irradiated *Alliflu* samples with variable density. Those non-irradiated are also used as control sample for the irradiated ones. Also in this case, the nuclear reactor TRIGA Mark II of L.E.N.A. in Pavia was used as the neutron source. In a few hours of irradiation at the reactor, it is possible to integrate a neutron fluence corresponding to months of use of the clinical facility.

The mechanical resistance study was conducted in two rounds of measurements. The first round involved the irradiation of 3 *Alliflu* samples only. At that moment, in fact, the new improved machine for sintering was not ready and the prototype available was not optimized for an efficient production of the samples.

2.3. Mechanical resistance

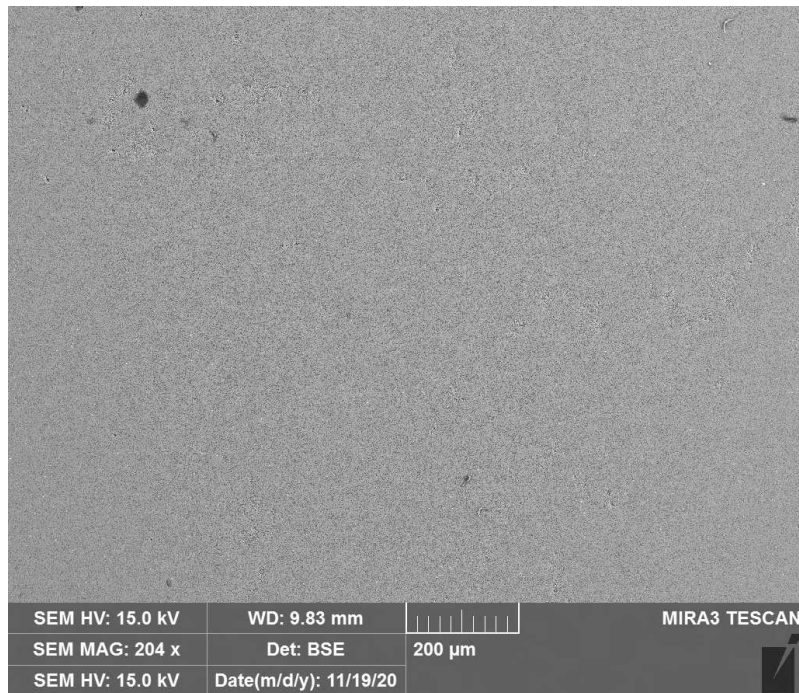


Figure 2.20: SEM imaging of an *Alliflu* sample produced with both the LiF and AlF_3 powder micro-milled

Moreover, after the irradiation of the samples in the reactor, it is necessary to wait enough time for their decay to be able to handle them safely. The first round of measurements was thus considered as a preliminary test to determine the best experimental conditions for a more complete analysis involving a greater number of samples.

The *Alliflu* samples were exposed to neutrons in the Central Thimble of the TRIGA Mark II reactor, with an irradiation of a total duration of 6 hours. The spectrum of neutrons in that position is shown in Figure 2.6. In terms of neutron fluence, this is comparable to about 1000 clinical treatments in the RFQ-based BNCT facility. Thus, the effects of such irradiation can be reasonably assumed as representative of a long working time of *Alliflu* as core of the BSA for the clinical beam.

An acceptable decay time for irradiated *Alliflu* was estimated to be about 60 days. Table 2.4 summarizes the radionuclides which are generated by neutron activation in the material, with the related half-lives and the evaluated activities at the end of an irradiation and after 60 days. The values have been estimated from the experimental activation reaction rates obtained with the irradiation of powders carried out for the NAA.

After the 60 days, the compression tests were set-up at the Department of Mechanical and Industrial Engineering of University of Brescia. The researchers of the local Laboratory of Science and Technology of Materials have experience both in the treatment of materials exposed to neutron irradiation and in the evaluation

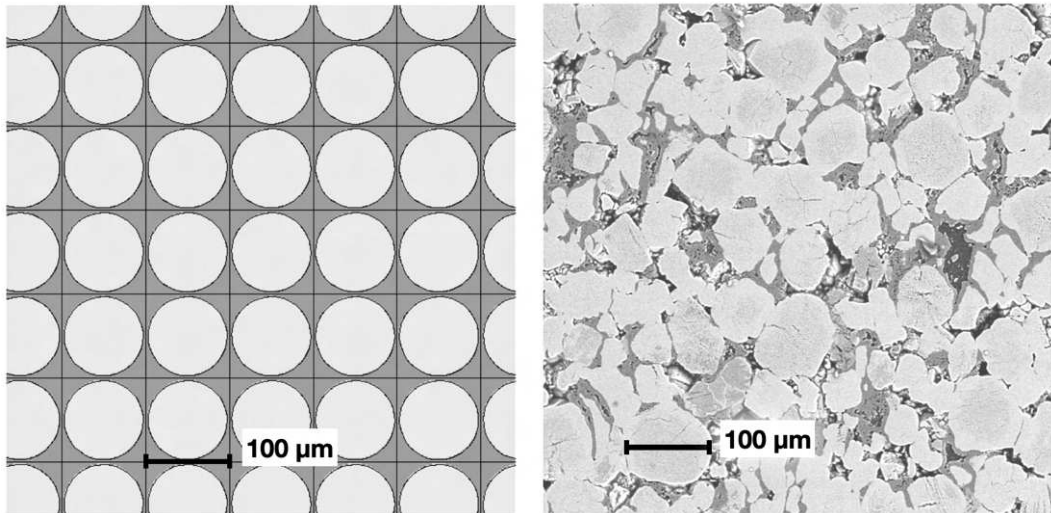


Figure 2.21: On the left, the MCNP6 geometry of the lattice built to simulate the microstructure shown on the right (obtained by the third production procedure)

of stiffness and mechanical resistance in solids.

Although the irradiated *Alliflu* were safe to handle at the time of the experiment, the compression tests were carried out with the samples placed in plastic bags (Figure 2.22). In this way, we were able to collect all the residues after the breakage of the material. The residuals returned at L.E.N.A. in Pavia after the experiments, for their correct disposal as radioactive waste according to the legislation.

2.3.1 First round of measurements

A set of 14 samples with variable density from 2.0 to 2.8 g/cm³ was available to be compared with the 3 irradiated ones for the first round of measurements. These samples were tested without irradiation to study the mechanical resistance of the new material. To maintain the same experimental conditions between irradiated and not irradiated samples, also this set was tested with the specimens inserted in plastic bags.

We used the universal testing machine INSTRON[®] model 3366 [49], with maximum force capacity of 10 kN (Figure 2.22). Each specimen was compressed between the parallel plates of the machine with a gradually increasing axial stress, until its total breakage or up to the maximum possible load. Breakage, in fact, was not obtained for every sample, indicating the need for a testing machine with a greater force capacity.

The stress-strain curves [50] obtained for *Alliflu* specimens during this first round of compression tests is shown in Figure 2.24 (the curve falls to zero where the sample breaks). These initial results indicated a good mechanical resistance

Table 2.4: Half-lives and specific activities of radionuclides produced via neutron activation in *Alliflu*

radionuclide	$T_{1/2}$	A [Bq/g] at the end of the irradiation	A [Bq/g] at 60 days from the irradiation
Al-28	2.414 min	3.5×10^9	0
As-76	1.0778 d	2.8×10^5	4.9×10^{-12}
Br-82	35.30 h	5.2×10^2	2.7×10^{-10}
Co-60	5.2714 y	9.5×10^1	9.2×10^1
Fe-59	44.503 d	6.1×10^0	2.4×10^0
Ga-72	14.10 h	2.2×10^4	~ 0
Mg-27	9.458 min	1.5×10^6	0
Na-24	14.9590 h	1.9×10^7	~ 0
Sb-122	2.7238 d	1.7×10^2	3.9×10^{-5}
Sb-124	60.20 d	6.4×10^0	3.2×10^0
Sc-46	83.79 d	4.1×10^0	2.5×10^0
Zn-65	244.26 d	3.4×10^1	2.9×10^1

of the material, both before and after the long exposure to neutron irradiation in the reactor. Samples with higher density, despite being more fragile during the production process⁴, showed better mechanical properties, breaking with higher loads. The 3 irradiated samples (the black curves) showed a more complex behaviour compared to the non-irradiated ones. From these results, however, it was not possible to clearly extrapolate the effect of irradiation on the mechanical properties of the material, nor the dependence of them on the density. These aspects needed further research. The second round of measurements was designed to better understand the effects of density and of neutron irradiation on the mechanical resistance, with a different machine and a greater number of *Alliflu* samples.

2.3.2 Second round of measurements

The second round of compression tests was carried out at the Metallurgy Laboratory of the Department of Mechanical and Industrial Engineering of University of Brescia, where a universal testing machine INSTRON® model 3369 is available. By using such machine, this time it was possible to apply on the specimens a force up to 50 kN.

A set of 30 samples was prepared for this second round, divided into 3 density ranges. 12 of them were irradiated in the reactor, again for 6 hours in the Central Thimble to reproduce the effects of about 1000 clinical treatments, while 18 were subjected to compression tests without being irradiated.

For the irradiated samples, absorbed dose was calculated using a detailed

⁴Several samples of high-density *Alliflu* broke during the extraction from the graphite molds.



Figure 2.22: Experimental set-up for the first round of compression tests on Alliflu samples

MCNP6 model of the TRIGA reactor. This model, validated in the thermal column ad described in [51], was recently renewed to take into account a major change in the position of the fuel elements in the core. This new model has been validated with neutron flux measurements along the Central Thimble [52]. The geometry of the set-up has been reproduced by simulating the plastic holders and the *Alliflu* samples stacked in the position of the central thimble where the neutron flux is better simulated. Tally F4 was used to calculate the neutron fluence and tally F6+ was used to calculate the total dose (from neutrons and photons) absorbed by the samples, with KERMA approximation, in a coupled neutron-photon transport run. Figure 2.23 shows the MCNP geometry of the holders inserted into the Central Thimble. Table 2.5 lists the results of the simulations.

To date, the 12 irradiated samples are kept at the reactor to decay before being tested for resistance. Thus, only the results regarding the 18 non-irradiated samples are available. Their density values are listed in Table 2.6.

The stress-strain curves corresponding to these samples are shown in Figure 2.25. The effect of the density on the mechanical properties of the material is now more evident: the higher the density of a specimen, the higher is the load at which its complete breaking occurs.

Furthermore, from the slopes of the stress-strain curves it is possible to infer the dependence of the material stiffness on the density. The slope of the stress-strain curve in the initial section (i.e. in the range of linear proportionality of stress to strain) is in fact the Young's Modulus [53]. The Young's Modulus -or

2.3. Mechanical resistance

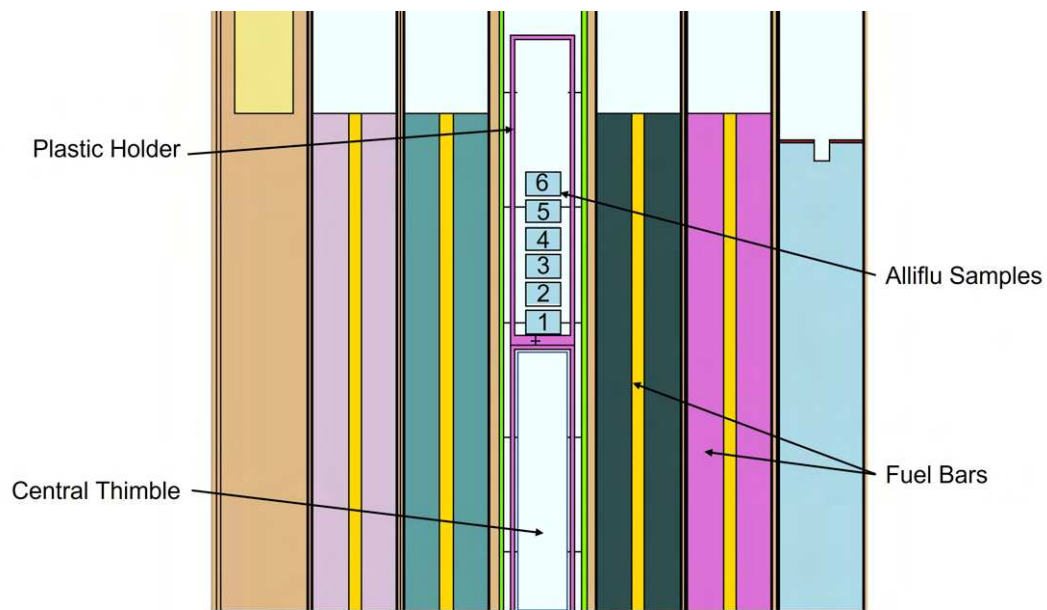


Figure 2.23: MCNP geometry of the set-up of Alliflu irradiation inside the Central Thimble of the TRIGA reactor.

Elastic Modulus- is defined as the ratio of stress below the proportional limit to the corresponding strain, and is a measure of the rigidity (or *stiffness*) of a material: to a greater modulus corresponds a stiffer material, being smaller the elastic strain resulting from the application of a given stress.

From the stress-strain curves of Figure 2.25 it is evident that low-density samples (with density up to 2.26 g/cm^3 , referring to Table 2.6) exhibit a variable Young's Modulus increasing with the density. While above a certain density value, all the tested specimens have the same Young's Modulus, which results about 5 GPa. The density threshold may reasonably represent the minimum value below which the material is not completely sintered, being comparable to a compacted powder more than to a solid.

Table 2.5: Simulated fluence and absorbed dose in the Alliflu samples irradiated in the Central Thimble of the TRIGA reactor for 6 hours at 250 kW. The number in the column samples correspond to the positions shown in Figure 2.23. Statistical errors are below 1%.

Sample position	neutron fluence [10^{17}cm^{-2}]	total dose [10^6Gy]
1	2.67	9.24
2	2.49	8.23
3	2.30	7.45
4	2.12	6.89
5	1.93	6.38
6	1.77	6.22

Table 2.6: Density values of the 18 Alliflu samples tested via compression tests concerning their mechanical resistance in the second round of measurements

Low density		Medium density		High density	
Sample ID	Density [g/cm ³]	Sample ID	Density [g/cm ³]	Sample ID	Density [g/cm ³]
1	1.98	17	2.35	56	2.66
55	2.00	28	2.41	9	2.76
4	2.02	21	2.43	13	2.81
43	2.04	65	2.48	14	2.85
5	2.07	22	2.51	11	2.89
18	2.26	16	2.62	29	2.91

2.3. Mechanical resistance

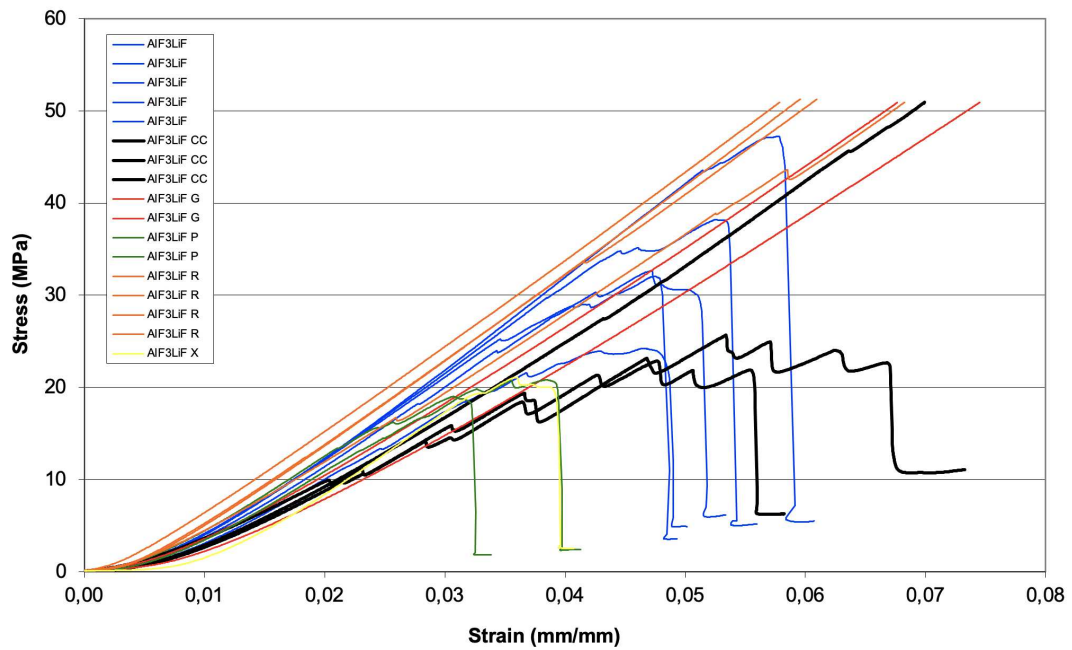


Figure 2.24: Stress-strain curves of Alliflu samples from the first round of compression tests

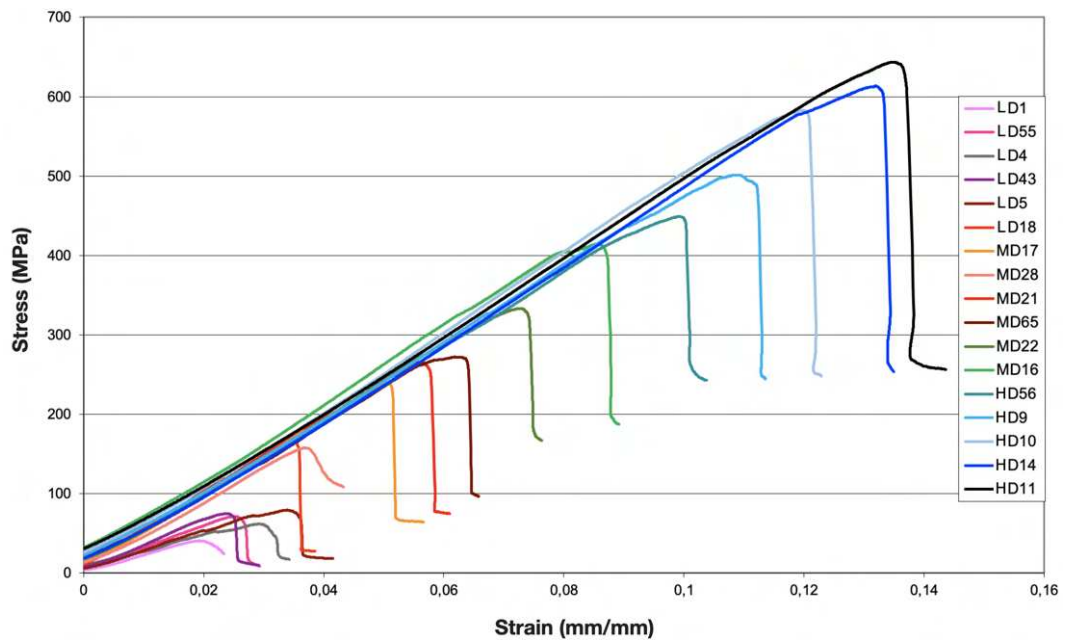


Figure 2.25: Stress-strain curves of Alliflu samples from the second round of compression tests

Spectrum modification by Alliflu

One of the goals of the present work was to experimentally validate the moderation properties of *Alliflu*. In fact, since densified lithiated aluminum fluoride is a new material, there are no experimental data to make a comparison with the Monte Carlo simulations concerning its interaction with neutrons. The realization of *Alliflu* pushed the need of carrying out the first neutron spectrometry of neutrons moderated by solid AlF_3 . This would provide a solid base for the reliability of the design of the clinical neutron beam.

The presented study envisaged the irradiation of increasing amounts of *Alliflu* with neutrons of proper energy, and to collect the emerging spectra for comparison with simulated results. The experimental activity and the simulations performed are described in the following paragraphs.

3.1 Materials and methods

Being the INFN-RFQ not yet accessible, we used as neutron source the CN accelerator available at the Legnaro National Laboratories of INFN [54]. CN is a “Van de Graaff” electrostatic device accelerating 5 MeV protons with maximum current of $3 \mu\text{A}$. It can be coupled to a Be target (Figure 3.1) to produce a neutron beam with the same spectral characteristics as the one in the RFQ-based facility, different only in intensity.

Thanks to an established collaboration with *Politecnico di Milano* and its spin-off RAYLAB Srl [55], it was possible to use two detectors for the acquisition of neutron spectra. The two detectors, described in Figure 3.2, are:

- Active Converter Spectrometer (ACSpect)
- Direction-aware Isotropic and Active MONitor (DIAMON)



Figure 3.1: Beryllium target used at the CN proton accelerator of LNL to obtain the neutron beam. The source can be approximated as point-like with neutrons exiting from the point circled in red on the left. The two metal semicircles around are part of the cooling system

ACSpect [56] is an innovative two-stages spectrometer with high energy and spatial resolution. It is based on a Polyvinyl Toluene scintillator coupled through a collimator to a monolithic silicon telescope (MST). The plastic scintillator works as an “active” recoil-proton converter, converting neutrons into recoil-protons while measuring the energy deposited by the latter. The MST measures the residual energy of recoil-protons downstream of the converter and discriminates them from the photons related to the neutron field.

ACSpect was designed and developed by the Nuclear Measurements group of the Energy Department of *Politecnico di Milano* and used for the first neutron spectrometry of Be(p,n) neutron spectrum at 5 MeV [32] before being optimized for the measurements presented here. The optimization of the detector is the subject of a Master thesis of the *Politecnico di Torino* [57] and of an article, recently submitted [58].

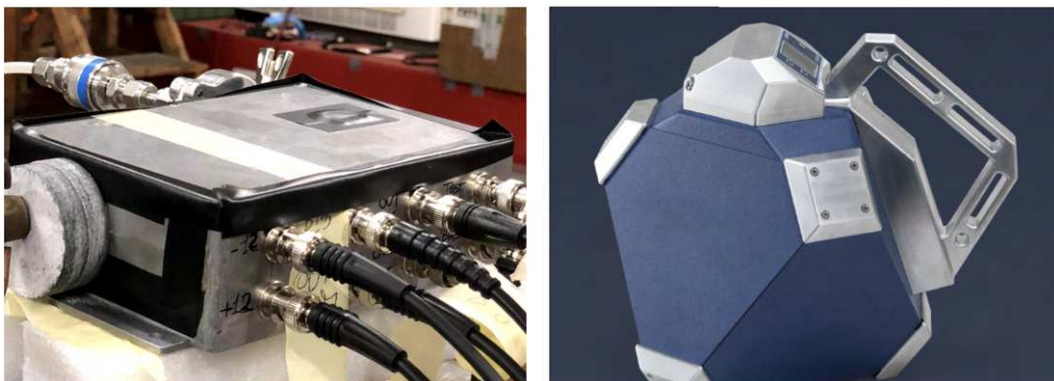


Figure 3.2: Neutron detectors used in the described measurements: ACSpect (left) and DIAMON (right)

DIAMON [59] is a neutron moderation spectrometer providing spectral, directional and dosimetric capabilities in a single device, with real-time response through a high-level graphical user interface. DIAMON was implemented by the Nuclear Measurements group of *Politecnico di Milano* in collaboration with RAY-LAB and it can measure the neutron energy spectrum with low energy resolution but in a wide energy range, from thermal to fast energies, giving very precise integral information.

Initially, simulations with no *Alliflu* were carried out, to make a preliminary comparison with the experimental data available concerning the neutron source at CN [32]. The neutron source implemented in the simulation is point-like, and it was simulated in [60]. It replicates a neutron source due to 5 MeV protons impinging on a Be target, with angular distribution reproduced from the experimental data acquired at CN with the first version of ACSpect [61]. F4-type tallies were used in the MCNP6 simulation, with the same energy bins as in [32], in the frontal direction with respect to the proton beam. The result of the tally was multiplied by the detector sensitive area (0.01 cm^2) and by the normalization factor $2.58 \times 10^9 \mu\text{C}^{-1}$, and divided by energy bin and solid angle. The normalization factor used is reported in [60], and differs from that used in [32] due to the angular distribution of the source. The solid angle was determined starting from the efficiency, determined in a dedicated simulation with the same geometry and a monoenergetic, isotropic point-like source.

The comparison of the simulated values with the experimental data is reported in Figure 3.3, showing a good agreement. The simulations reproduce the experimental set-up of ACSpect detector located in front of the beam-line in the forward direction and without any moderator, as shown in Figure 3.4. This step verified the correctness of the simulated source, enabling its use for the subsequent simulations.

3.2 Measurements with *Alliflu* tiles

We carried out two experimental campaigns at the CN accelerator using *Alliflu* tiles. The moderator elements used are shown in Figure 3.5: *Alliflu* tiles with square or circular section, having 5 cm side or diameter respectively. They were created by sintering about 50 g of $\text{AlF}_3 + \text{LiF}$ powder with the first prototype of sintering machine, and they have variable density. As described below, the measurements were carried out with increasing thickness of *Alliflu* to detect its effect on the acquired spectra. One detector or the other were used, according to the necessities.

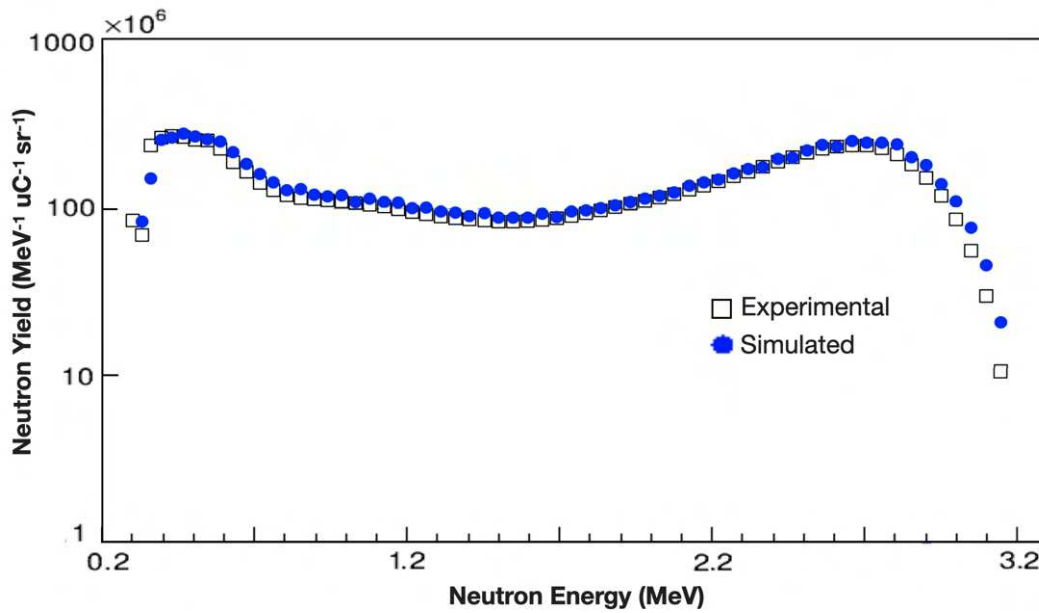


Figure 3.3: Comparison between simulated values and experimental data from [32], for the set-up with ACSpect detector located in front of the beam-line in the forward direction and with no moderator (next figure).

3.2.1 First experimental campaign

The first round of measurements was dedicated to the optimization of the methods, the test of the detectors and their set-up. In that occasion, the CN accelerator worked at very low current (20-60 nA), thus we focused on acquiring spectra for small moderator thickness.

In this experimental campaign, spectra were acquired with DIAMON for 0, 1.15, 2.16, 4.47 and 6.63 cm of moderating *Alliflu* elements, and with ACSpect for 0, 1.15 and 2.16 cm only. This detector, in fact, has low efficiency ($\sim 10^{-6}$) and requires long acquisition times. While ACSpect was placed in contact with the last *Alliflu* element (Figure 3.6), in the measurements with DIAMON the distance between the detector and the moderator end was set to 130 cm. In this case, spectra were collected for each tested *Alliflu* thickness, with and without a shadow cone (Figure 3.7). The shadow cone has a total length of 50 cm, 20 of lead and 30 of polyethylene, and it is used to shield the direct contribution from the target. This allows evaluating the scattered neutron component coming from the surrounding materials, obtaining the background to subtract from the direct measurements [62].

The comparison between the open-beam neutron spectrum acquired with ACSpect and that previously measured by Agosteo et al. [32] and with the one reported in [63], showed good agreement. Due to low proton current and low detection efficiency, the measurement is affected by an error never lower than 10%.

Figure 3.8 shows the comparison between the experimental spectrum acquired



Figure 3.4: Experimental set-up of ACSpect detector located in front of the beam-line in the forward direction and without any moderator

with ACSpect for the 2.16 cm moderator thickness and the simulated spectrum in the same geometry, with good agreement over almost all the energy range. An even better agreement between simulated values and experimental data is achieved when comparing the integral flux values obtained by ACSpect, DIAMON and MCNP6 simulation, as presented in Table 3.1.

Table 3.1: Comparison between the measured and simulated integral fluence, for the different Alliflu thickness and neutron detectors

Alliflu thickness [cm]	Integral Fluence [$10^8 \mu\text{C}^{-1} \text{sr}^{-1}$]			
	DIAMON		ACSpect	
	exp	sim	exp	sim
0	3.93±0.16	4.19±0.23	5.11±0.94	4.19±0.23
1.1	-	-	4.37±0.76	3.83±0.21
2.2	2.73±0.11	3.18±0.11	3.39±0.58	3.35±0.18
4.5	1.66±0.07	1.86±0.07	-	-
6.6	1.15±0.05	1.10±0.04	-	-

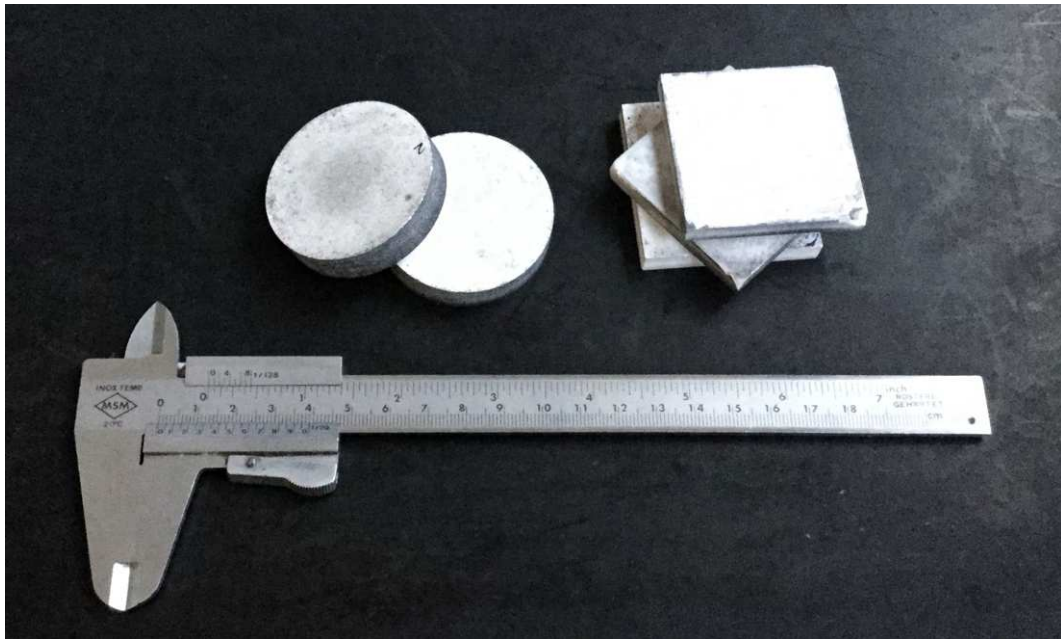


Figure 3.5: Alliflu tiles used as neutron moderator elements in the experimental measurements at CN

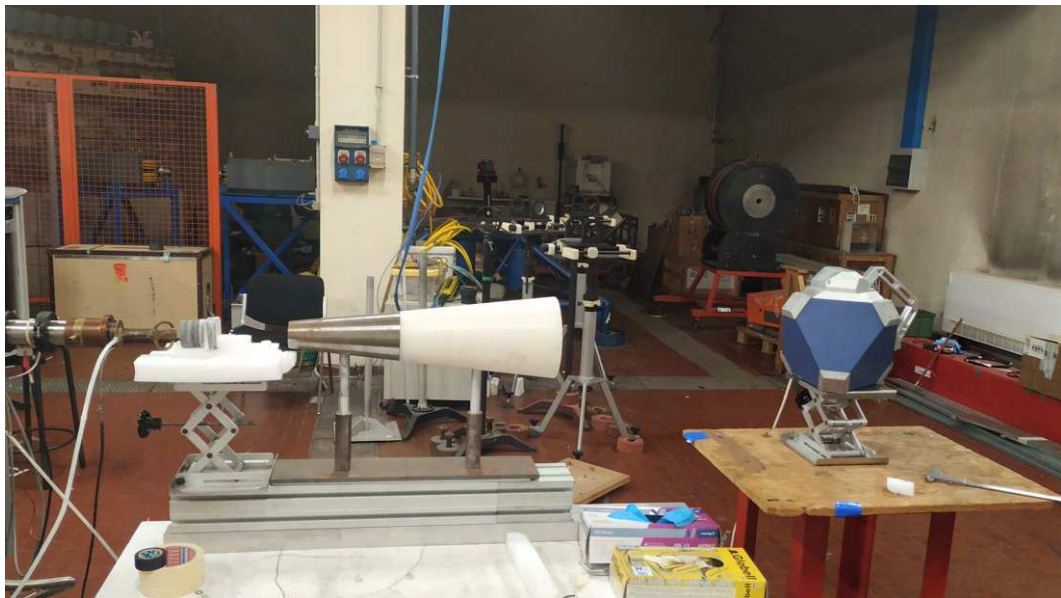


Figure 3.7: Experimental set-up with DIAMON, Alliflu elements and shadow cone

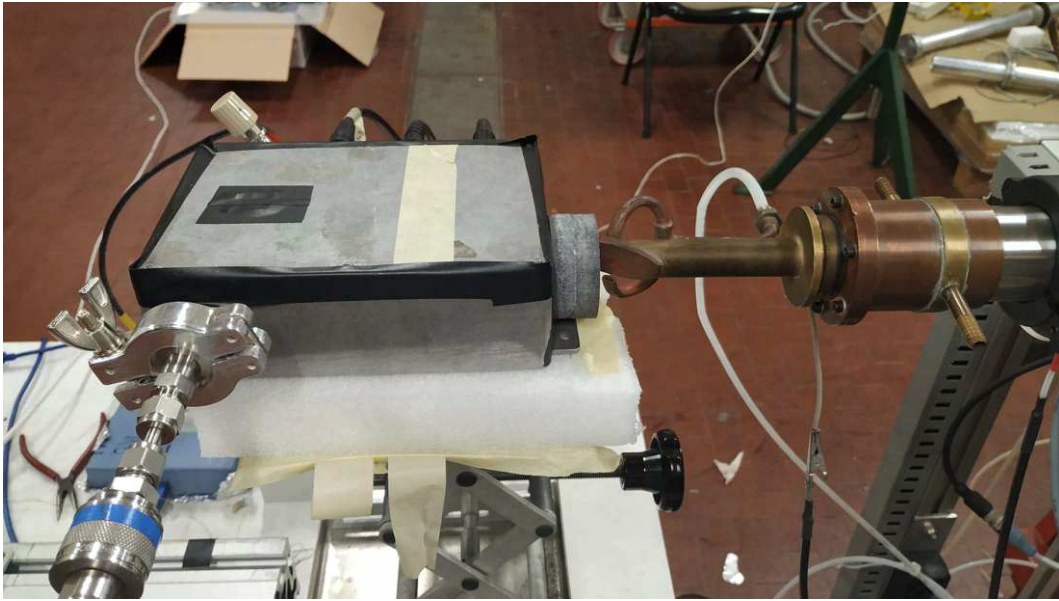


Figure 3.6: *Experimental set-up with ACSpect and Alliflu elements*

3.2.2 Second experimental campaign

In the second experimental campaign, spectra were acquired with DIAMON for 0, 1.01, 2.16, 4.03, 6.45, 8.45, 10.8, 12.8, 15 and 17.2 cm of *Alliflu*, and with ACSpect for 0 and 2.16 cm only, improving the statistics of the first campaign. The geometrical configuration between moderator and detectors was maintained as in the first set of experiments. As shown in Figure 3.9, the agreement between the simulated and the experimental fluence attenuation rate collected with DIAMON is excellent: the experimental data are well fitted by an exponential curve, almost coincident with the Monte Carlo simulations.

Regarding the shape of the neutron spectra obtained by deconvolution of DIAMON measurements, the agreement between simulations and experimental data was not perfect. This is due to a non-optimal function used to obtain the experimental spectrum. In fact, DIAMON deconvolution was optimized for an isotropic source of neutrons, which does not represent the experimental situation, with the neutron source with a specific angular distribution [32].

However, the simulation was improved in order to understand the data acquired. The geometry description was optimized to take into account the effect of the structures present in the room. In fact, the collected data likely comprised a contribution of neutrons scattered from the environment, not removed by the shadow cone. Simulations were run using the FLAG feature of MCNP, to distinguish the origin of the neutrons producing the scored tally. This was useful to understand that the contribution of neutrons reflected by the floor to the spectrum in the detector position is practically negligible. Thus we implemented in the Monte Carlo geometry other elements such as the wood tables used as the

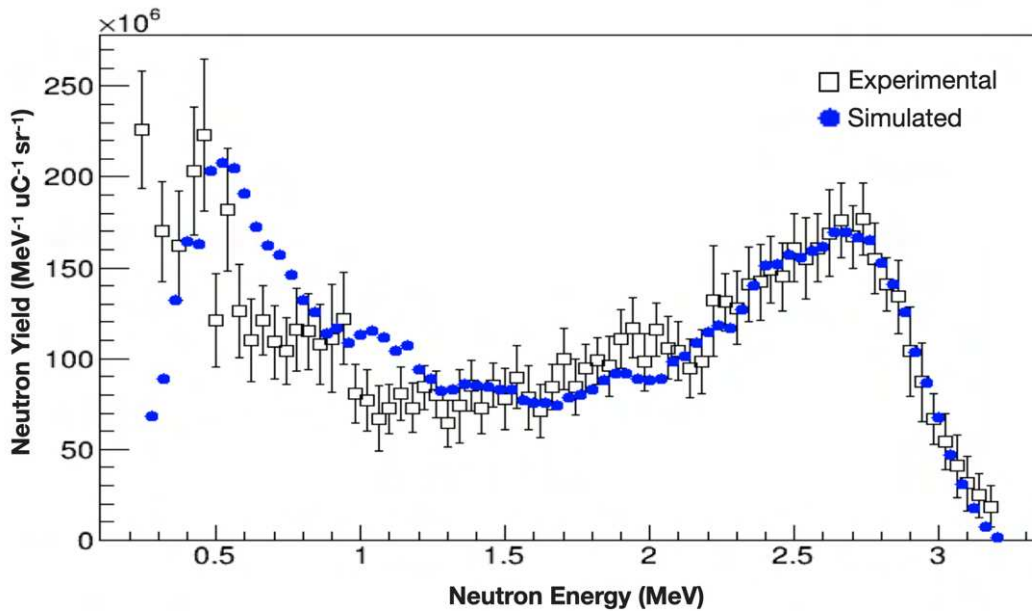


Figure 3.8: Comparison between experimental data and simulated values for the neutron spectrum from (p,n) on Be after crossing 2.2 cm of Alliflu

moderator/detector support.

3.3 Measurements with BSA prototype

The last part of this section is devoted to exploring the neutron moderation capabilities of *Alliflu* within a BSA. Objectives of this study are the design, construction and test of a BSA prototype, with the essential characteristics of the BSA developed for the RFQ, to experimentally validate the synergy between the BSA materials in moderating neutrons.

Such structure is clearly not intended to reproduce the epithermal beam with low contamination of thermal and fast neutrons obtained with the designed BSA of Figure 1.3. In fact, the CN neutron beam has the same energy spectrum generated at a point of the target in the clinical set-up. Thus, to obtain the same angular distribution and spectral composition as the clinical beam, the entire structure of the target [64] and the RFQ published in [15] would be needed. In addition, the clinical BSA is designed to shield as much as possible for radiation protection considerations, and attenuates the neutron beam by more than 3 orders of magnitude at the beam-port. Such attenuation would make the measurement impossible considered the limited CN beam time and proton current. Instead, the aim was to define a set-up having the same materials as in the original BSA, to prove that the Monte Carlo model can reproduce the beam emerging from such a complex structure. Lead was used as reflector and borated polyethylene as ab-

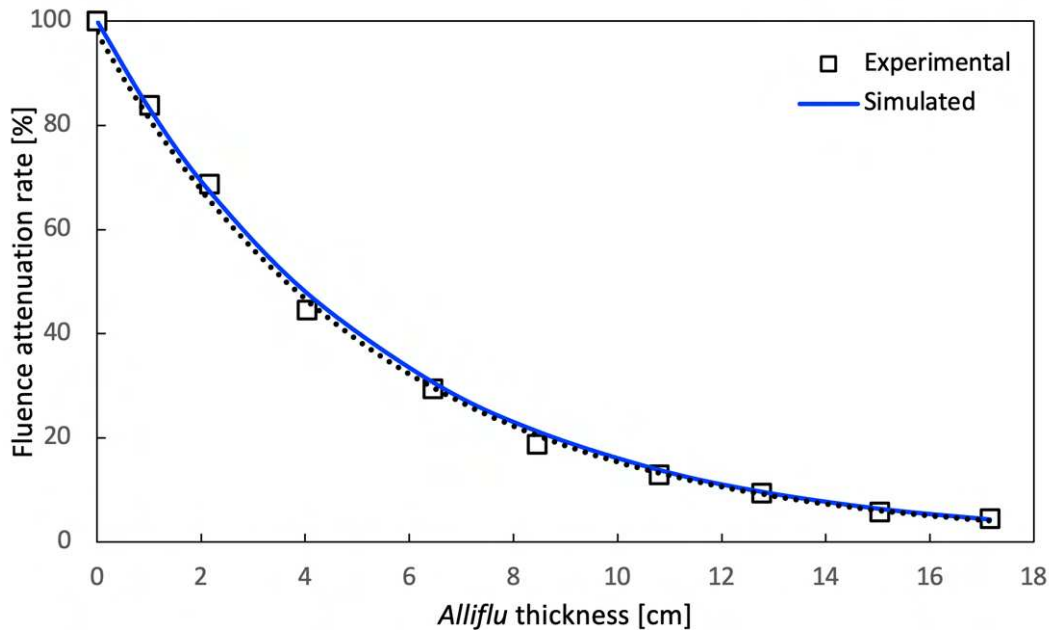


Figure 3.9: Fluence attenuation rate as a function of Alliflu thickness. The black dashed line is the exponential fit on the experimental data acquired with DIAMON, the blue solid line is the trend simulated with MCNP

sorber of the thermal component that escapes from the *Alliflu* core¹. Disks of borated polyethylene are placed at the end of the beam as collimator, while lead is around the core of the BSA, both as in the clinical BSA. In the simulation of the clinical beam, the Pb reflector is placed within the concrete walls. So, for the prototype, we implemented more polyethylene around the reflector to simulate the clinical situation.

For ease of construction, the geometry of the prototype is cylindrical, with *Alliflu* in the center, the reflector around and the absorber at the end. To avoid scattering in the structures present in the room, in the floor and in the back wall, particular attention was devoted to the collimation. To this end, several simulations were run to design the optimal geometry. This should enable the detection of significant variation of the beam spectrum increasing the thickness of the core moderator, and enhance as much as possible the epithermal component. To this aim, we added a borated polyethylene shell to enclose the lead reflector. In this way, neutrons that lose energy by scattering in *Alliflu* and in the reflector are finally absorbed, an effect similar to that of the walls of the room in the clinical beam (see next Chapter and our publication [65]).

¹In the original BSA is lithiated polyethylene (to avoid the 478 keV photons generated via the neutron capture in boron) but it is expensive and difficult to find.

3.3.1 BSA prototype: final configuration

The description of the different phases of the design is reported in Appendix B, with the results of the simulations concerning each layout tested. Figure 3.10 shows the technical drawings of the BSA prototype in the final configuration.

As anticipated, the constituents of the BSA prototype are:

- A: the *Alliflu* core: the central cylinder with 5 cm diameter and variable length, created by joining several *Alliflu* elements (tiles shown in Figure 3.5)
- B: the reflector: the surrounding Pb cylindrical shell, with length 25 cm, thickness equal to 5 cm and central hole of 5 cm in diameter for the housing of *Alliflu* (5 lead elements, length 5 cm each, to allow a further modulation of the structure)
- C: the collimator: the cylindrical shell of borated polyethylene, 65 cm diameter, perforated in the center (5 cm diameter hole), at least 15 cm long (7 disks, 2.5 cm thick each, for a total of 17.5 cm in length in order to obtain 15 cm also considering any loss of material due to the machining)
- D: the absorber: the borated polyethylene around the lead, a cylindrical shell 25 cm long and 1 cm thick (a 17 cm-diameter cylinder divided into 3 segments)

The BSA prototype has been assembled at the mechanical workshop of INFN Pavia (Figure 3.11). *Alliflu* disks were sintered with diameter 5 cm and thickness of about 1 cm to carry out measurements by increasing the thickness of the moderator up to a maximum of about 25 cm. Their density was accurately measured to be implemented in simulations reproducing the experimental set-up as accurately as possible.

As explained in Appendix B, a further polyethylene (PE) shield will be added for the next round of measurements: a cylindrical shell surrounding the entire structure upstream of the collimator. This structure, while leading to a lower epithermal spectral component, allows a higher differentiation of the neutron spectra as a function of the core moderator thickness.

Irradiation of BSA prototype

The first irradiation of the BSA prototype at LNL was carried out in September 2021. A wheeled stand was designed at the Mechanical Workshop of INFN Pavia to facilitate its transport and positioning for the experiment (Figure 3.12).

Figure 3.13 shows the experimental set-up of these measurements.

We used the DIAMON spectrometer to collect the neutron spectra, with and without shadow cone, for 7 different thicknesses of *Alliflu*, gradually inserting in the prototype each set of tiles shown in Figure 3.14.

In this measurements campaign, we did not use ACSpect because the neutron flux would be suppressed by the BSA and the needed irradiation time would

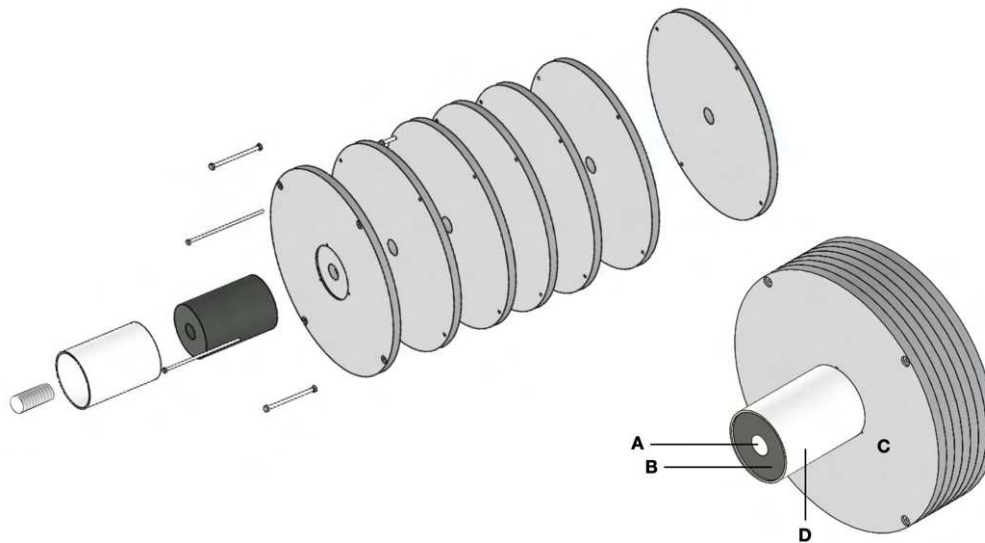


Figure 3.10: Technical drawing of the BSA prototype, courtesy of the Mechanical Workshop of INFN Pavia

be too long given the detector efficiency. Moreover, DIAMON capabilities in reconstructing the neutron spectra have been improved since the last experiments, thus the analysis should provide reliable experimental spectra to be compared to the simulated ones. At the time in which I am writing, the experimental data are under analysis. As an example of the expected results, simulated by MCNP, Figure 3.15 reports the neutron spectra at the beam-port and at a distance of 100 cm, for the two extreme configurations: BSA without moderator, and BSA with the maximum thickness of *Alliflu* inserted into the cylinder. These simulations will be validated with the experimental spectra obtained by deconvolution of DIAMON measurements.



Figure 3.11: *Assembling of the BSA prototype at the Mechanical Workshop of INFN Pavia*

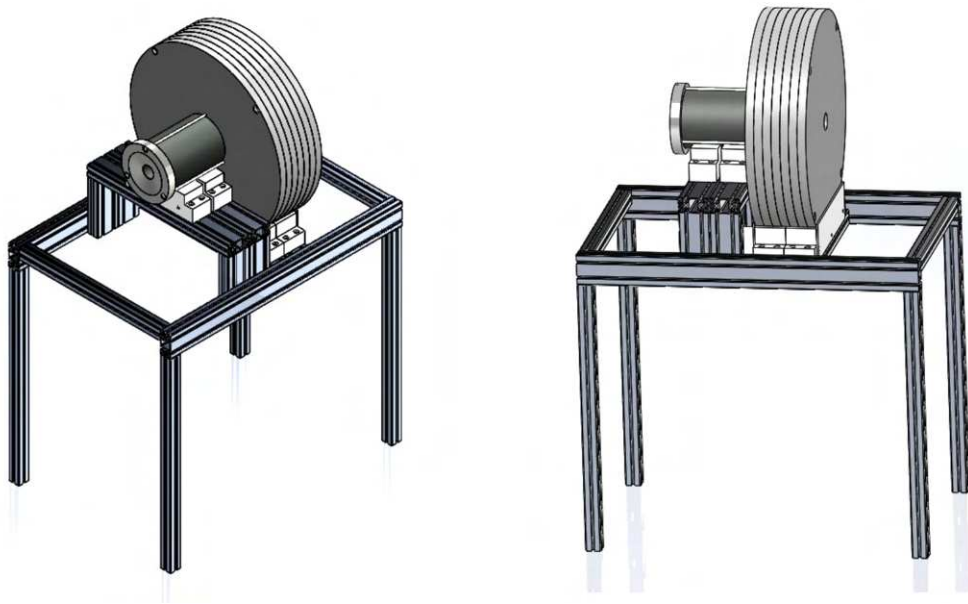


Figure 3.12: *Technical drawing of the BSA prototype with the stand designed and manufactured at the Mechanical Workshop of INFN Pavia*

3.3. Measurements with BSA prototype



Figure 3.13: Experimental set-up for the irradiation of the BSA prototype at LNL in September 2021, with DIAMON and shadow cone



Figure 3.14: Sets of Alliflu tiles used for the experiments at LNL in September 2021

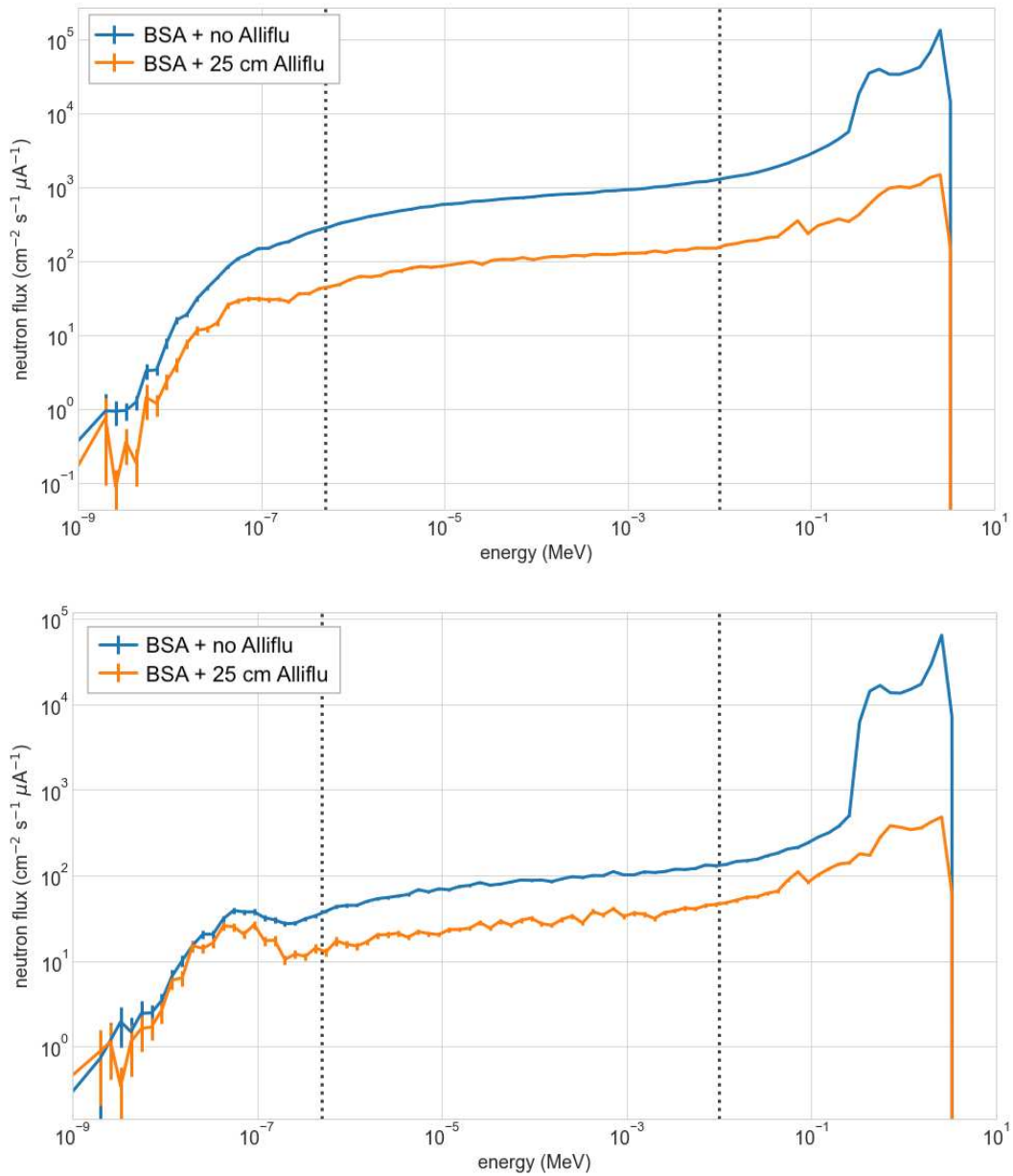


Figure 3.15: Simulated neutron spectra for the BSA prototype with 0 or 25 cm of Alliflu, at the beam-port (top) and at a distance of 100 cm from it (bottom)

Treatment room

From the studies on the BSA we move now to the evaluations concerning the design of a suitable treatment room for BNCT. Factors influencing the room configuration and the post-irradiation management of patients are connected to radiation protection issues. In particular, we carried out studies concerning the activation of the materials subjected to neutron irradiation, including the air of the treatment room and the patient. Moreover, this part of the work involved ambient and patient dosimetry studies. For the latter, the in-air doses distributions and the absorbed dose in the out-of-field organs of the patient were investigated. Special attention was dedicated to the dose absorbed by the heart, due to the emerging evidences of radiation-induced cardiovascular diseases.

A Monte Carlo model of a treatment room with dimensions $3.30 \times 4 \times 6 \text{ m}^3$ and with walls 50 cm thick was created (Figure 4.1) to evaluate the quantities of interest by running in it simulations of clinical treatments. Depending on the aspect to be studied, different Monte Carlo codes were used: MCNP6 [31], FLUKA [66] and PHITS [67].

Being interested in the transport of neutrons, MCNP would typically be the code of choice. Nevertheless, our goal included specific calculations that FLUKA and PHITS can perform more effectively, although at the expense of the representation of our neutron source: the complex distribution of neutrons from the Be target can only be realistically simulated in MCNP. In the FLUKA and PHITS simulations, approximated neutron sources were implemented, after proving their acceptability. They were in fact conservative from the dosimetric point of view.

All the simulations have been run in order to obtain an acceptable uncertainty on the results while optimizing the machine time, by implementing variance reduction techniques when needed.

Simulations were carried out both with open beam and with a phantom representing the patient, located in representative positions of a clinical treatment.

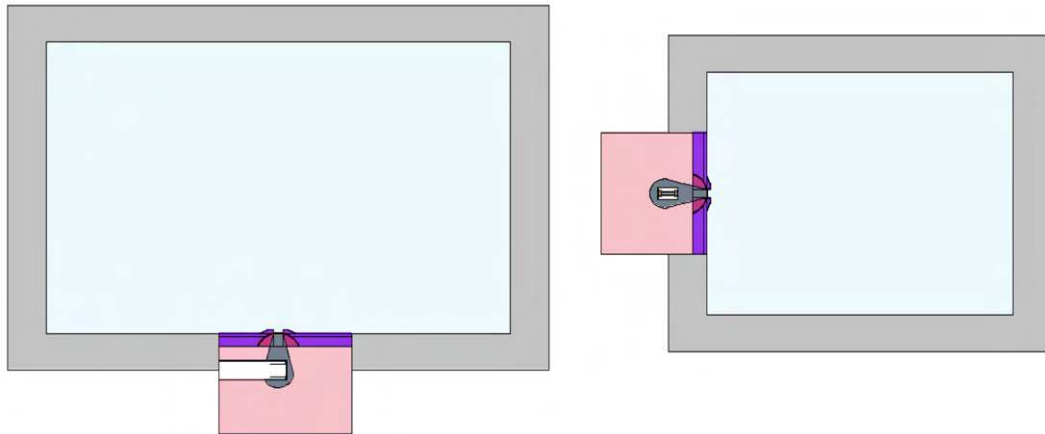


Figure 4.1: Horizontal (left) and vertical (right) sections of the MCNP6 model of the treatment room

4.1 Neutron activation of the air

The first evaluation concerned the neutron activation of the air. This is an important aspect to consider since the air of the treatment room is exposed to an epithermal neutron flux of the order of about $10^9 \text{ cm}^{-2} \text{ s}^{-1}$. The most relevant aspect is the activation of argon, a noble gas naturally present in air in percentages around 0.9%. From the neutron capture in argon-40 the radioactive isotope Ar-41 is produced, β^- emitter with half-life of 109.34 minutes [68]. Due to its nature as noble gas, it is difficult to filter argon out of the air of the treatment room. For this reason, the best strategy to contain the induced radioactivity in the air of the room is to limit the production of Ar-40. The neutron activation of argon in air due to a typical treatment was simulated to determine the induced activity and its dependence on the material of the room walls.

Five different materials were considered:

- ordinary concrete
- concrete with the add of 5% in mass of natural abundance boron
- ordinary polyethylene
- polyethylene with the add of 7% in mass of natural abundance lithium
- barite concrete with the add of 0.5% in mass of natural B

The induced radioactivity in the air can be derived from the number of atoms of argon-41 created by the neutron irradiation. This quantity is evaluated by calculating the reaction rate of neutron activation of Ar-40 in the air of the irradiation room. The reaction rate R is the number of atoms of argon-41 created per unit time, providing the production rate of radioactivity in air due to the $^{40}\text{Ar}(n,\gamma)^{41}\text{Ar}$ reaction.

4.1. Neutron activation of the air

To obtain a reliable estimation of the correct air activity, it is also necessary to take into account the decay of ^{41}Ar and the ventilation system of the room, which expels part of activated argon in every air change. The rate of air changes, equal to 15 per hour, can be described as a decay constant λ_{air} that adds up to the radioactive decay constant λ_{dec} .

Therefore, the evolution of air activity over time is given by:

$$\frac{dA}{dt} = R\lambda_{dec} - (\lambda_{dec} + \lambda_{air})A \quad (4.1)$$

For Ar-41, λ_{dec} is equal to $(157.7 \text{ minutes})^{-1}$, while with 15 air changes per hour λ_{air} is equal to 0.25/minute.

Considering the situation at equilibrium $\frac{dA}{dt}=0$, thus we have:

$$A = \frac{R \lambda_{dec}}{\lambda_{dec} + \lambda_{air}} \quad (4.2)$$

Since $\lambda_{dec} \ll \lambda_{air}$, it is possible to neglect λ_{dec} at the denominator, obtaining the following relation for the final specific activity of air at equilibrium:

$$a = \frac{A}{m} = \frac{R \lambda_{dec}}{\lambda_{air} m} \quad (4.3)$$

The specific activity in air have been calculated from the simulated reaction rates for every tested walls composition. The results were then compared with a conservative limit of 1 Bq/g.

In Table 4.1 the calculated specific activities are listed for every tested composition, showing that the design goal is achieved only with walls of borated concrete or lithiated polyethylene.

Since concrete presents other practical advantages over polyethylene, as the ease of construction and costs of materials, borated concrete is the material that has been considered as the most suitable for the treatment room. Even with a small percentage of boron, borated concrete is able to suppress the activity induced in air. This is due to neutron capture in ^{10}B , the same reaction that is exploited in BNCT treatments, reducing the thermal neutron flux in the room and thus the reaction rate due to neutron activation.

While the issue of external dose rate is easier to control by acting on the shielding thickness of the room wall, the neutron activation of air was proven as a major issue affecting the choice of the materials for the treatment room. Notably, the studies in this work showed that this constraint forced a change in the clinical BSA design. The original BSA was designed to maximize the clinical effect, by evaluating the dosimetry in the tumour and in the surrounding healthy tissue in relevant clinical ([16], [69]). When tested for air activation, the optimized beam exceeded the 1 Bq/g limit with any composition of the walls, thus requiring further modification of the BSA design. The final BSA showed in Figure 1.3 complied

with the requirement. This has shown a very important aspect when designing a clinical beam: radiation protection evaluations can be an important constraint and a necessary feedback for the beam design. The same holds for out-of-beam in-patient dosimetry, as described in [15]. A very appealing beam from the point of view of therapeutic potential could have serious limitations from the point of view of safety, impairing its use in clinical treatment.

Table 4.1: Air specific activity in the treatment room at equilibrium, due to argon activation with open beam

Walls composition	a [Bq/g]
concrete	5.632
borated concrete	0.070
polyethylene	2.578
lithiated polyethylene	0.223
borated baritic concrete	1.777

4.2 Neutron activation of the walls

Borated concrete was identified as the optimal material for the walls of the treatment room. However, concrete contains elements which can be activated, possibly becoming radioactive when exposed to high-fluence neutron irradiation. Therefore, neutron activation of concrete walls is a relevant factor to assess in the design of the treatment room for a clinical facility.

This aspect was evaluated by calculating the activation reaction rates in a simulation of a clinical treatment in the Monte Carlo model of the room. To this end, F4-type tallies were used, coupled to the appropriate tally modifiers. To better visualize the activation distribution in the depth of the walls, mesh-type F4 tallies have been used, with cubic elements having 10 cm side. Mesh tallies map a simulated quantity over a spatial reticulation independent of the geometry. They also allow the visualization of the results distribution in a color-scale plot [70].

The simulations were carried out with the walls made up of ordinary and borated concrete, to point out the effect of the percentage of boron added in the normal composition in decreasing the neutron activation.

The composition used in the simulations for ordinary concrete is listed in Table 4.2, which shows the elements present in concrete with their mass percentages. Borated concrete was implemented with the same composition, added with the 5% of natural B (thus 1% of ^{10}B and 4% of ^{11}B), and the percentages of other elements re-scaled to a total of 95%.

The activation reactions taken into account¹ are:

¹We focused on the reactions potentially significant from a radiation protection viewpoint, considered the abundance of the target isotope, the cross section of the reaction and the decay mode of the produced radionuclide.

4.2. Neutron activation of the walls

- $^{27}\text{Al}(n, \gamma)^{28}\text{Al}$
- $^{40}\text{Ca}(n, \gamma)^{41}\text{Ca}$
- $^{41}\text{K}(n, \gamma)^{42}\text{K}$
- $^{26}\text{Mg}(n, \gamma)^{27}\text{Mg}$
- $^{23}\text{Na}(n, \gamma)^{24}\text{Na}$

Since the major contribution for the considered reactions comes from low-energy neutrons, the mapping of thermal neutron flux is a significant indicator of the distribution of neutron activation. Figure 4.2 shows the simulated distributions of thermal neutron flux in the mesh superimposed on room and walls, when the wall material is ordinary and borated concrete respectively. Compared to the ordinary concrete, the distribution for borated concrete shows a sharp decrease of neutron flux going deeper into the walls, down to very low values in the outermost layer.

Accordingly, Figure 4.3 shows the activation reaction rates per cm^3 of calcium, the isotope with the highest activation rate among the concrete elements. The advantage of B add is evident in the reduction of Ca activation for a factor higher than 100 already in the first internal layer.

Table 4.2: Composition of ordinary concrete (in mass percentages) used in the simulations of this work

	O	C	Ca	Al	K	Na	Fe	H	Mg	S
%	49.56	31.35	8.26	4.56	1.92	1.71	1.22	0.56	0.24	0.11

To assess the time evolution of the dose due to activated materials, we explored the capabilities of the FLUKA code [66]. FLUKA is a useful code for neutron activation studies: unlike MCNP, it allows to generate and transport decay radiation in the same simulation in which radioactive nuclides are generated. The amount of produced radionuclides, their time evolution and the residual dose after their decay can be obtained in the same run, for a given irradiation set-up and for an arbitrary series of cooling times.

As anticipated, it is not possible to reproduce with FLUKA the neutron source from the INFN-RFQ accelerator coupled to the Be target with the same spectral and angular details as allowed by MCNP. Thus, we tested the suitability of an isotropic point-like neutron source placed in the central position of the Be target, with energy uniformly distributed between 0 and 3.5 MeV. The same source was used to calculate the reaction rates with MCNP, obtaining a slight overestimation compared to the detailed source (2%). This uniform isotropic source can thus represent a reasonable approximation for our purposes. The strategy to assess the suitability of a facility concerning radiation protection issues is in fact to assume conservative conditions. This was also true for the estimated irradiation time, set

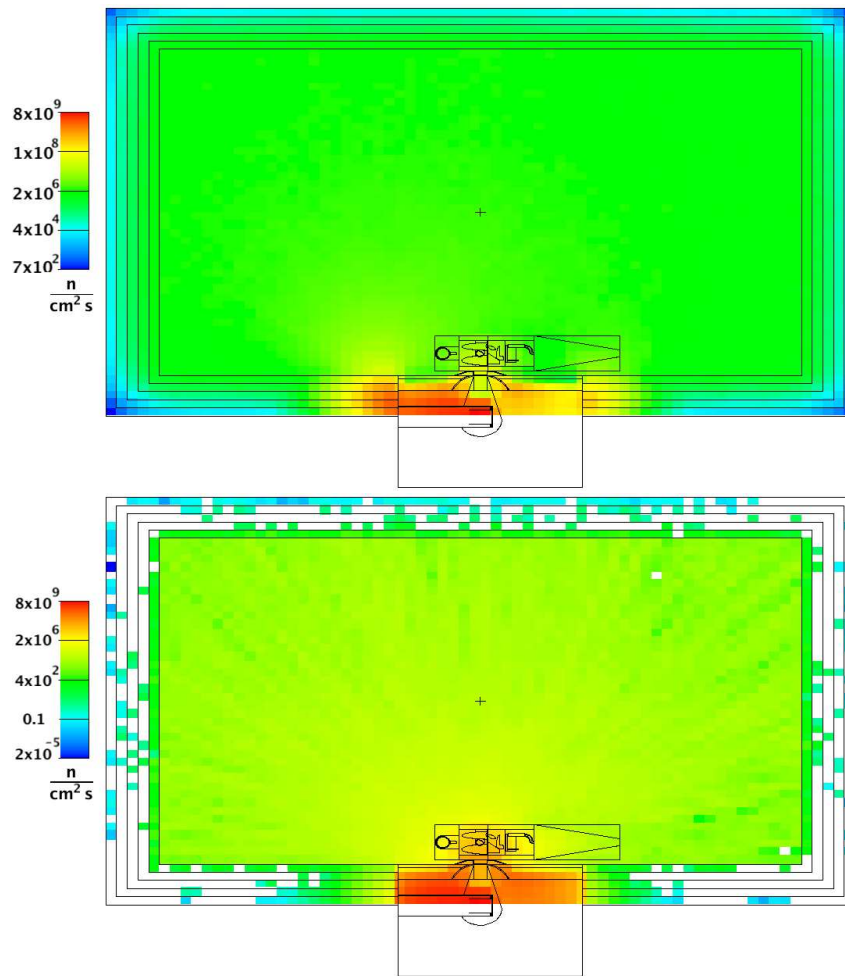


Figure 4.2: MCNP6 simulation of thermal flux distribution in a treatment room with walls of ordinary (left) and borated (bottom) concrete

as 2 hours, even if the typical patient treatment is between 30 and 70 minutes. These settings were implemented in FLUKA simulations. The specific tools available in FLUKA for activation studies have been used: the “RADDECAY” card has been activated, enabling the production of radioactive nuclides and their decay simulation.

FLUKA simulations estimated the radioactivity induced by the neutron activation of concrete elements in the total volume of the walls. The resulting activity values at the end of the treatment in a room with ordinary or borated concrete walls are shown in Table 4.3. The comparison between the two cases proves that the boron presence in the walls reduces the activity of the walls by at least one order of magnitude.

4.2. Neutron activation of the walls

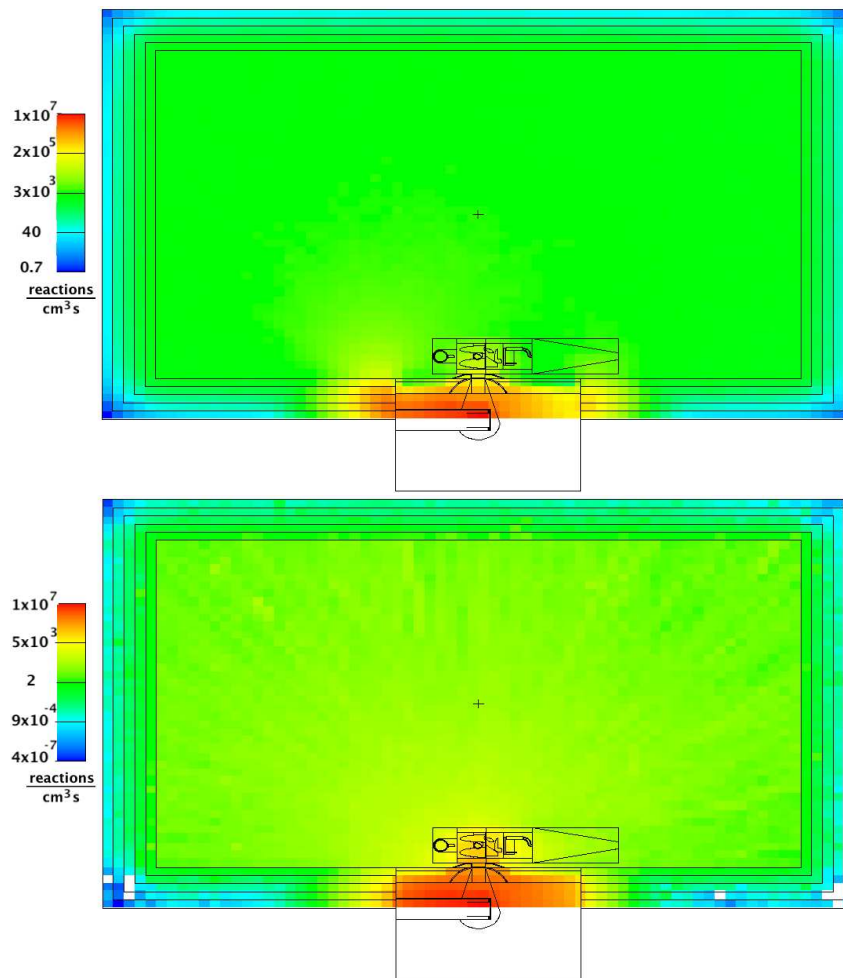


Figure 4.3: MCNP6 simulation of activation reaction rate per volume unit of Calcium in ordinary (top) or borated (bottom) concrete walls of the treatment room

Table 4.3: Induced radioactivity values in the walls at the end of a 2 hours treatment simulated via FLUKA, for a room with ordinary or borated concrete walls

Isotope	A [kBq]	
	ordinary concrete	borated concrete
Al-28	5.7×10^7	4.8×10^4
Na-24	3.3×10^6	2.8×10^3
Mg-27	7.8×10^4	-
Ca-45	710	0.24
K-40	6.6×10^{-10}	6.0×10^{-10}

4.3 Neutron activation of the patient

The neutron activation of patients is an important aspect for the safety of those who will come into contact with them after the treatment, and plays a role for the after-treatment management of patients and for the organization of the facility layout. In fact, the design of the building also depends on the need of specific facilities such as hot restrooms to store radioactive urine or separate rooms to host patients after irradiation.

Table 4.4: Composition in mass percentages of standard urine [71] and soft tissue of MIRL phantom [31]

	H	C	N	O	Na	P	S	Cl	K	Fe
urine	11.0	0.5	1.0	86.2	0.4	0.1	-	0.6	0.2	-
soft tissue	10.5	41.4	3.4	43.9	-	0.1	0.02	0.02	0.02	0.01

For this reason, we calculated the residual radioactivity of the elements composing the patient tissues and the urine. The compositions to which we made reference for the two materials are listed in Table 4.4. A phantom representing the patient in position for a clinical treatment was implemented in the simulated geometry of the room. Three different treatment positions were tested, representative of a clinical irradiation of the head and neck district, of the thoracic area and of the lower limb region (Figure 4.4). The dependence of the evaluated quantities on the material chosen for the wall composition was verified, simulating the irradiation both in a room with ordinary and borated concrete walls.

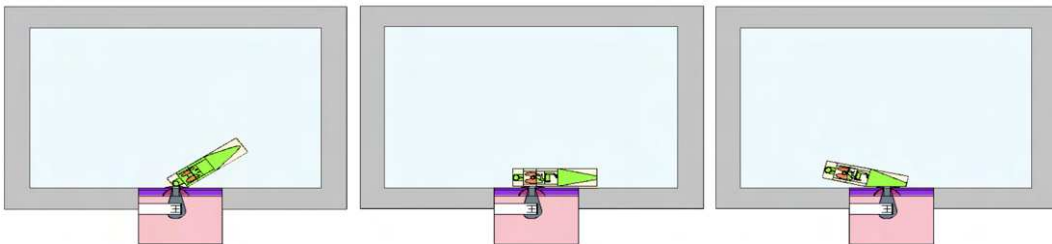


Figure 4.4: Horizontal sections of the MCNP6.1 treatment room model with the MIRL phantom in three representative positions for a clinical irradiation (from left to right: beam on head and neck district, thoracic area and lower limb region)

4.3.1 Residual radioactivity of urine

The phantom used is MIRL, a geometrical anthropomorphic model that represents the human anatomy with 22 internal organs and more than 100 sub-regions

[31]. To assess the neutron activation of urine, the phantom was implemented in the geometry of the room with the bladder full.

The urine composition was set with the mass percentages of Table 4.4 based on [71], modified to include a conservative quantity of sulfur² to investigate the possible issues related to its induced radioactivity at the end of a clinical irradiation. The focus was on the $^{34}\text{S}(n, \gamma)^{35}\text{S}$ reaction, which produces the isotope sulfur-35 with half-life of about 87.3 days [68]. Natural sulfur has been thus considered to be present in the bladder in a 0.2% percentage, re-scaling the amounts of other elements.

Neutron activation of the urine has been evaluated using the reaction rates R per mass unit, calculated for the reactions of interest. As neutrons reaching the bladder have low energy, threshold reactions do not occur and the activation reactions taken into account are: $^{37}\text{Cl}(n, \gamma)^{38}\text{Cl}$, $^{41}\text{K}(n, \gamma)^{42}\text{K}$, $^{23}\text{Na}(n, \gamma)^{24}\text{Na}$. The rationale for choosing the reactions is to consider those that can create, at the end of a treatment, residual activities not negligible for radiation protection. E.g. the reaction $^{35}\text{Cl}(n, \gamma)^{36}\text{Cl}$, producing the β emitter Cl-36 with half-life of the order of 10^5 years, was not considered.

The residual radioactivity of the elements in the urine was calculated from the simulated reaction rates of the neutron activation reactions, by using Eq. 2.8. The values obtained at the end of a 2-hours treatment are listed in Table 4.5, for each irradiation position and walls composition tested. It emerges that neutron activation of sulfur does not represent a problem of residual radioactivity compared to the other isotopes. The most problematic radioisotope created is chlorine-37, having the highest induced activity at the end of a clinical irradiation, however it has the shortest half-life among the isotopes considered.

Table 4.5: Residual specific activities of the urine elements, at the end of a 2-hours clinical irradiation, for each treatment position in a room with ordinary or borated concrete walls

Isotope	Half-life	Head and Neck		Thorax		Lower Limb	
		a _{ORD} [Bq/g]	a _{BOR} [Bq/g]	a _{ORD} [Bq/g]	a _{BOR} [Bq/g]	a _{ORD} [Bq/g]	a _{BOR} [Bq/g]
Cl-38	37.24 min	16.4	2.17	26.4	16.1	33.9	12.9
K-42	12.360 h	5.94	0.8	9.54	5.81	12.2	4.7
Fe-59	44.503 d	0.37	0.049	0.60	0.36	0.77	0.30
S-35	87.32 d	$5.6 \cdot 10^{-4}$	$7.4 \cdot 10^{-5}$	$8.9 \cdot 10^{-4}$	$5.4 \cdot 10^{-4}$	$1.15 \cdot 10^{-3}$	$4.4 \cdot 10^{-4}$

4.3.2 Residual radioactivity of soft tissue

For the activation of the patient entire body, a simplified phantom was used: a rectangular parallelepiped with dimension $40 \times 15 \times 170 \text{ cm}^3$ with composition

²Clinical experience suggests that traces of sulfur can be present in the urine of some patients.

equal to the soft tissue of MIRD (Table 4.4). The total volume of the phantom is overestimating the one of an average patient, but again the intent is to remain conservative.

In this case, the reactions taken into account are: $^{37}\text{Cl}(n, \gamma)^{38}\text{Cl}$, $^{41}\text{K}(n, \gamma)^{42}\text{K}$, $^{58}\text{Fe}(n, \gamma)^{59}\text{Fe}$. The resulting specific activities at the end of a 2 hours clinical irradiation are listed in Table 4.6, with their dependence on the patient position and on the wall material (ordinary or borated concrete).

Table 4.6: Residual specific activities of the soft tissue elements, at the end of a 2-hours clinical irradiation, for each treatment position in a room with ordinary or borated concrete walls

Isotope	Half-life	Head and Neck		Thorax		Lower Limb	
		a_{ORD} [Bq/g]	a_{BOR} [Bq/g]	a_{ORD} [Bq/g]	a_{BOR} [Bq/g]	a_{ORD} [Bq/g]	a_{BOR} [Bq/g]
Cl-38	37.24 min	23.5	14.3	23.5	8.88	24.7	9.48
K-42	12.360 h	1.68	0.73	1.68	0.68	1.76	0.72
Fe-59	44.503 d	$2.7 \cdot 10^{-4}$	$1.4 \cdot 10^{-4}$	$2.7 \cdot 10^{-4}$	$1.3 \cdot 10^{-4}$	$2.8 \cdot 10^{-4}$	$1.4 \cdot 10^{-4}$

Borated concrete walls reduce the specific activities at the end of a treatment by 60% and by 40%, in soft tissue and in the urine respectively. Even with borated walls, the obtained results suggest the need of special restrooms to store urine, depending on the local radiation protection regulations.

The obtained reduction in residual activities shows the efficiency of a small percentage of boron added in concrete in producing a significant difference in different aspects of radiation protection: activation of air, walls, tissues and urine.

4.4 Patient out-of-field dosimetry

The beam effect on the out-of-field organs is a significant aspect when designing a BNCT clinical facility. In fact, the dosimetry is important not only in the tumour and in the surrounding normal tissues, but also in the peripheral healthy organs. Radiation protection guidelines do not provide limits for the out-of-field dosimetry, being the focus in radiotherapy on the therapeutic effect. Still, the absorbed dose in healthy organs has been proved as a significant tool to compare different beams in terms of patient safety [15]. In this thesis, the beam ensuring the best out-of-beam dosimetry in the cited study has been employed for simulation. This beam is in fact the one chosen as the clinical candidate, ensuring optimal therapeutic potential as well as safety.

In this work, the in-patient dosimetry was evaluated from the viewpoint of the healthy organs, not directly irradiated by the clinical beam. The MIRD phantom was used also in this case, implemented in the geometry of the room in the three representative treatment positions of Figure 4.4.

The absorbed doses in the patient healthy organs were calculated through the nuclear reactions that take place in biological tissue irradiated with neutrons: the elastic scattering on hydrogen, the radiative capture in hydrogen and the capture in nitrogen with emission of protons, i.e. respectively ${}^1\text{H}(n, n'){}^1\text{H}$, ${}^1\text{H}(n, \gamma){}^2\text{H}$ and ${}^{14}\text{N}(n, p){}^{14}\text{C}$. In addition, to take into account the presence of the borated compound in the healthy organs, we considered the capture with alpha emission on boron: ${}^{10}\text{B}(n, \alpha){}^7\text{Li}$. Boron in the healthy organs was assumed to be present in a conservative concentration of 15 parts per million, with the exception of kidneys. As reported in [15], kidney, known to filter BPA, is the only organ with higher boron uptake. The concentration of boron in kidneys was thus set to 75 ppm ([72], [73]).

The dose components due to (n,n'), (n,p) and (n, α) reactions have been calculated through reaction rate tallies (F4-type). In these cases the released charged particles have a short range in tissue ($\sim \mu\text{m}$), thus all their energy is deposited within the organ where they are produced. Therefore, these dose components were calculated by multiplying the simulated reaction rate per mass unit by the Q-value of the reaction. The photons produced in the radiative capture have a mean free path large enough to leave the volume considered. Thus, for (n, γ) contribution a heating tally was used (F6-type) to calculate the dose deposited by photons in the volumes of interest. F6 calculates the energy released per unit mass in the volume of interest, and in absence of electron transport, the energy is locally deposited (kerma). The results overestimates the actual dose value, because electrons may travel in tissue and leave the volume of interest depositing part of their energy elsewhere. However, given the organ volumes, such approximation is acceptable, leading to very small correction of the true dose value. Moreover, being a radiation protection criterion, a conservative approach is always preferable.

The dose-rates due to the four described reactions were calculated in the following organs of the MIRD phantom³: adrenal glands, bladder, brain, head, heart, intestines, kidneys, liver, lungs, marrow, pancreas, pharynx, skin, spleen, stomach, testes, thymus, thyroid.

Table 4.7 shows, for each MIRD organ and treatment position, the results in the cases of ordinary or borated concrete walls. Also in this case, it is evident the reduction produced by the boron addition in the concrete. The average decrease in the patient out-of-field dosimetry produced by borated concrete is about 20% and 25% for the beam irradiating the thorax and the head-and-neck region respectively. For the treatment position with the beam in correspondence of the lower limb the average reduction reaches the 60%.

As for the air activation, also the out-of-beam dosimetry using human models appears as an important tool to guide the project of the irradiation room.

As explained in the following, due to recent evidences of radiation-induced cardiovascular diseases, we focused in particular on the doses absorbed by the heart.

³The volume of each considered organ of MIRD phantom was checked in advance through the stochastic volume Monte Carlo technique [74]

Table 4.7: Total absorbed dose-rates calculated in each organ of the MIRD phantom, for each representative treatment position and for a treatment room with ordinary or borated concrete walls.

organ	Head and Neck		Thorax		Lower Limb	
	\dot{D}_{ORD} [$\mu\text{Gy/s}$]	\dot{D}_{BOR} [$\mu\text{Gy/s}$]	\dot{D}_{ORD} [$\mu\text{Gy/s}$]	\dot{D}_{BOR} [$\mu\text{Gy/s}$]	\dot{D}_{ORD} [$\mu\text{Gy/s}$]	\dot{D}_{BOR} [$\mu\text{Gy/s}$]
adrenals	97.9	78.9	201.4	181.1	133.4	46.6
bladder	47.7	25.9	118.0	100.2	153.9	98.7
brain	686.5	666.0	232.9	178.6	87.5	14.1
head	426.5	406.5	246.1	202.8	94.5	17.5
heart	132.7	109.7	283.1	259.5	135.3	34.4
intestine	60.9	39.4	154.3	136.9	139.9	69.2
kidneys	85.7	59.7	198.8	176.4	142.8	52.7
liver	116.7	94.7	305.6	286.7	171.9	53.9
lungs	29.7	27.8	115.1	113.6	19.9	8.4
marrow	156.3	142.6	153.0	133.7	80.2	25.6
pancreas	85.4	63.5	222.0	203.9	149.1	53.2
pharynx	351.5	331.8	240.8	201.1	94.5	17.1
skin	199.3	175.6	276.7	250.6	162.2	68.5
spleen	78.3	56.5	127.0	106.5	85.8	29.6
stomach	88.1	64.0	158.7	136.4	101.1	31.4
testes	41.8	22.1	98.0	79.3	192.9	146.0
thymus	167.4	146.1	262.4	235.9	131.0	29.4
thyroid	277.2	256.6	253.8	214.8	105.9	21.9

4.4.1 Radiation-induced cardiovascular diseases

The term “radiation-induced cardiovascular disease” includes a range of deleterious side effects on the heart, unintentionally produced as a result of therapeutic irradiation of the thoracic area and coronary vessels [75]. With induced damages that can interest pericardium, myocardium, valves, conduction system or coronary arteries, it ranges from sub-clinical histopathological findings to overt clinical disease, and can lead to pericarditis, coronary artery disease, arrhythmia, cardiomyopathy, valvular dysfunction, and even heart failure.

The heart was long considered a radioresistant organ [76]. Recently it appears more and more evident how the cardiovascular risks associated to radiation exposure can affect the benefit from radiotherapy in some cancer patients [77]. In fact, even if many radiation-induced abnormalities are asymptomatic at first [78], long-term cardiac toxicities following irradiation become more relevant as the survival of cancer patients increases, with the possible development of late effects previously underestimated.

To date, there are no official published screening or prevention guidelines. Studies as [79] suggest a linear dose-response relationship between the dose ab-

sorbed in the heart and the rate of myocardial infarction in treated patients with radiotherapy. The doses reported in the cited work were converted in single-fraction using the BED formalism [80] as in Eq 4.4, with α/β the ratio of the Linear Quadratic Model (LQM) parameters and D the dose of each of the n fractions. With this conversion, the mean single-fraction dose absorbed in the hearth of the patients evaluated is 4 Gy and the risk of myocardial infarction increases considerably over 6.8 Gy.

$$D_{\text{single fraction}} = \frac{-\alpha/\beta + \sqrt{\alpha/\beta^2 + 4D(\alpha/\beta + D/n)}}{2} \quad (4.4)$$

Table 4.8: Calculated absorbed doses in the heart in the simulated BNCT treatment of conservative duration of 2 hours

walls composition	Head and Neck D [Gy]	Thorax D [Gy]	Lower Limb D [Gy]
ordinary concrete	0.96	2.04	0.97
borated concrete	0.79	1.87	0.25

To make a comparison, we estimated the total dose received by heart in a BNCT treatment with the described beam. The overall dose-rate of Table 4.7 for heart was multiplied by the irradiation time considering a 2 hours treatment. The results are shown in Table 4.8, with their dependence on the irradiation position and on the composition of the walls in the treatment room. In every position and for each of the walls configurations the absorbed dose obtained is less than or comparable to 2 Gy. However, BNCT dose is radiobiologically more effective than photons in producing damages to cells.

It is possible to convert BNCT dose values in photon-equivalent units by means of the Relative Biological Effectiveness (RBE) parameters. RBE is defined as the ratio between the absorbed doses of a reference radiation (typically γ -rays or x-rays) and of the radiation of interest which produce the same biological effect or clinical end-point [81].

Using the common RBE factors used in BNCT dosimetry [82], we converted the values of Table 4.8 obtaining a biological-equivalent dose in heart lower than 3.3 Gy (RBE-weighted). From these values, calculated in conservative assumptions, BNCT with the designed beam remains below the dose above which the risk of myocardial infarction increases considerably⁴ according to [79]. It must be highlighted that RBE formalism has been recently questioned as not representative for the expression of BNCT dose in photon-equivalent units ([83], [84]). Other formalisms, more suitable to evaluate the clinical outcome in view of the patient dosimetry have been proposed. In this work, we will employ the *photon*

⁴Since the cited studies are quite recent, unfortunately there is currently no information regarding the cumulative risk of myocardial infarction at a given dose years after diagnosis.

iso-effective dose model described in the cited papers (see next Chapter). Authors of these publication demonstrated that the difference between the RBE-weighted dose and the photon iso-effective dose is especially relevant at high values, i.e. in the tumour. For low dose values, such as those absorbed by peripheral healthy organs, the values calculated by the two models are comparable. In this evaluation we thus assume that RBE-weighted dose can be used to estimate the effects due to single-dose photon irradiation.

Such findings suggest that BNCT with the RFQ-based neutron beam is a viable treatment modality from the point of view of radiation-induced cardiovascular disease.

4.5 In-air dosimetry

We here evaluate the dosimetry in the air of the treatment room demonstrating the effect of boron added in the walls⁵. The in-air dosimetry distributions were evaluated for the air of the treatment room, comparing the cases of ordinary and borated concrete walls. The simulations were run with or without the MIRD phantom in position for a treatment. A mesh F4-type tally was used to map the calculated dose in a color-scale plot. In this case, we used a mesh reticulation with units of dimensions $10 \times 15 \times 20 \text{ cm}^3$.

The dose from neutrons can be determined from kerma assuming Charged Particle Equilibrium (CPE) conditions. This refers to the situation in which there is balance between the radiant energy of the incoming and outgoing particles in a given volume. When CPE occurs in an irradiated medium, kerma in the volume is equal to the absorbed dose [85]. We can reasonably assume that this situation is verified in the volumes studied in our simulations.

For neutrons, kerma can be calculated by multiplying the fluence by the kerma factors [86]. A tally of type F4 was thus required, coupled with a table of kerma factors for the fluence conversion. This is possible in MCNP, with proper cards which divide the energy range of the problem in a chosen binning structure (DE card values), and multiplies the neutron fluence in each bin by the kerma factor in the corresponding DF card. The result of the tally provided as the simulation output is the sum over all energy bins, i.e. the total absorbed dose in the volume, if CPE conditions are valid.

To obtain the absorbed dose in air, we have used the neutron kerma factors for Medical Physics Air, calculated from kerma data in ICRU Report 63 [87] and JENDL-3.2 cross sections and Q-values (kerma factors from [88]).

In addition, other dosimetric quantities were calculated as explained in the next paragraphs: we simulated the equivalent dose, H, and the ambient dose equivalent $H^*(10)$. These quantities were still obtained with FMESH:4-type tal-

⁵Of course, only the patient is expected to be inside the room during the treatment. However, this is an important assessment also for radiation protection of staff and operators of the facility: the best scenario concerning dosimetric quantities outside the treatment room is not independent of the situation inside.

lies, but by varying the DF factors from the factors used for the conversion from fluence to kerma.

4.5.1 Equivalent dose

As mentioned above, for the same absorbed dose, different types of radiation produce different effects in biological tissues. To take into account this, International Committee for Radiological Units (ICRU) and International Commission on Radiological Protection (ICRP) introduced the *Radiation Weighting Factors* (previously *Quality Factors*). They are dimensionless factors related to the LET of a radiation of a certain type and energy, accounting for its effectiveness in inducing biological effect by interacting with human body.

Equivalent dose, H , is a “protection” quantity⁶ used in radiation protection, that takes into account the biological effectiveness of the radiation. For each body tissue or organ T , equivalent dose H is calculated from the mean absorbed dose D multiplied by the radiation weighting factor w_R which depends on the type and energy of the radiation R :

$$H_T = \sum_R w_R \cdot D_{T,R} \quad (4.5)$$

We used the factors of ICRP Publication 116 [89] for neutrons, given as a continuous function of neutron energy E_n as follows:

$$w_R = \begin{cases} 2.5 + 18.2e^{-[\log(E_n)]^2/6} & \text{for } E_n < 1 \text{ MeV,} \\ 5.0 + 17.0e^{-[\log(2E_n)]^2/6} & \text{for } 1 \text{ MeV} \leq E_n \leq 50 \text{ MeV,} \\ 2.5 + 3.25e^{-[\log(0.04E_n)]^2/6} & \text{for } E_n > 50 \text{ MeV.} \end{cases} \quad (4.6)$$

To obtain the equivalent dose, a FMESH:4 tally has been used with DF values obtained from the air kerma factors described in the previous paragraph, this time multiplied by the appropriate w_R .

4.5.2 Ambient dose equivalent

Even with the same equivalent dose absorbed in each part of the human body, the response of different tissues is different, due to the fact that some tissues are more sensitive to radiation than others. The protection quantity E , *effective dose*, takes into account this effect through the *Tissue Weighing Factors* w_T , which depend on the tissue radiosensitivity. The Effective Dose Equivalent is calculated summing the dose equivalent values in an organ/tissue, multiplied by the associated w_T , for each organ or tissue irradiated:

$$E = \sum_T w_T \cdot H_T = \sum_T w_T \cdot \left(\sum_R w_R \cdot D_{T,R} \right) \quad (4.7)$$

⁶Not a physical quantity: its definition can change over time, depending on the decisions of the Commissions for Radiation Protection which establish the factors used to define it.

The protection quantity *Effective Dose Equivalent* is defined by ICRP as the central radiation protection quantity, however it is not measurable.

The operational quantities were introduced by ICRU [90] to enable the assessment of protection quantities for external irradiation. They are intended to provide a reasonable estimate of the protection quantities relevant for human exposure to external radiation under typical irradiation conditions.

For all types of external radiation, the definition of operational quantities for area monitoring relies originally on the dose equivalent value at a certain depth d in a simple phantom, the ICRU sphere [91], a 30 cm diameter sphere of tissue-equivalent material with density 1 g/cm^3 , and mass composition: 76.2% oxygen, 11.1% carbon, 10.1% hydrogen, 2.6% nitrogen.

Ambient dose equivalent, $H^*(d)$, is the main operational quantity used in radiation protection for external monitoring of environments. With $d=10 \text{ mm}$, $H^*(10)$ is intended to provide an assessment of effective dose in the case of strongly penetrating radiation. According to ICRP publication 103 [92], the ambient dose equivalent $H^*(10)$ at a certain point in a radiation field is the dose equivalent that would be produced by the corresponding expanded and aligned field at a depth of 10 mm in the ICRU sphere, on the radius opposing the direction of the aligned field (Figure 4.5). Expanded radiation field is a hypothetical field where fluence and its angular and energetic distributions have the same values in the volume of interest as in the actual field at the point of reference. An expanded and aligned radiation field requires additionally a unidirectional fluence [93].

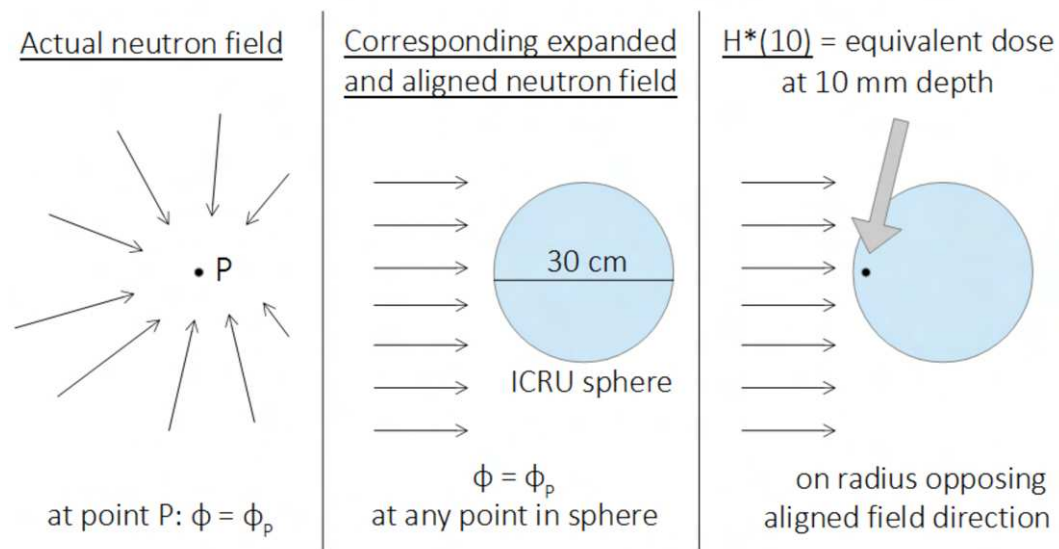


Figure 4.5: Expanded and aligned field and $H^*(10)$ representation

MCNP6 provides a dedicate feature for the direct calculation of $H^*(10)$ in a region of interest, however, in the available version of the code, it is incompatible with the use of mesh tallies. Thus, to obtain the ambient dose equivalent we used

4.5. In-air dosimetry

a FMESH:4 tally coupled with suitable DE+DF factors (see subsection 4.5) for the conversion of fluence in $H^*(10)$ [94]. All the dosimetric quantities of interest were evaluated for three neutron energy bins: thermal (0-0.4 eV), epithermal (0.4 eV-0.5 MeV) and fast (0.5-4 MeV). Figure 4.6 shows the total distributions, i.e. the dose values for the whole energy range from 0 to 4 MeV, for ordinary and borated concrete.

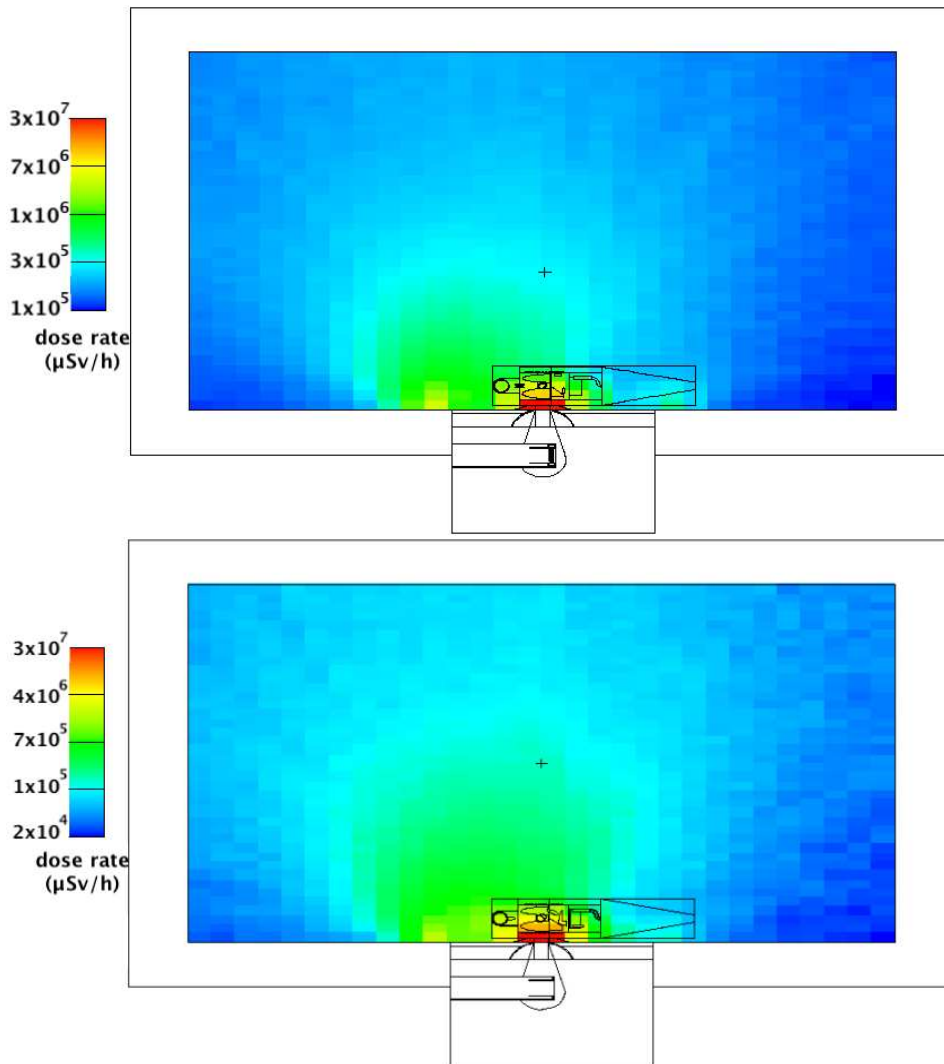


Figure 4.6: In-air distribution of the rate of ambient dose equivalent in the treatment room, simulated with MCNP6, which evidences the influence of boron in the wall concrete.

The distributions of doses with walls of borated concrete show a reduction⁷ compared to the ones obtained with ordinary concrete, confirming the effective-

⁷It should be noted that the color scale is not the same in the different plots.

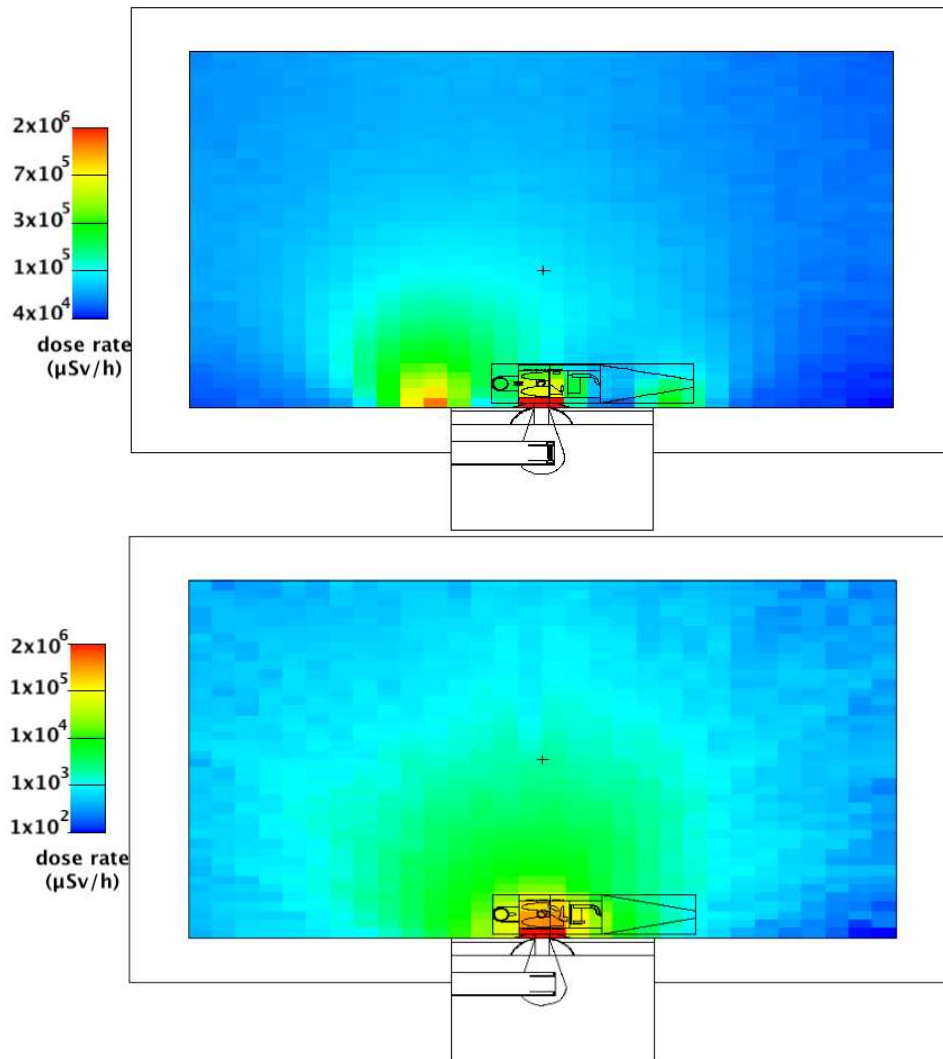


Figure 4.7: In-air distribution of the rate of ambient dose equivalent in the treatment room, simulated with MCNP6, for the thermal component only

ness of boron addition in the walls in reducing the neutron flux in the air. The action of boron in concrete is even more evident when considering the in-air dosimetry distributions related to the thermal component only (Figure 4.7).

From the obtained in-air distributions, it is also possible to notice a higher dose along the wall on the left side of the beam. Such asymmetry is due to the vacuum channel of the accelerator structure. To eliminate this effect, it may be worth adding a layer of neutron-absorbing material to the wall in front of the vacuum tube.

4.5.3 Dose from neutron activation

In order to comprehensively assess the dosimetry in the treatment room, it is necessary to consider also the dose coming from the neutron activation of the irradiated materials. This is an important effect as it may require additional shielding or a beam-shutter to improve the patient safety.

To study this issue, we first carried out FLUKA simulations evaluating the dose resulting from the total induced radioactivity. As explained above, the use of FLUKA required the approximation of the source, still conservative concerning the reaction rates of neutron activation.

Figure 4.8 shows the FLUKA distribution of the rate of ambient dose equivalent due to overall induced radioactivity, 5 minutes after a 2-hours clinical irradiation, in a treatment room with walls of ordinary concrete and borated concrete, respectively. The reduction of the residual dose in the case of borated concrete walls demonstrates the effectiveness of this material in reducing the neutron activation in the room. However, the results suggest the need for additional shielding in the patient area. To this end, the distribution of radioactivity in the room should be employed as a source to calculate the dosimetry adding a screen in front of the beam port to evaluate the advantages of such solution. However, in FLUKA, the original geometry can no longer be modified, except by setting a previous material to vacuum or air (“MAT(decay)” option). This can be useful to visualize the spatial distribution of the dose around an activated element without the effect of the surrounding materials present in the original geometry, but it prevents the insertion of new materials. This is instead achievable using PHITS [67] along with the DCHAIN activation code (“DCHAIN-PHITS”) that has been recently incorporated in it. PHITS can only calculate the induced radioactivity immediately after irradiation, DCHAIN calculates the time evolution of induced radioactivity and the heat and gamma spectrum due to the decay [95].

The combination of PHITS and DCHAIN was exploited to design a possible shield to reduce the dose from the residual radioactivity in the patient area, as illustrated in the next paragraph.

4.5.4 Shielding design for residual dose

A model of the treatment room was created with PHITS and a simulation of a 2-hour clinical irradiation was run with the “T-DCHAIN” section enabled. This section activates the radionuclides production in the region of interest and allows to set the desired decay times. The generated output was used as the input for a DCHAIN simulation, which calculated the induced activity, the decay heat⁸ and the emitted gamma spectrum, during and after irradiation.

A set of simulations allowed to calculate the dose in the patient area due to the radioactivity induced in the BSA. The decrease of the dose caused by a shielding at the beam-port was achieved by running a new PHITS simulation in which the original source was replaced with the decay gamma spectrum generated by

⁸The heat released as a result of radioactive decay.

running DCHAIN. In this new PHITS simulation the geometry can be modified, adding different shielding geometries.

Figure 4.9 shows the distribution of the rate of ambient dose equivalent, at the end of the treatment, given by the radioactivity induced by neutron irradiation of the BSA. In Figure 4.10 the distribution of the same quantity in presence of a shielding located on the wall of the BSA and a shutter at the beam-port, both made up of a 5 cm thick Pb screen. This screen should shield the gamma radiation coming from the activated materials in the BSA, to protect the patient and the medical staff during the preparation and in the operations at the end of the irradiation session. The comparison⁹ between Figure 4.9 and 4.10 shows a dose reduction of at least one order of magnitude in the patient positioning area.

Finally, the dose distribution due to the neutron activation of the shielding on the BSA wall was also individually simulated. Figure 4.11 shows the distribution of the rate of the ambient dose equivalent, at the end of a 2h treatment, given by the radioactivity induced in such shielding. The dose due to the shielding activation proved to be negligible, especially when compared to the advantage gained in terms of ambient dosimetry after irradiation.

⁹Also in this case, to be noted that the color scale is not the same in the two plots

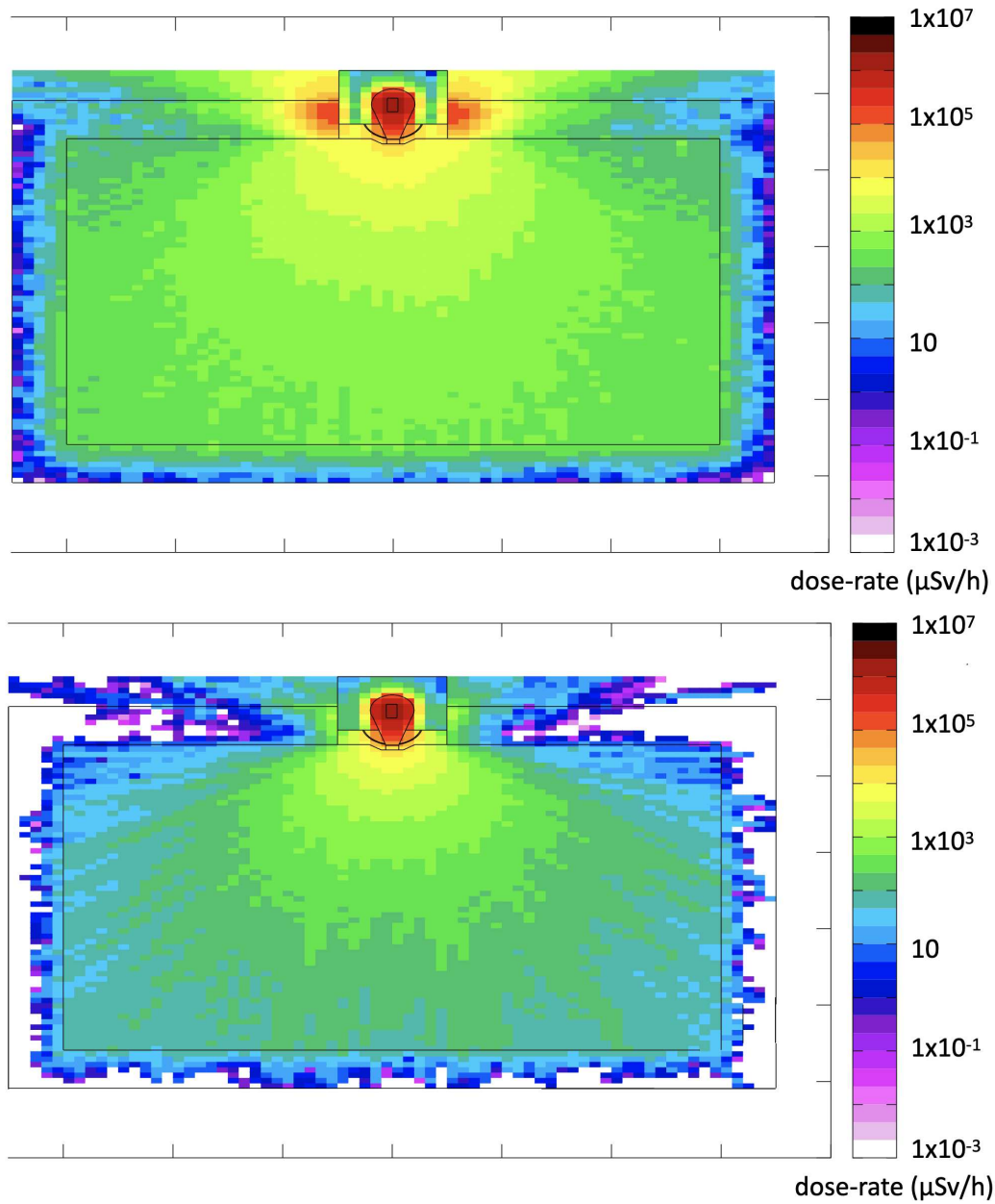


Figure 4.8: Distribution of the rate of ambient dose equivalent from the overall induced radioactivity, 5 minutes after a 2-hour clinical irradiation, in a treatment room with walls of ordinary concrete (top) and borated concrete (bottom)

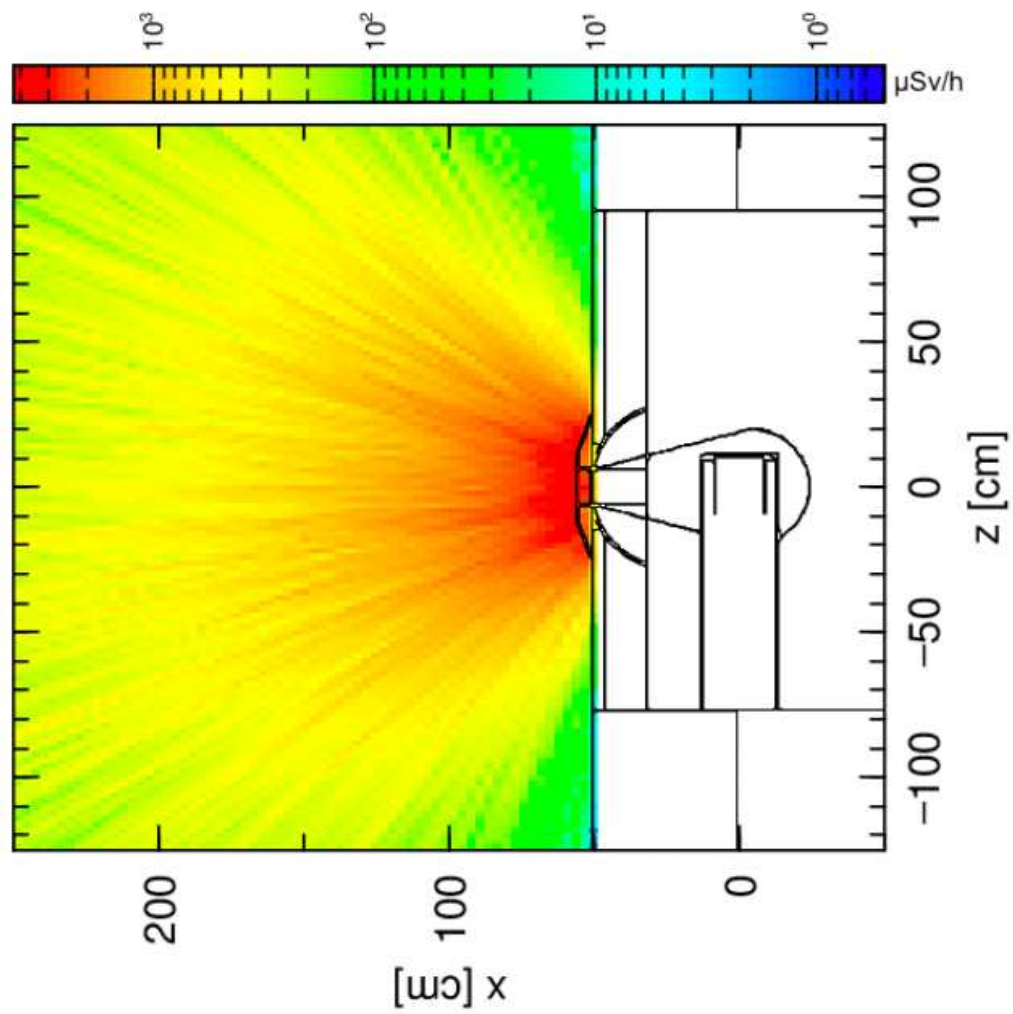


Figure 4.9: Distribution of the rate of ambient dose equivalent, at the end of the treatment, given by the radioactivity induced by neutron irradiation of the BSA

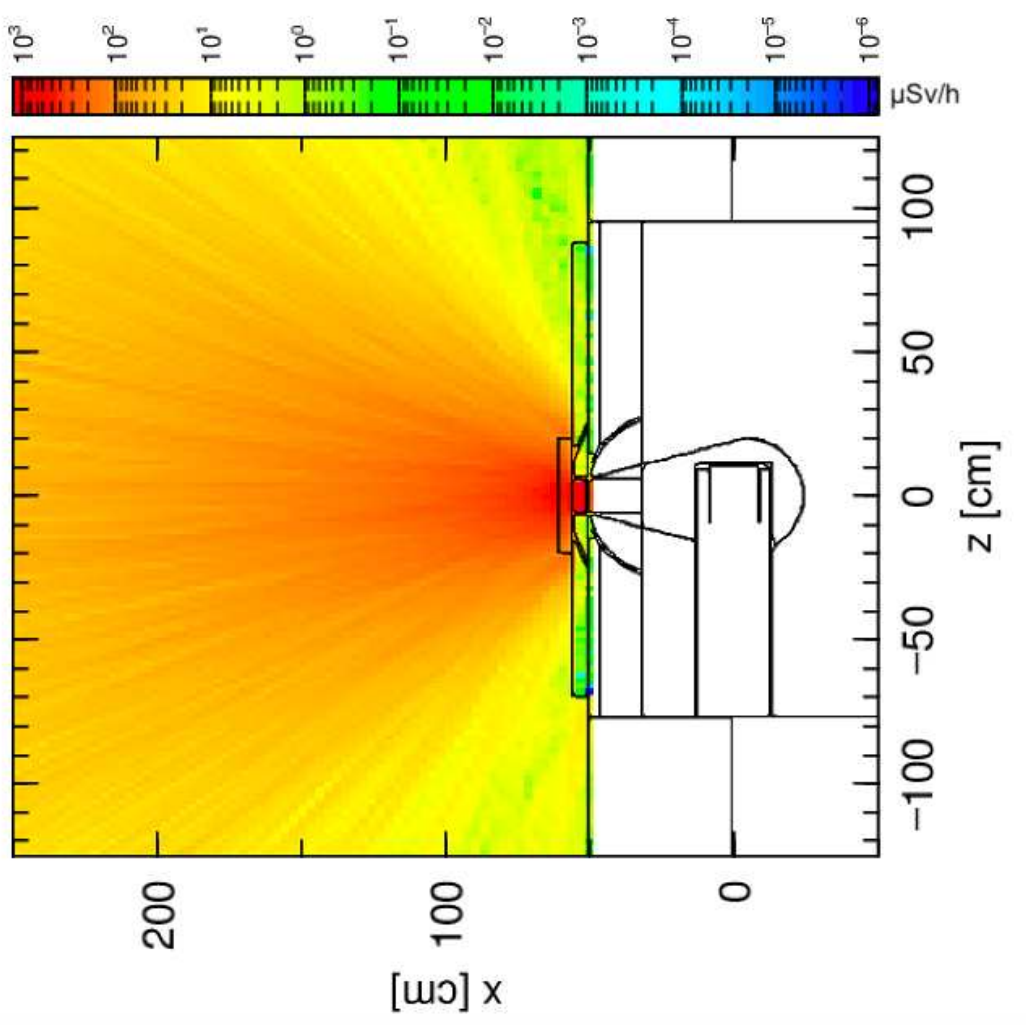


Figure 4.10: Distribution of the rate of ambient dose equivalent, at the end of a 2h treatment, given by the radioactivity induced by neutron irradiation of the BSA, in presence of the proposed lead shielding on the BSA walls

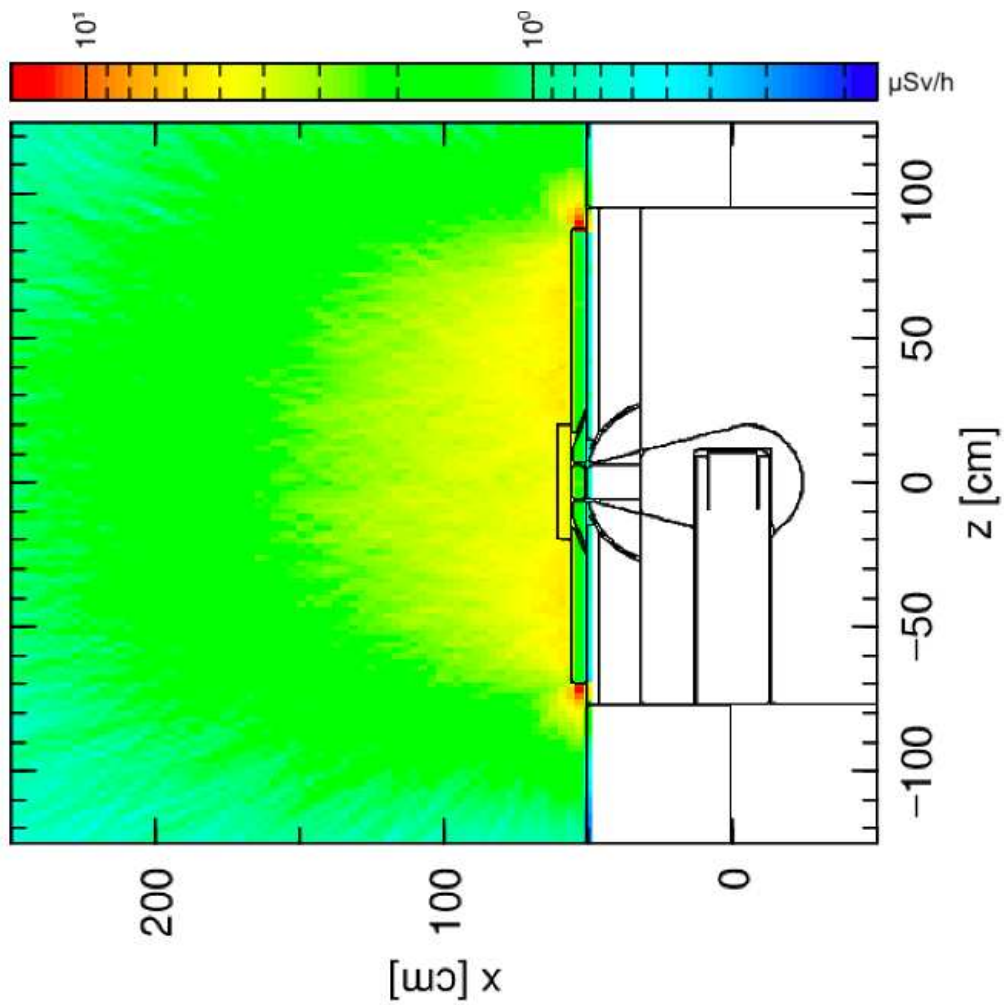


Figure 4.11: Distribution of the rate of ambient dose equivalent, at the end of a 2h treatment, given by the radioactivity induced by neutron irradiation of the proposed lead shielding on the BSA walls

Clinical applications

The last part of the work is dedicated to the simulation of clinical applications of an AB-BNCT facility based on the INFN-RFQ coupled to Be target and BSA with *Alliflu* core, with an original approach. The study is characterized by innovative aspects such as the combination of two different particle therapy techniques and the use of a new model, recently developed in Argentina, to express the BNCT dose in photon-equivalent units. Moreover, a new computational tool, implemented in Pavia in the framework of the INFN project IT_STARTS (*an Innovative Toolkit to Simulate neuTron cApture theRapy irradiation and doSimetry*) was employed to analyze the results of the treatment planning.

This Chapter describes the comparison of the in-patient dosimetry due to a BNCT treatment with the dose delivered in a clinical case irradiated with 12-C ions. The tools and methods to perform such comparison also led to explore the possibility to combine BNCT and 12-C ion-therapy to obtain a favourable clinical result, in terms of tumour control and sparing of the healthy tissues. The combination BNCT-hadrontherapy has never been explored before: the rationale of this study is the possibility to exploit the advantages of the two strategies to tackle very challenging tumours, as illustrated later in this Chapter. Before, the next section summarizes the principle of hadrontherapy and the advantages of heavy ions therapy.

5.1 Hadrontherapy with carbon ions

Hadrontherapy (or particle therapy) is a form of radiotherapy that uses beams of protons, neutrons or heavier charged ions [97]. These beams have physical and radiobiological characteristics considerably different from those of photons or electrons used in traditional radiotherapy.

From a physical point of view, the advantage of radiotherapy with hadrons relies on their dose-depth profile. In this regard, a fundamental quantity connected to the absorbed dose is the Linear Energy Transfer (LET), defined as the average

amount of energy transferred to matter per unit of traveled distance from ionising radiation exclusively via electronic collisions.

When the primary mechanism of energy loss is through inelastic collisions with the electrons of the traversed material, as happens in particle therapy, the LET is equal to the stopping power. The stopping power, which is the mean energy loss per unit of path length, depends on the properties of the incident particles and of the target material, and for the particles used in hadrontherapy it is well described by the Bethe-Bloch formula [98]:

$$-\left\langle \frac{dE}{dx} \right\rangle = K \rho z^2 \frac{Z}{A} \frac{1}{\beta^2} \left[\frac{1}{2} \log \left(\frac{2m_e c^2 \gamma^2 \beta^2 T_{max}}{I^2} \right) - \beta^2 - \frac{\delta}{2} - \frac{C}{Z} \right] \quad (5.1)$$

where $K = 4\pi N_A r_e^2 m_e c^2$ (with N_A the Avogadro's number, r_e the classical electron radius, m_e its mass, c the velocity of light), z is the charge of the incident particle in units of the elementary charge e , ρ the density of the target material, Z and A respectively its atomic and mass numbers, $\beta = v/c$ the ratio of the projectile velocity in the medium over the speed of light, $\gamma = \sqrt{1 - \beta^2}$, T_{max} the maximum energy transfer in a single collision, I the mean excitation energy of the target material, δ and C the density and shell corrections.

The stopping power is dominated by the $1/\beta^2$ term, indicating that the energy loss is inversely proportional to the squared speed of the projectile particle. At the entrance in the medium, with the particle having high speed, the release of energy is small; as the speed decreases, the average transferred energy increases, up to a maximum reached just before the stopping of the particle.

The resulting dose-depth profile is dominated by a pronounced peak in correspondence of the final path of the particle (Figure 5.1). It is the so-called Bragg Peak, characteristic of charged particles and the reason behind the higher precision of hadrontherapy compared to traditional radiotherapy: the particles used in hadrontherapy release almost all their energy in the region of the Bragg peak, in a spot of limited dimensions.

By modulating the energy of the incident particle, a precise correspondence between the Bragg peak and the tumour can be achieved, leading to the maximum of dose delivered in the volume to treat. In clinical practice, the superposition of beams of different initial energy is used, to generate a dose profile able to cover the entire target depth: the Spread Out Bragg Peak (SOBP) represented in Figure 5.2.

With the possibility to deliver the dose to the tumour with high precision while reducing the adverse effects in the surrounding tissues, hadrontherapy can offer an enhanced tumour control and better outcomes than conventional radiotherapy for a variety of cancer.

In addition to the physical characteristics described above, hadrontherapy with carbon ions also offers a radiobiological advantage. Projectiles with higher mass than protons such as ^{12}C ions produce in fact denser ionization tracks, leading to a reduced cellular repair and thus to a higher biological effectiveness [99]. This is why ^{12}C ion therapy is especially interesting for the treatment of radio-

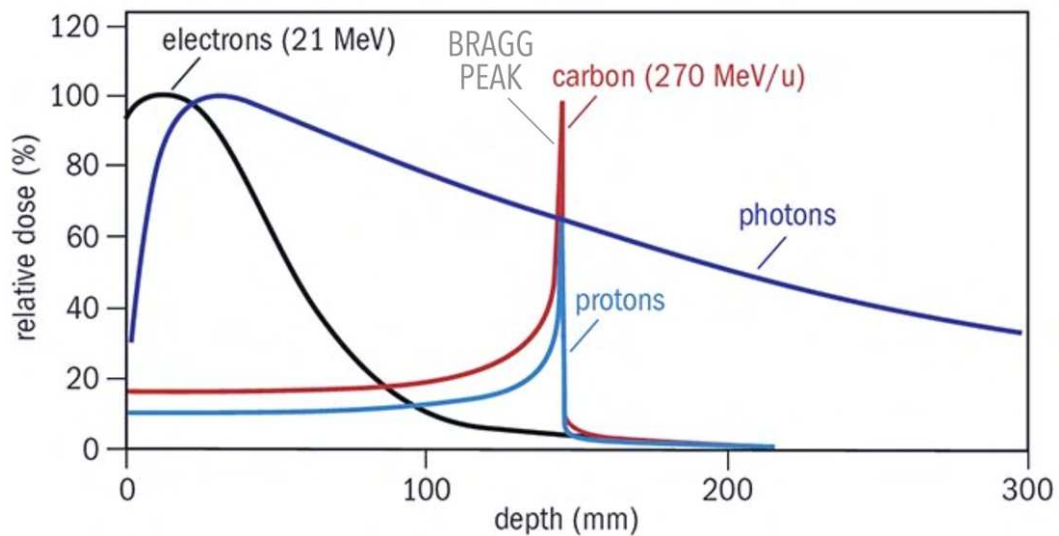


Figure 5.1: Dose-depth profile of different radiations and Bragg peak

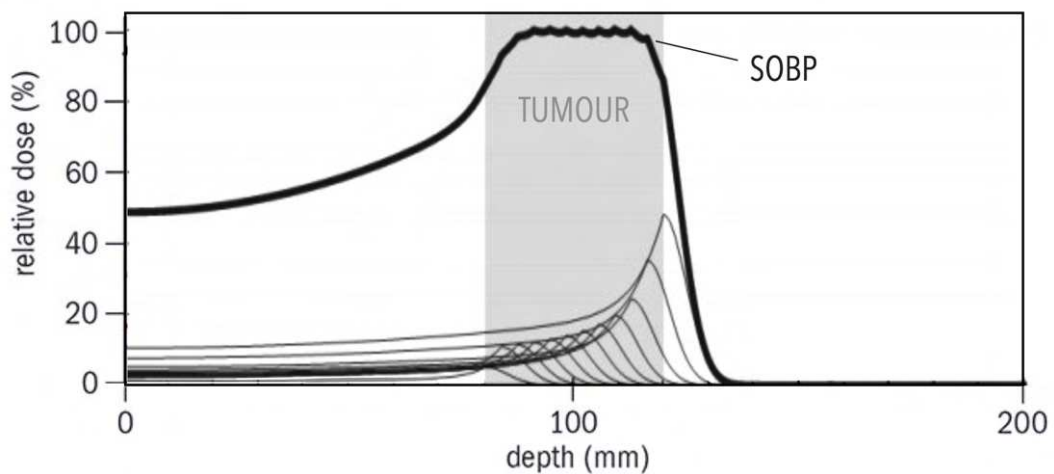


Figure 5.2: Example of SOBP (Spread Out Bragg Peak) built in correspondence of the shaded region representing the zone to treat

resistant tumours, for which a highly effective radiation is preferable, localized in proximity of organs at risk that can be spared thanks to the ballistic precision of the Bragg peak.

However, due to the complexity of the machines required to accelerate ions to the energies needed for the treatment, currently the application of ^{12}C is restricted to a few facilities in the world. One of them is the National Center of Hadrontherapy (CNAO) located in Pavia, which treated the first patient with ^{12}C ions in 2012.

The idea to exploit ^{12}C ion therapy as a boost of BNCT of large tumours was born in the context of the project NEU_BEAT, a High Relevance Project funded by MAECI¹ in the frame of Italy-China technological and scientific cooperation 2016-2018. It is being further deepened in the Project *Progetto Dipartimento di Eccellenza* of the Physics Department, University of Pavia (2018-2022).

5.2 Comparison and combination of BNCT and ^{12}C treatments

Combining the two radiation therapies could be advantageous in different situations. The selectivity of BNCT in targeting tumour cells and the high precision of hadrontherapy with carbon ions could be exploited for tumours that cannot be controlled by hadrontherapy alone. In fact, when the tumour volume is large, and the Planned Treatment Volume comprises very radiosensitive targets such as the optic nerve, the dose delivered by ^{12}C must be limited to avoid relevant adverse effects. In these cases, BNCT could be used to irradiate large portions of tissues/organs, because the delivery of high doses is selectively determined by boron distribution. However, large tumours are often poorly vascularized in their core, possibly preventing a suitable and uniform boron distribution in the bulk. Moreover, penetration of neutron beams may not be optimal in the deepest part of the malignancy. Carbon ions can instead deposit a very effective dose in the tumour core, ensuring a uniform tumour painting, where BNCT may be less effective. In other words, BNCT could represent a valuable tool to treat the infiltration and the peripheral part of the tumour: here isolated and proliferating cancer cells could be killed with BNCT while avoiding a higher-than-safe dose to healthy tissues. The addition of a ^{12}C boost would ensure a therapeutic dose to the inner part of those tumours, where BNCT dose is also more difficult to calculate due to lack of precise knowledge of boron distribution.

To explore this approach, we studied a representative clinical case of head and neck cancer, that is a target for carbon ion therapy in clinical practice [100] and also one of the diseases in which BNCT has given the most promising clinical results. In Helsinki, Finland, 69 patients received BNCT at the VTT reactor between 2003 and 2012, the 2-year locoregional progression-free survival rate was 38% and the overall survival rate 21% [101]. In Japan, patients with either locoregional recurrence or newly diagnosed head and neck cancer were treated at KURRI (Kyoto) between 2001 and 2007, resulting in overall response rate of 58% within 6 months and median survival time of 10.1 months after treatment [102]. In Taiwan, 17 patients with 23 recurrent head and neck were treated with with a 2-year OS of 47%. A second trial was performed combining BNCT and Intensity Modulated Radiotherapy [103]. Recently, the results of a phase II trial using the C-Bens accelerator in Japan have been reported. Accelerator-BNCT produced tumor response in 71% of head and neck patients, with no serious adverse events [104].

¹Ministero degli Affari Esteri e della Cooperazione Internazionale

In this study, we used the data from a patient treated with carbon ion therapy at the CNAO of Pavia. The patient was irradiated with a fractionated irradiation scheme. The primary tumour resulted in complete control. Several months later it recurred in a zone irradiated with lower dose, due to the presence of the optic nerve in the peripheral part of the PTV, the Planning Target Volume (see below).

Three are the main volumes defined in radiotherapy planning [105]:

- GTV (Gross Tumour Volume): essentially the gross demonstrable location and macroscopic extent of the tumour, defined by physical examination and/or imaging studies;
- CTV (Clinical Target Volume): the volume that contains GTV plus a margin for sub-clinical microscopic malignant lesions that cannot be fully imaged;
- PTV (Planning Target Volume): geometric concept designed to ensure the adequate deliver of dose to the CTV, it contains the CTV plus a margin to account for variations in patient position, organ motion, and other treatment uncertainties.

Radiotherapy planning must always take into account also the safety of critical normal tissue structures defined Organs At Risk (OAR). In some cases a margin analogous to the PTV can be necessary around a specific OAR to ensure that it receives a dose below a safe level. This is particularly important when treating with heavy ions, due to their enhanced biological effectiveness with respect to traditional radiotherapy.

In the case under study, the patient was affected by an adenoid cystic carcinoma of the salivary glands (Figure 5.3.a), and received carbon ion therapy in 16 fractions. The irradiation was divided into 9 fractions covering the PTV “Low Dose” (PTV-LD), defined based on the presence of the OAR optic nerve which limits the treatment, and additional 7 fractions covering the PTV “High Dose” (PTV-HD) only.

Months after the treatment, the patient presented a recurrence, localized in the PTV-LD, and very close to the optic nerve (Figure 5.3.b). In this case it would have been impossible to treat the recurrence with carbon ions sparing the optic nerve. In fact, it is impossible to paint the tumour with a heavy ion beam without depositing the same dose to a normal tissue/organ comprised in the treatment volume as depicted in the image.

In Figure 5.4 the three volumes for the case under study are shown: it is evident the large volume of PTV-LD compared to the GTV, which makes radiation treatment considerably challenging. However, it is worth noting that patients who received BNCT in the trials cited above were affected by large tumours. For example, in Finland, the median GTV volume was 105 cm^3 , ranging from 53 to 187 cm^3 [101]. The primary tumour of the chosen clinical case is thus a representative example of possible BNCT candidates. Also the PTV_LD volume is comparable to tumours previously treated [106].

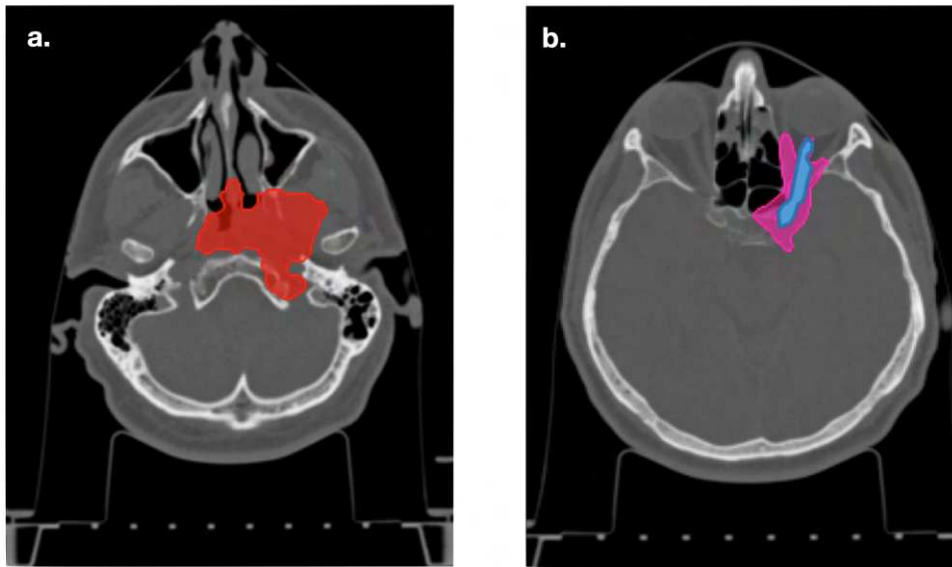


Figure 5.3: CT image of the patient: (a) with the primary tumour (GTV) depicted in red, and (b) with the recurrence in pink and the optic nerve in blue

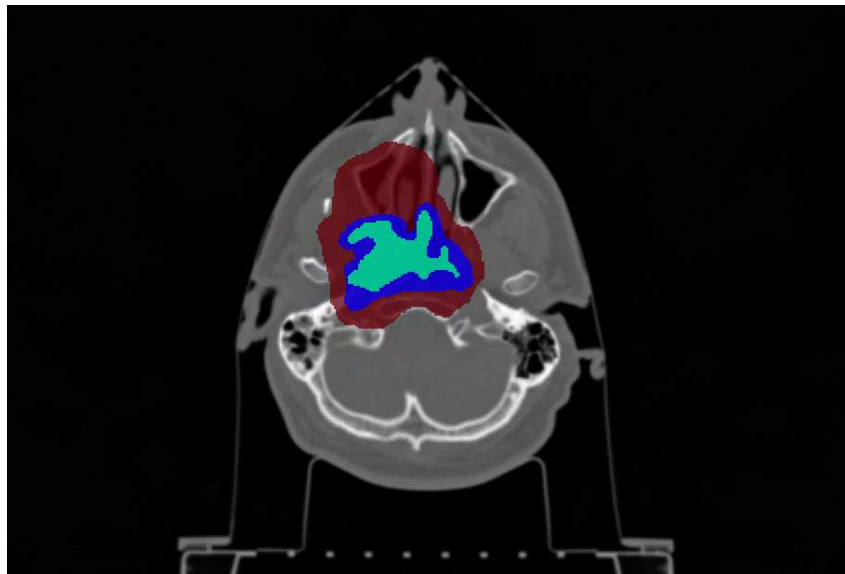


Figure 5.4: CT image of the patient with in red the PTV-LD, in blue the PTV-HD and in green the GTV

The goal of this investigation was first to compare the possible effects of a BNCT treatment, using the RFQ neutron beam, in terms of dose distribution and tumour control probability with those obtained with the real 12-C treatment. Moreover, we wanted to explore the potential of BNCT when 12-C treatment is not possible and in combination with 12-C to obtain a more effective dose distri-

bution.

Three different scenarios have been considered for the proposed analysis involving both dose distributions and TCP calculations:

1. Evaluation of BNCT as a potential treatment for the primary tumour: comparison to the treatment with ^{12}C
2. Evaluation of BNCT as a potential treatment for the recurrence;
3. Evaluation of ^{12}C and BNCT as complementary treatments to produce a more advantageous dose coverage of the PTV. compared to the one achieved in the treated patient.

The comparison and the combination of different types of therapies can only be carried out when the dose values are expressed in consistent units. In fact, BNCT products and ^{12}C have different effectiveness in producing biological effects. It is thus necessary to translate the dose values in a common language, to compare and eventually sum charged particle therapy and BNCT dose values.

The doses delivered in particle therapy are normally expressed in photon-equivalent units or Gray equivalent: GyE or Gy-Eq. GyE is the measured physical dose in Gray multiplied by the RBE factor specific for the beam used. As already introduced, RBE is the ratio of dose producing a certain biological effect with photons and the one required to produce the same effect with the ionizing radiation of interest. For carbon ion therapy the Treatment Planning System already calculates dose in GyE, taking into account different RBE according to the LET of the beams used to form the SOBP.

The BNCT absorbed dose from the simulated treatment planning was converted into photon-equivalent units using the *photon iso-effective dose* model, illustrated in the next paragraph.

5.2.1 Photon iso-effective dose

The dose from a BNCT treatment is due to a mixed field, with different dose components: dose from thermal neutrons, mainly due to ^{14}C and protons through the (n,p) reaction on ^{14}N ; dose from fast neutrons, mainly due to recoil protons from the scattering on hydrogen; dose from the neutron capture reaction on ^{10}B due to α and lithium-7 ion; dose from photons, due to the radiative capture on hydrogen as well as to the gamma background present in the neutron field.

In the traditional approach, the “weighted” or “biological” dose is calculated as follows:

$$D_w = D_t w_t + D_f w_f + D_B w_B + D_\gamma \quad (5.2)$$

with the subscript $i = t, f, B, \gamma$ referring to respectively the dose from thermal neutrons, fast neutrons, (n, α) on boron-10 and gammas. Each dose component is weighted by an appropriate factor w_i accounting for the different effectiveness of the particles delivering the dose with respect to photons, being the weighting

factor for gamma component equal to 1. w_t and w_f are the RBE for neutron interaction, w_B is called CBE (Compound Biological Effectiveness), and takes into account that different boron carriers determine different biological effectiveness of this dose component.

The weighting factors are calculated for a fixed endpoint [109], and this simplification does not lead to a representative photon-equivalent dose. It was in fact demonstrated in [83] that the biological weighted dose is not able to explain the outcomes of BNCT treatments compared to traditional radiotherapy. In the same work, the *photon iso-effective dose* model has been proposed as a more accurate formalism accounting for the biological effect in BNCT.

The photon iso-effective dose is the dose of reference photon radiation which causes the same effect as the combination of the four dose components of the BNCT mixed-field. To calculate the photon iso-effective dose, a first approach is to use the survival of cells as a function of the dose obtained in radiobiological *in vitro* experiments as described in [83]. If *in vivo* data are available, the effect used to compare BNCT and the reference radiation can be a relevant radiobiological figure of merit, such as TCP (Tumour Control Probability), when considering the effect on the malignancy, or NTCP (Normal Tissue Complication Probability) for what concerns the effect on healthy structures [84].

When using cell survival curves, the photon iso-effective dose is calculated from:

$$\sum_{i=1}^4 \alpha_i D_i + \sum_{i=1}^4 \sum_{j=1}^4 G_{ij}(\theta) \sqrt{\beta_i \beta_j} D_i D_j = \alpha_R D_R + G(\theta') \beta_R D_R^2 \quad (5.3)$$

with D_i ($i = t, f, B, \gamma$) indicating the dose components of the BNCT mixed field. The Modified Linear Quadratic model, according to which the biological effect E has a linear-quadratic dependence on dose as $E = \alpha D + \beta D^2$, is used to fit the dose-survival curves and the calculated parameters enter in the equation above. The model also considers the synergism between the different dose components as well as the repair mechanisms as a function of time with the generalized Lea-Catcheside time factor $G(\theta)$ [110].

This model has proven to be robust to explain the outcome of BNCT treatments on head and neck, brain tumours and nodular melanoma carried out in the past. The BNCT photon isoe-effective dose can be thus considered comparable with the 12-C dosimetry in the analysed clinical case.

5.2.2 The IT_STARTS toolkit

For the calculation of the iso-effective dose and the analysis of the results, we worked in the framework of the research project IT_STARTS, aimed to develop a modern toolkit for dosimetry as an open-access program based on the Python™ language [111]. IT_STARTS is a young-researchers grant, funded by the INFN National Scientific Committee 5, and carried out in close collaboration with the Argentinean Treatment Planning and Computational Dosimetry group of CNEA

(Comisión Nacional de Energía Atómica), Buenos Aires, where the formalism of photon iso-effective dose was developed.

With the IT_STARTS toolkit it is possible to use the medical images of the patient anatomy, to convert the dose using different models and to superimpose the isodose curves on the patient geometry. Moreover, it allows to build the Dose Volume Histograms (DVH) for a certain Region of Interest (ROI) and to calculate several relevant quantities, both dosimetric and radiobiological, such as TCP and NTCP.

The treatment planning simulation (i.e. deciding the number, position and orientation of the beams, and constructing of the input for the simulation of the neutron/photon transport in tissues) was carried out with the NCTPlan software ([112], [113]). The outcome of the BNCT treatment was then analyzed with the Python™ software included in the IT_STARTS toolkit as explained below. Within the established collaboration with the Argentinean group, the results were also compared with those obtained with their code BNCT-Ar for appropriate validation [114].

5.3 Treatment Planning, Dosimetry and TCP calculation criteria

The treatment was simulated using the protocol adopted by the Finnish group, who safely applied BNCT to several head and neck patients at the FiR-1 reactor-based facility [116]. Such BNCT protocol consists in two applications, using two beams each. The median time between the 2 treatments was approximately 6 weeks. Boron concentration was also taken from the Finland clinical experience in head and neck cancer, with administration of 350 mg of BPA per kg of body weight, two hours before the irradiation. Table 5.1 lists the boron concentration values assumed in different tissues.

Table 5.1: Concentration values of ^{10}B assumed in tissues for dose calculation

Tissue	^{10}B concentration
brain	15 ppm
optic nerve	15 ppm
eye	15 ppm
skin	22.5 ppm
mucosa	30 ppm
tumour	52.5 ppm

For iso-effective dose calculation in case of head and neck cancer, *in vivo* data have been published, describing a preclinical radiobiological study in an animal

model (hamster) with oral cancer, irradiated with X-rays, with neutrons and with neutrons after boron administration. The animal model was optimized to be representative for the study of toxicity in tumour and in normal tissues [117]. A TCP model was obtained and used in the determination of iso-effective dose: this is the dose due to the combination of the four BNCT radiation components leading to the same TCP as the reference radiation [84].

The photon iso-effective doses for brain and optic nerve were derived from [118], which uses the radiobiological data published in [119] on the myelopathy effects on the spinal cord of rats (end point 50% incidence) irradiated with a mixed neutron-photon beam.

In BNCT treatment planning, the prescription is to the maximum dose that can be delivered to the most radiosensitive organ or tissue involved in the irradiation. After irradiation simulation, having the distribution of dose rates in the volumes of interest, treatment time is determined by the most restrictive dose-limiting value. In head-and-neck treatments, the tissue at risk is mucosa, which absorbs twice the concentration of boron than other normal tissues. The adverse effect limiting the treatment is the oral mucositis grade 3 or higher caused by the depletion of mucosa cells [120]. The dose delivered to the clinical case was prescribed with a very conservative criterion. As mucosa is difficult to contour in the medical images, we considered as mucosa all the normal tissues outside the masks delimiting the organs. Even if the point of maximum dose was not actually in the mucosa, this criterion ensures that mucosa would always receive a dose lower than its tolerance. Following the Finnish protocol, the treatment was limited to deliver a maximum absorbed dose of 6 Gy in mucosa. The maximum dose delivered to eyes, optic nerve and skin and the mean dose delivered to the brain was also calculated and compared to the limiting values [121] proving that the criterion adopted to protect mucosa was indeed the most conservative.

The Finnish protocol foresees a second BNCT treatment after 20 days, assuming that normal tissue is able to fully recover by total repair of radiation damage, while effects sum up in the tumour. This assumption has been proven safe in the clinical trial. For this reason, the dose values due to the two irradiation sessions sum up in the tumour for radiobiological figures of merit calculation.

In photon- and hadrontherapy the dose delivered to the tumour is usually uniform, and the mean absorbed dose is a representative quantity of the dose distribution in the tumour volume. For this reason, the majority of TCP models use the mean dose, without addressing possible effects due to non-homogeneous dose distribution. Instead, BNCT dose is characterized by significant in-depth variations due to the attenuation of the neutron beam in tissues. Moreover, head and neck tumours treated with BNCT are large, ranging from 20 cm³ to 400 cm³ [122, 123, 124]. This can cause differences of about 20% between the maximum and minimum dose. For this reason, a TCP calculated using the mean dose is less significant. González and Carando developed a theory named *equivalent sub-volume model* [125] and this was included in a TCP model to take into account non-homogeneous dose distributions.

Given a uniform absorbed dose D , and a tumour control probability (TCP) defined as:

$$TCP(v, D) = e^{(c_1 v^{c_2} S(D))}, \quad (5.4)$$

where v is the tumour volume in cm^3 , c_1 and c_2 are parameters modulating its effect on the probability of local control, and $S(D)$ the cell survival, the subvolume equivalent model applied to equation 5.4 gives

$$TCP_T = e^{-c_1 v^{c_2} (\int_T S(D(x))^{1/c_2} dx/v)^{c_2}}, \quad (5.5)$$

where $D(x)$ represents the dose in the subvolume centred at the x point.

For the head and neck tumour, the TCP model for non-uniform single-fraction photon doses was constructed based on the rate of complete responses reported by Rwigema et al. [126] for patients bearing recurrent squamous cell carcinoma of the head and neck [127]. The fractionated doses were first converted to single fraction values (BED formalism with the alpha/beta of 10 Gy as suggested in the cited work). The parameters of the model were obtained by non-linear minimization method of Eq. 5.4. The resulting TCP model corresponds to single-fraction uniform photon doses. Then the final expression for non-uniform distributions was obtained by applying the cited subvolume equivalent model.

5.4 First scenario

The first case-study is the comparison of BNCT and 12-C treatment in the primary tumour. The position of the beams was optimized to maximize the dose to PTV while sparing the normal tissues (Figure 5.5).

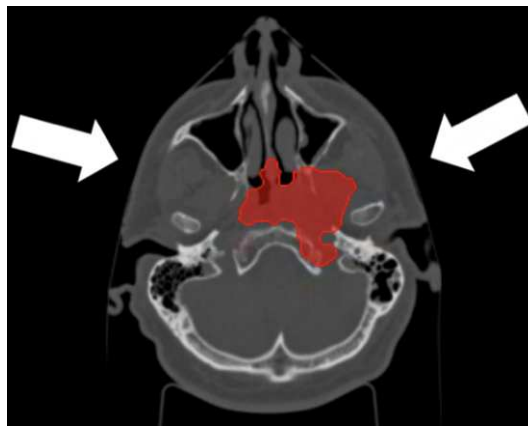


Figure 5.5: CT image of the patient with the primary tumor (GTV) highlighted in red. The white arrows represent the neutron beam-port positions for the two BNCT applications

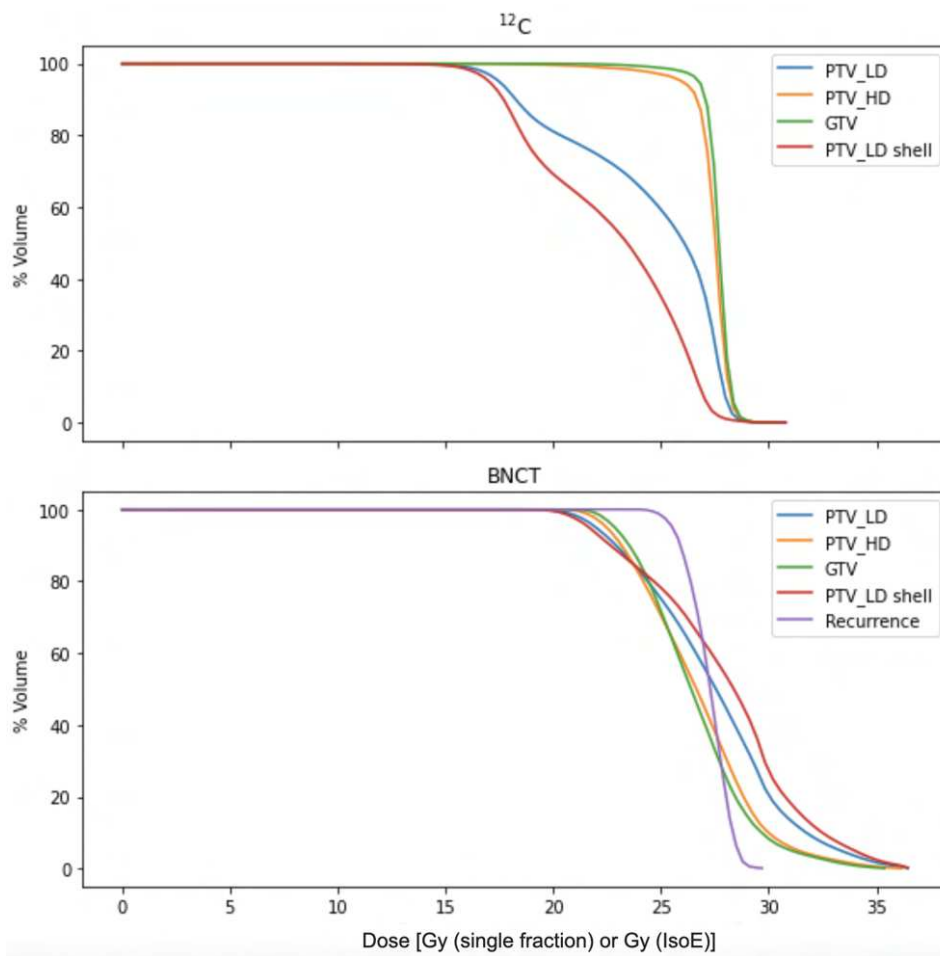


Figure 5.6: Top: Dose Volume Histograms of the carbon ions treatment (in single-fraction). Bottom: Dose Volume Histograms for the BNCT treatment. The units are respectively Gy (IsoE) for BNCT and GyE(single fraction ^{12}C) for carbon ion treatment.

The BNCT iso-effective dose rates were obtained for GTV, low dose PTV and high dose PTV; the same was calculated for relevant healthy tissue/organs. The point in which mucosa received maximum dose was limited to absorb 6 Gy, for a total treatment time of 25.7 min for each of the two sessions. The BNCT Dose-Volume Histogram (DVH) [128] are plotted in Figure 5.6-bottom. In this Figure, and in other references below, PTV-LD represents the entire treatment volume contained in the contour, thus including also PTV-HD and GTV, while the term “PTV-LD shell” indicates the portion of the PTV-LD *without* PTV-HD and GTV, i.e. the real volume treated with a lower dose to protect the optic nerve.

To compare the two treatments, we reported hadrontherapy doses into one fraction by using the BED formalism [80], already mentioned in the previous Chapter. The original carbon ion treatment planning, which consisted in administering 68.8 GyE in 16 fractions, of which 9 to the PTV-LD for a total of 38.7 GyE

5.4. First scenario

and 7 more to the PTV-HD for a total of 38.7+30.1 GyE, was thus converted in single fraction obtaining the values listed in Table 5.2.

	Volume [cm ³]	fractionated doses			single-fraction doses		
		Min [GyE]	Max [GyE]	Mean [GyE]	Min [GyE]	Max [GyE]	Mean [GyE]
PTV-LD	263.5	15.98	83.86	61.34	9.17	31.10	24.48
PTV-HD	102.9	31.57	81.79	70.86	15.07	30.51	27.36
GTV	57.4	43.60	81.79	71.77	18.88	30.51	27.61
PTV-LD shell	160.6	15.98	83.86	55.21	9.17	31.10	22.62

Table 5.2: Dose values for PTV and GTV of the original treatment planning with carbon-ion beam, last columns report the dose values translated into single fraction via BED

Figure 5.6-top reports the DVH for C-12 converted into 1 fraction.

As expected, DVHs of BNCT show a less uniform distribution as C-12, because of difficult beam penetration in large tumours located in-depth. The minimum, mean and max photon iso-effective BNCT doses are reported in Table 5.3. These values were used to compute minimum and mean TCP and compared with the TCP obtained with the single-fraction 12C-ion dosimetry reported in Table 5.2. Table 5.4 lists the TCP of the treatment with carbon ions calculated for each volume of interest with the IT_STARTS toolkit. It is important to stress that, while TCP in the GTV is an indicator of the clinical outcome of the treatment, TCP in the PTV assumes the role of a figure of merit to compare the performance of 12-C and BNCT treatments. In fact, in the PTV, tumour cells potentially spread in the Volume would occupy a volume considerably lower, thus the true value of the TCP would be higher. However, the possibility to summarize in one figure of merit the effect of dose distribution is a useful tool to compare the two radiation treatments.

Table 5.3: Photon iso-effective dose values of the BNCT treatment, with the IT_STARTS toolkit, in the different volumes considered for the first scenario

	Min [Gy (IsoE)]	Max [Gy (IsoE)]	Mean [Gy (IsoE)]
PTV-LD	18.65	36.83	27.46
PTV-HD	20.12	36.52	26.68
GTV	20.82	35.72	26.57
PTV-LD shell	18.65	36.83	27.96

Table 5.4: TCP of the original treatment planning with carbon-ions obtained with the IT_STARTS toolkit for the first scenario

	PTV-LD	PTV-HD	GTV	shell PTV-LD
^{12}C	0.50	0.69	0.77	0.50
BNCT	0.64	0.69	0.71	0.65

5.5 Second scenario

The position of the beams for the treatment planning of the recurrence is shown Figure 5.7. For this simulation, the same parameters and strategies were adopted as before.



Figure 5.7: CT image of the patient with the primary tumor in red and the white arrows representing the neutron beam-port positions for the two BNCT applications

In this case, there is no dosimetry with carbon-ion available for comparison. The point where mucosa received maximum dose absorbed was again limited to absorb 6 Gy, after verifying that the dose to the optic nerve was less limiting, and a total treatment time of 26.9 min.

The minimum, mean and max photon iso-effective BNCT doses are reported in Table 5.5.

Table 5.5: Photon iso-effective dose values of the BNCT treatment, with the IT_STARTS toolkit, in the recurrence

	Min [Gy (IsoE)]	Max [Gy (Iso)]	Mean [Gy (IsoE)]
recurrence	24.00	29.99	27.20

5.5. Second scenario

The BNCT dosimetry for the recurrence is summarized in the DVH plotted in Figure 5.8. The DVH is steeper (i.e. dose distribution is more uniform) with respect to the DVH of the primary tumour (Figure 5.6 bottom) because of the smaller volume of the recurrence compared to the primary tumour.

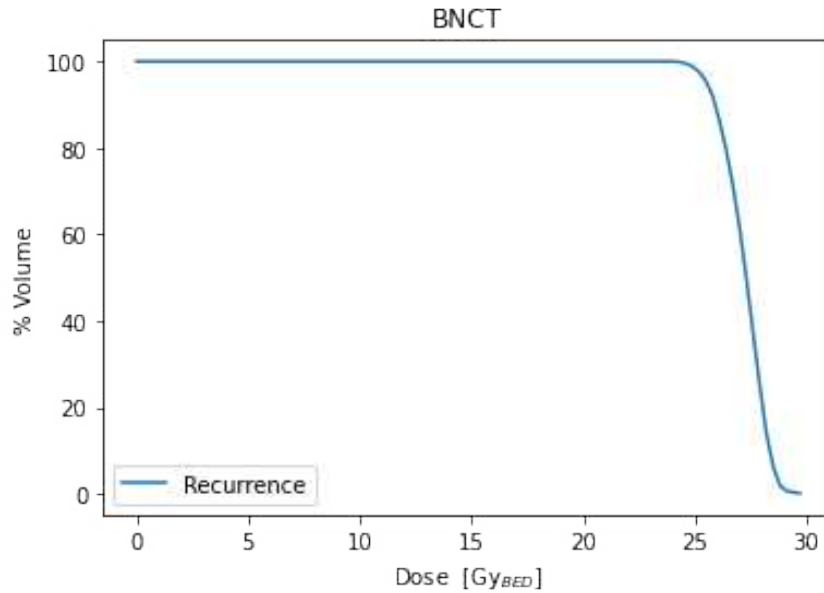


Figure 5.8: Dose Volume Histogram for the BNCT treatment of the recurrence

The dosimetry was used to calculate the TCP with the described method, giving a value of 0.79 (Table 5.6), comparable with the TCP obtained for the treatment of GTV with 12-C ions.

Table 5.6: TCP of the BNCT treatment in the second scenario, obtained with the *IT_STARTS* toolkit.

	recurrence
BNCT	0.79

As the primary tumour was controlled in the volume receiving the highest dose, this result suggests that BNCT could represent a therapeutic option for this recurrence, sparing the optic nerve, which receives a maximum dose lower than tolerance level (15.4 GyE single-fraction). The evaluation of this result must be carefully evaluated in view of the possible BNCT prescription to an organ that already received a 12-C dose, being located in the PTV-LD volume. The optic nerve may become the organ at risk in this recurrence treatment, preventing a so advantageous dose deposition in the tumour. However, the dose prescription is always a medical doctor decision, and depending on the clinical case, a dose higher than tolerance might be prescribed to achieve tumour control.

5.6 Third scenario

This step of the work explores the possibility to conceive combined treatments. At this stage of the work, the calculation of TCP with the superposition of dose distribution is not completed, and these considerations are preliminary evaluations regarding the potential advantage of such approach. In this representative case, 12-C treatment was not sufficient to prevent recurrence because, given its high biological effectiveness, it is not possible to treat large volumes including radiosensitive targets, that cannot be spared from the damages of the Bragg peak. On the other hand, BNCT offers a biological selectivity, depending on the boron biodistribution, which targets especially tumour cells. However, boron uptake is not uniform and depends on many factors including the vascularization of the tumour and the proliferation state. For this reason, boron absorption is likely more effective in isolated proliferating cells than in the most inner parts of the tumour. For this reason, the calculated TCP in the GTV could suffer from high uncertainty due to the lack of information on true boron distribution. This triggered the idea to use BNCT to irradiate a large volume such as the PTV-LD, to act against possible recurrences and to use 12-C ions to paint the GTV with a highly conformal and uniform dose. The TCP value of BNCT treatment in the low dose volume (PTV-LD shell), is 0.65 compared to 0.50 for carbon ions, always considering that these values are an indicator of performance, more than a true tumour control probability. In this treatment, also GTV would receive a dose, however, in a conservative approach it could be not considered at first. Irradiation with 12-C ions only in the PTV-HD ensures a TCP of 0.69, without considering the previous BNCT treatment. Summarizing, the combined treatment would ensure a TCP of at least 0.65 in the critical volume for possible recurrences and at least 0.77 in the bulk tumour volume.

The next step of this work will be the calculation of TCP with the dose distributions overlapped in the same geometry, tuning BNCT treatment time according to the new limitations due to the superposition of dose values in the healthy organs.

This example is of course only one clinical case and other studies are needed to confirm the feasibility and the clinical relevance of such an approach. Nevertheless, the study illustrates for the first time the methods to explore this possibility. Combining the advantages of two types of particle therapy may enlarge the pool of patients accessing therapeutic options when no other strategies are available.

Conclusions and Perspectives

The work described in this thesis has been carried out in the field of AB-BNCT, Accelerator-Based Boron Neutron Capture Therapy. BNCT is a promising radiotherapy, as demonstrated by the clinical trials conducted all over the world, and, with the recent possibility to install clinical facilities based on accelerators, is now at a turning point. Thanks to easier installation and maintenance and less authorisation issues compared to nuclear reactors, accelerators can in fact lead to a wider exploitation of BNCT: potentially, AB-BNCT could become a radiotherapy accessible in many hospitals.

Nowadays, there are many studies devoted to this type of clinical facilities, by different research groups around the world. The projects are based on different kinds of accelerators, targets and Beam Shaping Assemblies (BSA). Contributions to establish innovative evaluation methods, more refined models for dosimetry, new technology for accelerators, targets and moderating materials are being published in view of the next era of BNCT clinical application.

The context of this thesis is a project for a clinical facility based on a RFQ accelerator coupled to a Beryllium target and a BSA allowing an epithermal beam for BNCT of deep-seated tumours. The work aimed to cover different aspects, from the neutron beam spectral tailoring, to the installation of the facility reaching the clinical applications, and was carried out with a multidisciplinary research approach.

The first part was dedicated to the material chosen as the core of the BSA: densified lithiated aluminum fluoride. The material is not commercially available, and has been created on purpose at the Pavia University and INFN local Unit, through an innovative sintering process starting from a proper mix of powders of lithium and aluminum fluoride. The obtained densified material, named *Alliflu*, was studied in detail to verify its suitability as neutron moderator for the BNCT clinical beam. First, *Alliflu* was characterized from the point of view of content of trace elements, water absorption, solubility and microstructure uniformity. Different production procedures were tested to optimize this aspect, after investigation via SEM imaging. The sintering machine and process were optimized as well to

lead to the most reliable and efficient production possible. Moreover, studies regarding the mechanical properties of *Alliflu* were performed, by compression tests before and after neutron irradiation in the nuclear reactor available at the Pavia University.

By means of neutron transmission experiments at the CN accelerator of Legnaro National Laboratories of INFN, the first spectrometry on solid aluminum fluoride was carried out: the simulated moderation properties of the material were validated by comparison with experimental results. Overall, the new material has been characterized in detail and its suitability as neutron moderator has been fully assessed.

Finally, to verify the synergy between *Alliflu* and the other materials that will constitute the clinical BSA, a BSA prototype has been designed for future experiments at CN accelerator. Several configurations were tested through simulations, by varying the geometry and materials to identify the best prototype for optimized measurements at CN. The prototype was built at the mechanical workshop of the INFN Unit of Pavia, and irradiated at CN in September 2021.

A second phase of the work focused on the design of the treatment room, with a view on radiation protection assessment related to the out-of-field dose and neutron activation of the irradiated materials. A model of the treatment room was reproduced with different Monte Carlo codes, and simulations of clinical irradiation were performed to calculate the quantities of interest: the spatial distribution of the dose in the air, the neutron activation of air, walls and patient, and the dose absorbed in the patient organs. All the quantities were evaluated by changing the material of the walls of the room, to identify the best configuration for radiation protection in different representative treatment positions.

Concerning the out-of-field doses in the patient, particular attention was devoted to the doses absorbed in the heart, due to the emerging evidences of radiation-induced cardiovascular diseases. The safety of BNCT from this point of view was assessed according to the most recent studies in this field.

Furthermore, the usefulness of a shielding to decrease the dose in the patient area due to the neutron activation of the BSA was evaluated.

The results indicate that a room with walls made up of borated concrete, with lead shields over the wall of the BSA and in front of the beam-port are suitable characteristics for the RFQ-based irradiation facility. Moreover, the need for a special rest room for the storing of activated urine may be necessary. Finally, out-of-beam dose evaluations allowed demonstrating that BNCT treatment of tumours located in different body districts is low compared to dose-effect assessments present in literature.

The last part of the work explores the clinical applications of the BNCT facility under study. The focus is on the combination of BNCT and hadrontherapy with carbon ions, a possibility never studied before. The work was set up using data from a real treatment with carbon ions at CNAO (*Centro Nazionale di Adroterapia Oncologica*) of Pavia. We analyzed a case of adenoid cystic salivary gland carcinoma that relapsed in correspondence of the optic nerve after the treatment

with ^{12}C ions. Despite the situation was among the most unfavorable for the application of BNCT (very deep and massive tumor), good tumor control probability values were obtained. The study comprised also the possibility to treat with BNCT the recurrence of the tumour, not treatable with charged particles without irreversibly damaging the optic nerve, and the combination of BNCT (to act in the wider PTV including radiosensitive organs) and ^{12}C ions (to boost the treatment in the most inner part of the malignancy).

Although clearly preliminary because focused on only one clinical case, the Tumour Control Probability and the dose distributions suggest that BNCT is comparable to ^{12}C ion treatment concerning the therapeutic potential. Moreover, the combination could help treating difficult peripheral volumes preventing the recurrence of tumours. This study has innovative aspects in its methods: we employed new software tools aimed at integrating a new Treatment Planning System for BNCT, and new models to calculate dose in photon-equivalent units. We worked in close collaboration with the Argentinean Computational Dosimetry group of CNEA (*Comisión Nacional de Energía Atómica*) of Buenos Aires, that developed the Photon Iso-effective Dose model to replace the traditional RBE-weighted dose formalism. This way of calculating dose is more robust and allow a reliable calculation of radiobiological figures of merit, condensing into one value the tri-dimensional dose distribution in tumour and healthy tissue. These figures can be used as a bridge between the optimization of the neutron beam and of the in-patient dosimetry, and the prediction of a clinical output. They are thus a powerful tool for evaluating both the beam quality and the effectiveness of a treatment planning.

Overall, the work described in this thesis represents a contribution to the technological implementation of a pre-clinical and clinical BNCT facility based on the INFN RFQ accelerator. It started with the neutron beam, by developing a new material for the BSA, it approached the design of a suitable treatment room from a radiation protection viewpoint, and concluded by studying an original example of treatment.

The methods and the results presented in this thesis are a clear evidence that BNCT can and must be optimized with respect to past implementations, and that a serious R&D programme is needed to promote a new era of clinical applications, offering a valuable therapeutic option to patients who may have none.

Appendices



TT_Sinter

TT_Sinter is the name given to the sintering machine developed in Pavia in the framework of the namesake project of INFN Technological Transfer. The TT_Sinter project focused on the production of a neutron moderator in solid form made of aluminum fluoride with a small percentage of lithium. The goal was to obtain a compact material with high relative density, good mechanical properties and possibly machinable.

The procedure to create this new material named *Alliflu* is based on a sintering process of a mix of AlF_3 and LiF powders. Sintering of AlF_3 powders is difficult, due to its volatility at high temperatures and to the electronegativity of fluorine, the highest among the elements of the periodic table. For this reason sintering, which requires mass transfer through diffusion, generally involves long high temperature annealing. A more efficient residual porosity removal can be obtained by adding an uniaxial or isostatic pressing. These methods, however, involve the use of large and expensive machines with very long heating and cooling cycles. Field Assisted Sintering / Spark Plasma Sintering (FAST/SPS) has recently become the preferred technique to obtain compact solids from hard to sinter materials [129]. This technique has advantages such as high heating rates (up to $1000^\circ C/min$), very short sintering times (minutes instead of hours) and low sintering temperatures.

Thus, in the framework of TT_Sinter project, an experimental device and an optimized sintering procedure were developed. Powders are densified at high temperature in the presence of uniaxial pressure, and with timing sufficiently short to avoid significant material losses caused by the vaporization of the materials. Compared to common commercialized sintering machines, the proposed set-up is more compact, cost-effective and energy-efficient. The molds are engineered to lead to a uniform temperature distribution in the sample, maximizing the yield and speed of the process, and allowing the production of squared densified samples up to 15 cm per side. Therefore, thanks to the characteristics of the machine and the molds, the proposed method allows to obtain relatively large elements in a short time and with an energy efficient process.

Initially, a prototype of the sintering machine was designed and built at the



Figure A.1: First prototype of the sintering machine designed and created at the INFN Pavia Workshop

Mechanical Workshop of INFN Pavia, in collaboration with the Department of Chemistry of University of Pavia and with SIRAS [130] and TECNEL [131] Pavia Companies. The prototype is the device shown in Figure A.1. It was used to create the first samples of *Alliflu* (Figure 2.3) and part of the moderator bricks used for the measurement campaigns at Legnaro (Figure 3.5).

The final TT_Sinter machine was designed also on the basis of the experience gained by creating samples with the prototype. TT_Sinter is based on the latter but with several improvements: upgrades concerning a greater compactness, a remodeling of the vacuum chamber and the cooling system, the possibility to certify the machine and to explore the market. Compared to the prototype, this machine is also operationally more user-friendly, with a graphical interface that allows both to set the parameters of the machine and to collect and export data. Everything is integrated in a PLC¹ equipped with a touch screen and largely customizable.

Furthermore, the capability and efficiency of the machine were improved: the first with a larger vacuum chamber allowing to produce bigger samples, the second with a more efficient cooling system leading to shorter times required for a process.

Finally, improvements were also made to sensors and safety: various controls

¹Programmable Logic Controller, industrial computers used to control different electromechanical processes in manufacturing or other automation environments.

were integrated, such as interlock etc.

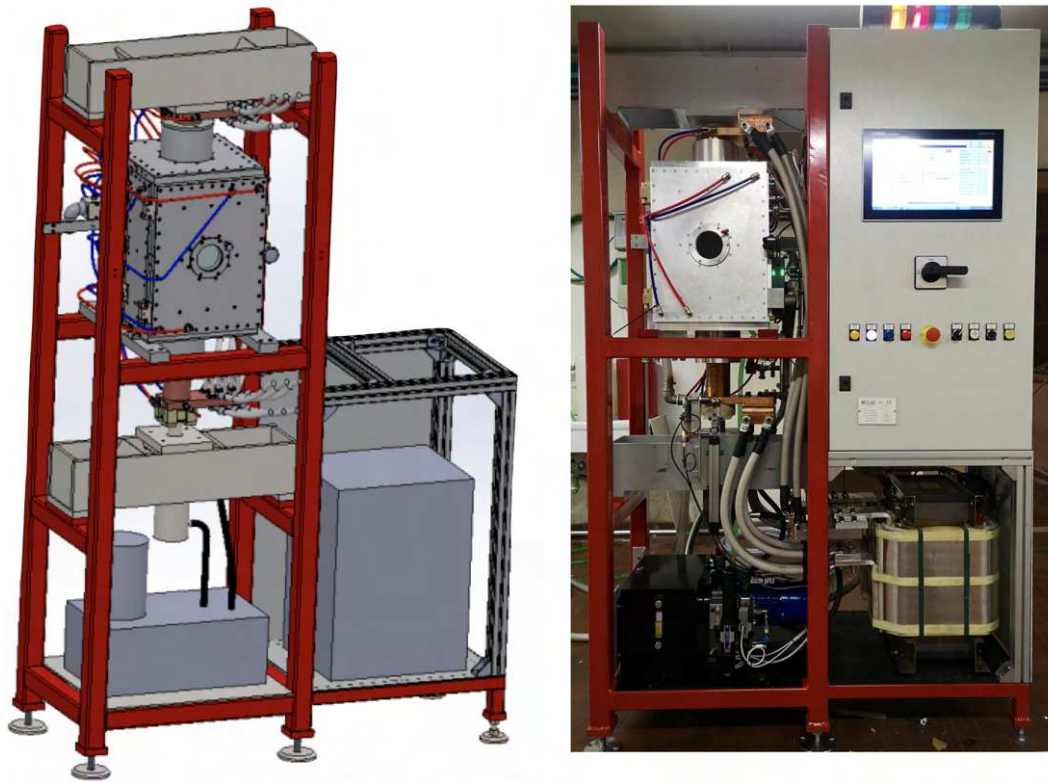


Figure A.2: Project (left) and final realization (right) of the TT_Sinter machine

The project of the new machine “TT_Sinter” is represented in Figure A.2 on the left, while on the right the final device is shown.

A.1 Machine overview

The main characteristics of TT_Sinter machine are: simple layout, smart design of molds, and use of off-the-shelf hydraulic, power components, and controllers. It is composed by a water-cooled vacuum chamber, vacuum system, vertical single-axis hydraulic press, especially designed water-cooled punch electrodes, AC generator, temperature, pressure and other sensors, all controlled by a process PLC. The whole system has size 2.1×1.35×0.85 m (H×W×D). Basically, the machine was designed ensuring very fast process cycle, customizable tooling, easy usage, maintenance and affordability.

The PLC controlling the sintering machine allows to manage several functions and implements all the necessary safety mechanisms. Through the software it is possible to enable or disable the vacuum pump and the hydraulic unit, as well as to precisely set the piston position and the working temperature. The software provides control over the hydraulic pressure and the sample temperature, which

can be monitored via a thermocouple or a pyrometer. Several operational parameters can be set through the interface, such as the values of the PID (proportional – integrative – derivative) controllers or the maximum percentage of the heating power in the different temperature ranges.

The machine can be set to operate both in manual or automatic mode upon specific preferred choices. In the latter mode, the software also allows for the possibility to select a pre-set “recipe” to be used (Figure A.3). A maximum of 20 recipes can be stored in memory, with up to 6 steps, each with a selected set of parameters (heating rate, target temperature and pressure, holding time). When working in automatic mode, once the start of the sintering procedure is confirmed by the user, the machine manages everything by itself, including the vacuum pump and the hydraulic pressure.

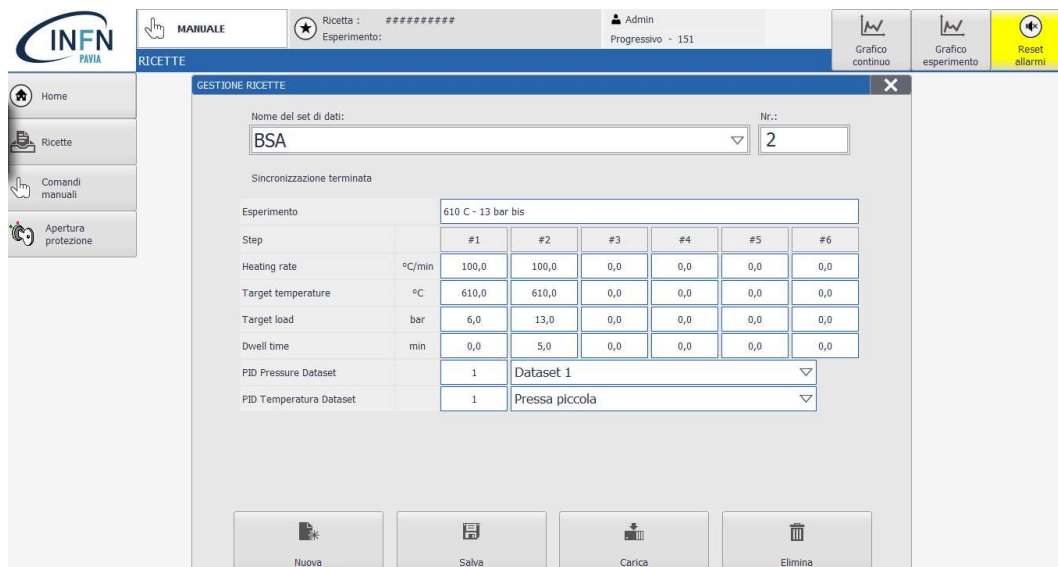


Figure A.3: User interface of TT_Sinter showing an example of pre-set recipe

After the preliminary tests, the software has been modified to make the interface more user-friendly and to make the parameters set-up further customizable. Moreover, a dual level of security was implemented, so that only privileged users can modify the recipes already in memory and other parameters, while non-expert users have only the possibility to use recipes already in memory. In addition to that, several safety checks are available: the door interlock, the maximum internal temperature at which the chamber’s door can be opened, the water flow for cooling and more. In case something is not working as it should, the user is alerted with warning messages directly on the graphic interface (Figure A.4), and the machine is re-enabled for operation only once these alarms have been reset.

During the sintering procedure, the user has the possibility to visualize in real time, through the graphical user interface, the trend of different parameters, such as the sample temperature, the applied voltage and current, the hydraulic pressure. In addition, the interface shows the piston displacement with respect to the

A.1. Machine overview

initial position when the hydraulic pressure is applied (corresponding to the decrease in the sintered sample thickness). The plots over time of all these quantities are saved together with the main settings and remain available to be downloaded by the user in different formats. Figure A.5 shows an example of the graphical interface with the evolution over time of the various parameters in a full sintering cycle.

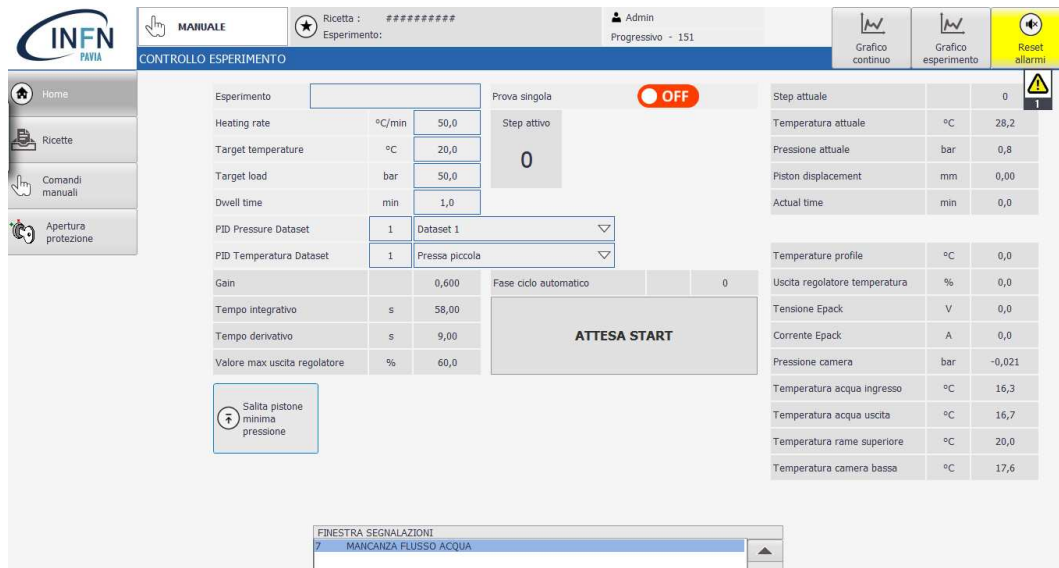


Figure A.4: User interface of TT_Sinter showing an error message

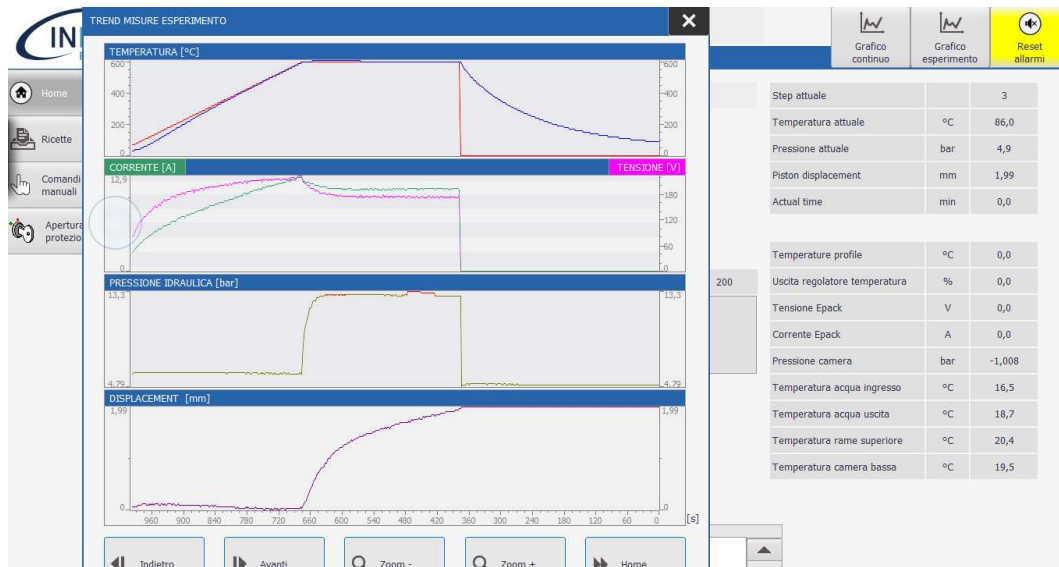


Figure A.5: User interface of TT_Sinter showing the time trend of the different parameters in a representative cycle.

A.2 Commissioning and tests

Several tests have been carried out in order to assess the machine response to selected operations. The stability at full operational regime has been tested, by setting temperature and pressure values at the limits of the achievable ranges.

The reproducibility of the procedure has been tested by sintering a considerable number of *Alliflu* samples in automatic mode with pre-saved recipes.

In this sense, the results of the first tests were disappointing: using always the same recipe and leaving untouched all other parameters, the final densities of the sintered *Alliflu* samples were too variable. Figure A.6 shows an example of two *Alliflu* samples obtained by sintering 3 grams of AlF_3+LiF powder with exactly the same procedure. As is evident from the variation in thickness, they are significantly different in density.



Figure A.6: *Alliflu* samples with significantly different densities despite being produced by sintering with the same procedure the same amount of powder

After extensive testing, we theorized that such variability could be due to subtle changes in the position of the thermocouple during the sintering procedure. Initially, the thermocouple was in fact inserted in a small hole on the side of the graphite die (Figure A.7). Even checking that it was fully inserted at the beginning of the procedure, a small change could evidently occur during sintering due to displacement of the molds, and this could lead to different results in terms of final densities. Indeed, with the thermocouple more or less in proximity of the powder, the temperature monitored could be more or less representative of the one of the sample. For example, with the thermocouple more distant from the center of the press, the detected temperature would be lower than the one of the sample, and

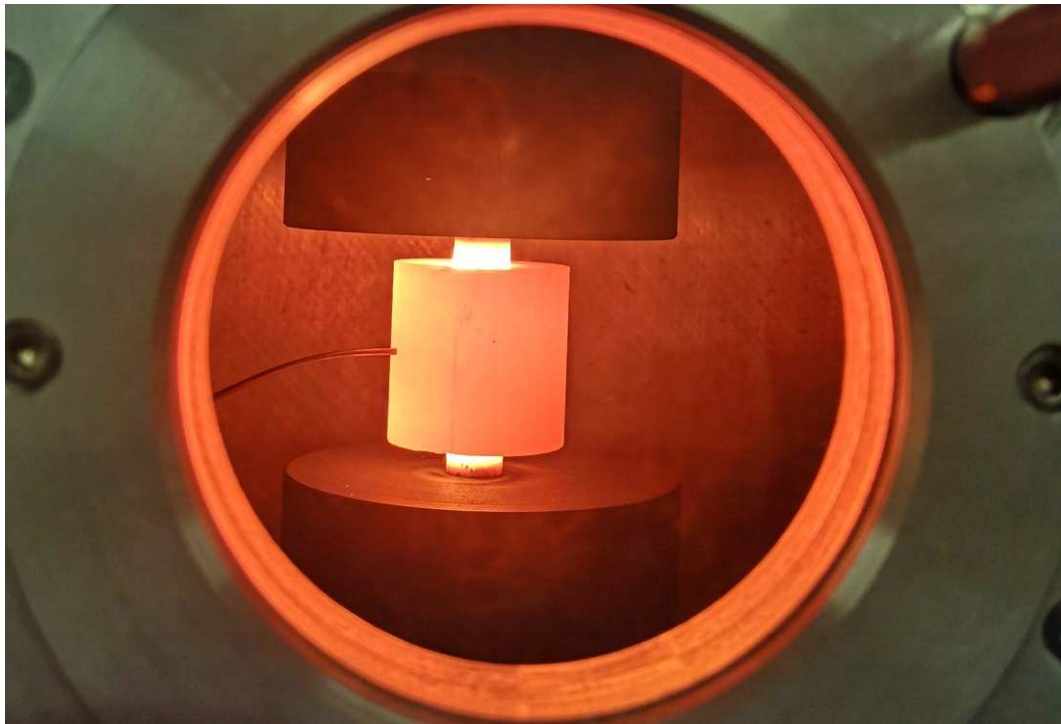


Figure A.7: Glowing graphite die at high temperature in the vacuum chamber of TT_Sinter, with the thermocouple on the left side

since the heating is carried out according to the temperature measured by the thermocouple, in this case the sample would be brought to a higher temperature resulting in a higher final density.

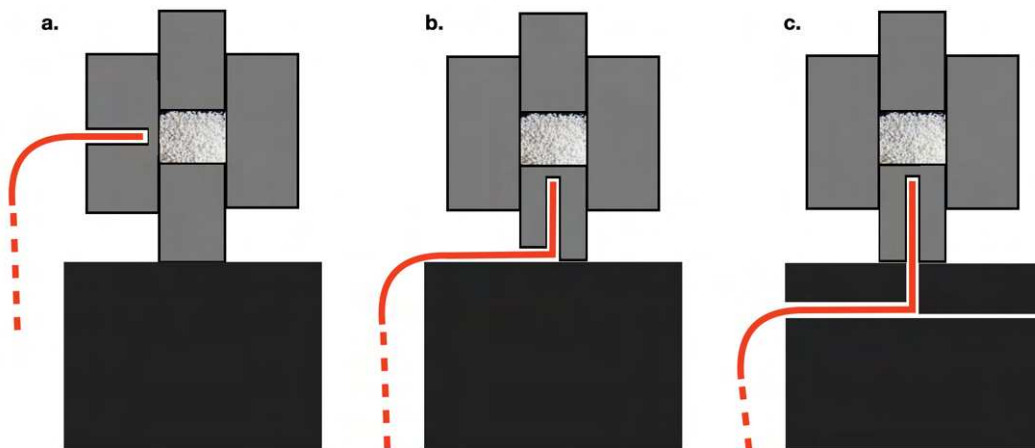


Figure A.8: Positioning of the thermocouple in the different configurations: from one side (a), from the bottom (b) and through the lower punch (c)

To analyze the problem, we re-designed the positioning of the thermocouple.

In Figure A.8 a representation of the three configurations tested for the positioning of the thermocouple, depicted in red. From the original configuration (**a** in figure), a first attempt (**b**) was made by inserting the thermocouple in the lower part of the graphite die, specifically perforated. Figure A.9 shows this modification once realized.

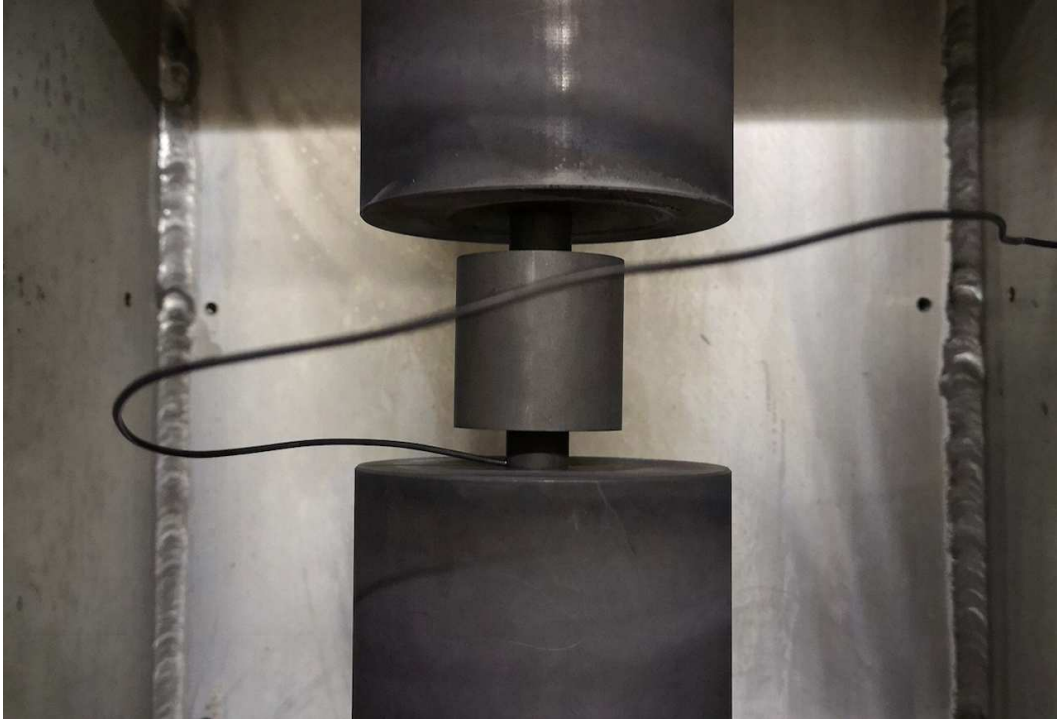


Figure A.9: Configuration **b** of Figure A.8 realized, with the thermocouple inserted in the die from the bottom

This modification actually resulted in improvements in density variability, confirming our hypothesis. However, this thermocouple configuration did not allow for a satisfactory stability of the graphite die: the weight of the die on the thermocouple is not sufficient to hold it still, with the risk of tilting the structure in the initial phase of the sintering procedure, while pressure is applied.

Therefore, we tried to stabilize the die by inserting the thermocouple directly into the lower punch (configuration **c** of Figure A.8). The punch was divided in two and in its upper part a groove was made to house and hold the thermocouple. The final realization of this configuration is shown in Figure A.10. The thermocouple is bent so that its free length exiting from the top of the punch is the appropriate one to be inserted in the die, while at the same time allowing the latter to perfectly adhere to the punch. With this configuration the stability of the die was ensured while avoiding possible displacements of the thermocouple.

Different dies are used depending on the size of the sample to sinter, thus the thickness of the punch upper part can be modulated in order to always bring the thermocouple to the same depth in the die: for example by interposing punctured



Figure A.10: Configuration *c* of Figure A.8 realized, with the thermocouple passing through the top of the lower punch

discs (the dotted area on the right in Figure A.12) between the punch and the die in the case of smaller dies.

The last configuration proved therefore to be the optimal choice in terms of the final densities of *Alliflu* samples created with the same sintering process.

Thanks to the numerous tests carried out with the machine by sintering a large quantity of *Alliflu* samples, it was moreover found that it could be advantageous to modify the recipes to further improve the outcomes of the production procedure. In fact, setting only one target temperature, the final density was always higher than the desired due to “overshooting”. In this sense, the versatility of TT_Sinter in enabling multi-step processes granted an excellent efficiency and precision: thanks to the possibility to set multi-step recipes, the target temperature was reached in two steps, a first fast heating (100°C/min) and a second slower heating (5°C/min) for the final 30°C. In this way, the target temperature is reached with considerably higher precision, resulting in a better accuracy of the density of the sintered materials.

A.3 Other applications

Once the initial phase of testing and optimizing the machine was completed, the potential applications of the machine in other fields were explored. This technol-

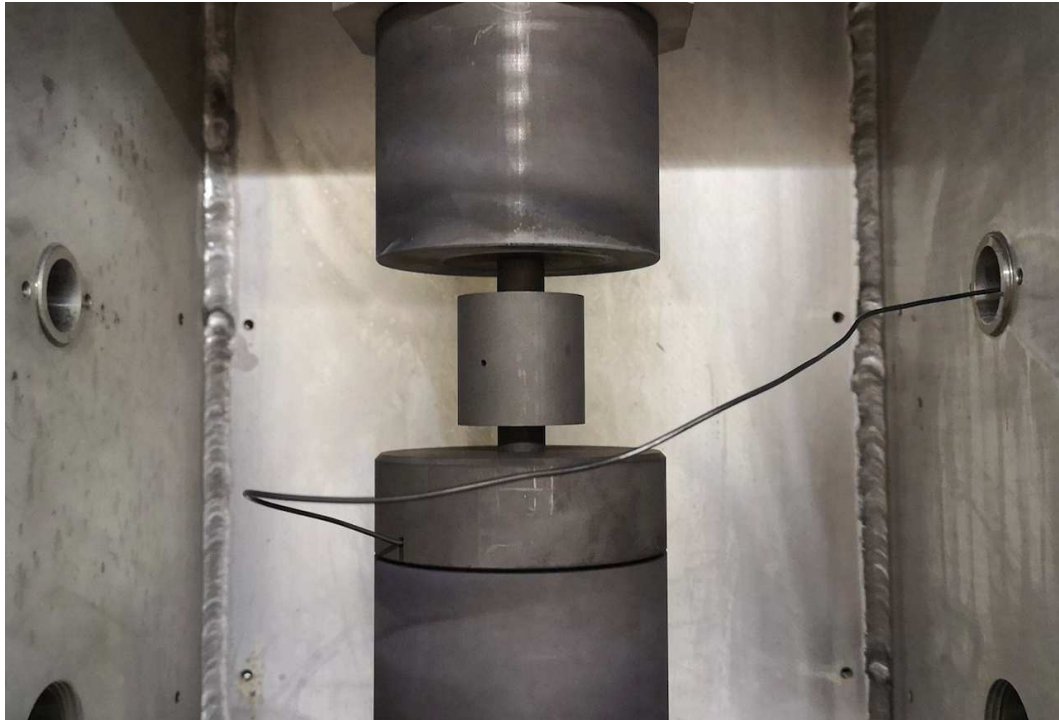


Figure A.11: Graphite die positioned in the final configuration (c of Figure A.8)

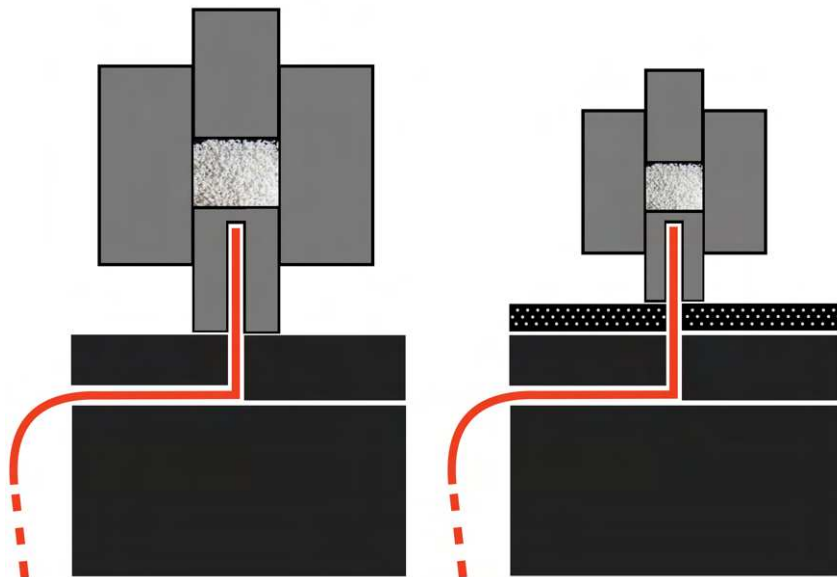


Figure A.12: Representation of the final configuration with and without an additional thickness to position the thermocouple always at the same depth in dies of different size

ogy, developed to solve a specific problem in BNCT field, can be in fact transferred to other applications, possibly after further appropriate engineering.

Targets for the technology transfer of this sintering technique and machine include, but are not limited to:

- Research laboratories: for small-medium production requiring flexibility and optimization, for material studies or for samples that need to be replaced at high rate
- Industries: for the creation and testing of new materials with a fast and reliable process in view of larger productions, or for the fabrication of sintered samples of relatively large dimensions
- Generic users dealing with the sintering of complex, multi-layer materials, such as ceramic over metal or similar.

For example, the FAST/SPS technique has been considered interesting for the R&D activities on cyclotron solid targets manufacturing in the framework of the INFN research programme LARAMED [132]. LARAMED (LABoratory of RADioisotopes for MEDicine) is a project that concerns innovative applications of nuclear physics to medicine, aiming to make LNL a reference center for the development of production methods of novel medical radionuclides.

The LARAMED team works on the cyclotron production of medical radionuclides, both commonly used such as metastable Technetium-99 (^{99m}Tc), and emerging ones with high potential medical interest, such as Copper-67, Scandium-47 and Manganese-52 (respectively ^{67}Cu , ^{47}Sc , ^{52}Mn).

The production of radionuclide ^{52}Mn has the so-called Multi-Modal Imaging (MMI) as final goal: with a perfect molecular matching between PET (Positron Emission Tomography) and MRI (Magnetic Resonance Imaging) diagnostic techniques by using both paramagnetic and radioactive properties of certain manganese isotopes, a very promising hybrid imaging modality PET/MRI could be achieved. Manganese-52/51 can be produced with 10-20 MeV protons on targets of natural chromium, mainly through the $^{52}\text{Cr}(p,n)^{52m/g}\text{Mn}$ and $^{53}\text{Cr}(p,2n)^{52m/g}\text{Mn}$ nuclear reactions.

In this framework, TT_Sinter has been considered extremely advantageous for the preparation of the targets, which is one of the most crucial points when creating radionuclides by cyclotrons [133].

In fact, with FAST/SPS the losses of the material to be sintered are almost completely avoided, and this represents a critical aspect when using isotope-enriched materials, generally quite expensive. Furthermore, the possibility of joining similar or dissimilar materials without any filler could be exploited to bond the target with the backing. This would allow an improvement in heat dissipation with consequent possible delivery of higher beam currents, therefore a greater radionuclide yield could be achieved.

Given the high potential of TT_Sinter in the described applications, a second machine, identical to the one shown in Figure A.2, was put into production with

the aim of installing it at the Legnaro National Laboratories. There, it will be exploited for the production of several medical radioisotopes, by expanding the portfolio of materials used for solid cyclotron targets.

Before the transfer to LNL, preliminary tests were carried out on the machine already in operation at the Mechanical Workshop of the Pavia to investigate further optimization or modifications needed for the use in cyclotron targets production.

For example, the manufacturing of a target of natural chromium (^{nat}Cr) on niobium backing with gold interlayer was tested. The gold foil, with purity 99.95% and thickness $25\ \mu\text{m}$, is used as a chemically inert protective interlayer. First, the adhesion of the Au foil on the Nb support with diameter 2.35 cm (Figure A.13) is achieved via FAST/SPS without a die, in “open mode”. Then, ^{nat}Cr powders (99.5% purity) are pressed in a standard press die with diameter 1-1.5 cm, resulting in pellets with thickness of about 0.4 mm (Figure A.14). The obtained pellets, are finally press-bonded to the Nb-based backing, again via SPS in open mode. A representative final target produced in this way during the tests with TT_Sinter is shown in Figure A.15.



Figure A.13: Thin layer of gold and niobium backing bond-pressed with TT_Sinter

A second round of tests on targets will be performed before the end of the year, to refine details and to conclude the commissioning phase before the transfer of the new machine to LNL.



Figure A.14: Pellet of natural chromium sintered with TT_Sinter

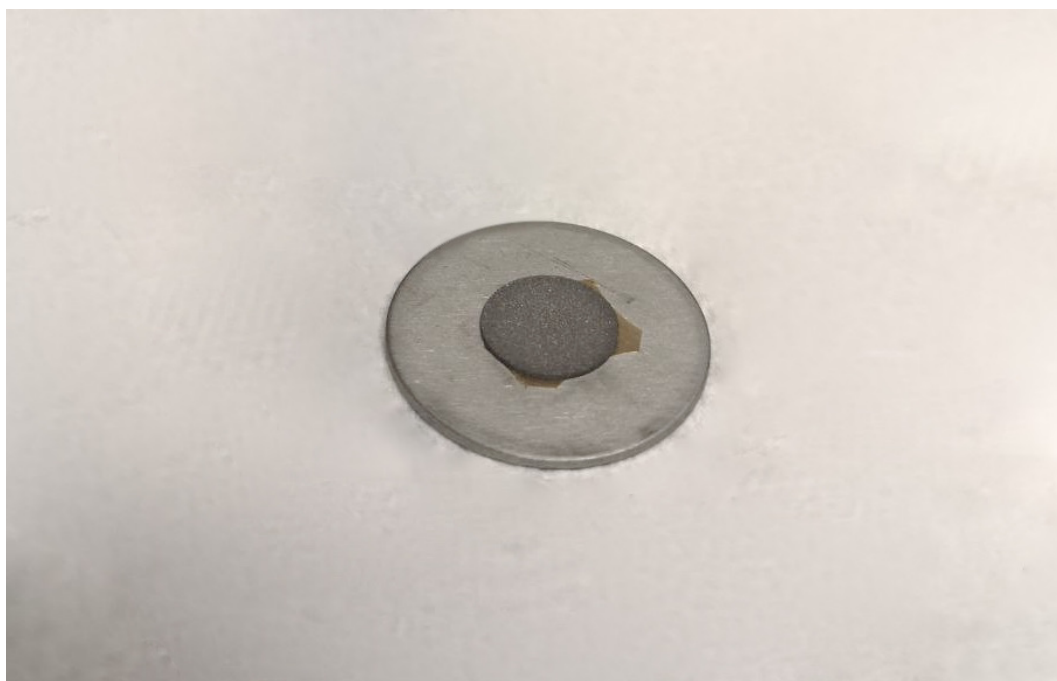


Figure A.15: Final ^{nat}Cr target on Nb-based backing, manufactured with TT_Sinter

BSA prototype

In the following, the different steps of the design for the BSA prototype are reported. As already illustrated, the purpose of this part of the work was the design and construction of a prototype with the essential characteristics of the BSA developed for the RFQ, in order to experimentally validate the synergy between the BSA materials in moderating neutrons. Obviously, this structure is not intended to be a reproduction of the clinical BSA, it would in fact be impossible to build a copy of the latter for the measurements at LNL. Rather, we aimed to create a representative structure of the BSA leading to an optimized data collection about the effect of the different materials on the neutron spectrum.

To this end, we simulated different configurations of the BSA prototype, to find the most appropriate for our purposes and at the same time feasible, based on the resources at our disposal. Several Monte Carlo simulations were carried out by using the MCNP6 code with the neutron source described in the second Chapter.

In the simulations, neutron flux tallies (F2-type) were set at the beam-port and at increasing distances along the direction of the beam: in two concentric disks with a radius of 2.5 and 12 cm at the beam-port and then at distances of 20, 40, 60, 80 and 100 cm. The neutron current was also evaluated in concentric discs centered on the beam axis (F1-type tally), as a function of the distance from the beam-port, and changing the radius, in order to verify the collimation achieved. Three energy bins were set for the tallies, to separate the different contributions related to thermal, epithermal and fast neutrons.

B.1 First configuration

The geometry of the first configuration is shown in Figure B.1 (dimensions not to scale), in which the white part, representing *Alliflu*, has variable thickness as it will be in the experimental situation.

The two elements around the *Alliflu* core are cylindrical shells, the innermost is a reflector made of lead (Pb), the other is an absorber of ordinary polyethylene

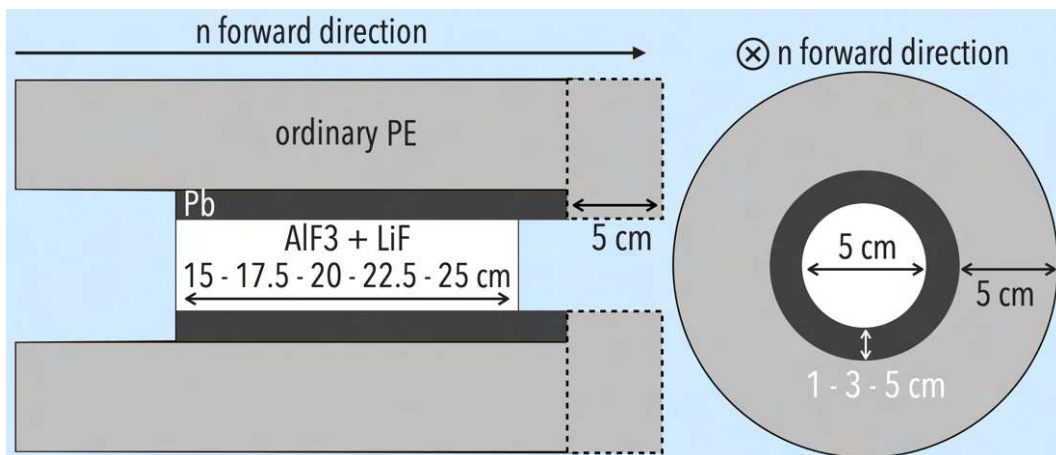


Figure B.1: Representation (not to scale) of the first configuration tested for the BSA prototype: vertical sections respectively parallel (left) and orthogonal (right) to the forward direction of neutrons from the Be target

(PE “screen”). Within this shell, the most suitable thickness of the Pb reflector is studied by varying it from 1 to 5 cm. It was demonstrated that the most efficient neutron reflection requires a lead cylinder 5 cm thick. The PE screen has a thickness of 5 cm and surrounds the reflector and the *Alliflu* core. At the beam-port, a borated PE collimator 5 cm long was also added (the area bounded by the dashed line in figure). This collimator is a cylinder with a hole of 5 cm in diameter with an external radius equal to the external radius of the BSA prototype, so as to cover the Pb reflector at the beam-port.

Results

Figure B.2 shows the radial trend of the current at the beam-port. The results obtained with 15 cm of *Alliflu* core are shown as a representative thickness of the moderator.

It is evident that *Alliflu* without the BSA structure (red line: 0 cm of Pb and no shell) does not generate a neutron beam. In fact, neutron current is higher for radius values greater than the beam-port. Adding a 5 cm thick cylindrical shell of reflector in Pb (blue line) a beam begins to form, albeit with poor collimation. By adding PE as a shield, we collimate the beam more, but a high thermal neutron current is generated (bottom left plot). The grey line represents the current obtained by further adding the collimator made up of borated PE, 5 cm thick. The bottom left plot shows that the thermal component is suppressed (grey line vs purple line) while leaving almost unchanged the epithermal component (bottom center plot, with grey and purple lines almost completely superimposed).

Figure B.3 shows the current as a function of the distance from the beam-port, in the configuration provided with the collimator. The plots above are the integral current in the disk corresponding to the beam-port as a function of the

B.1. First configuration

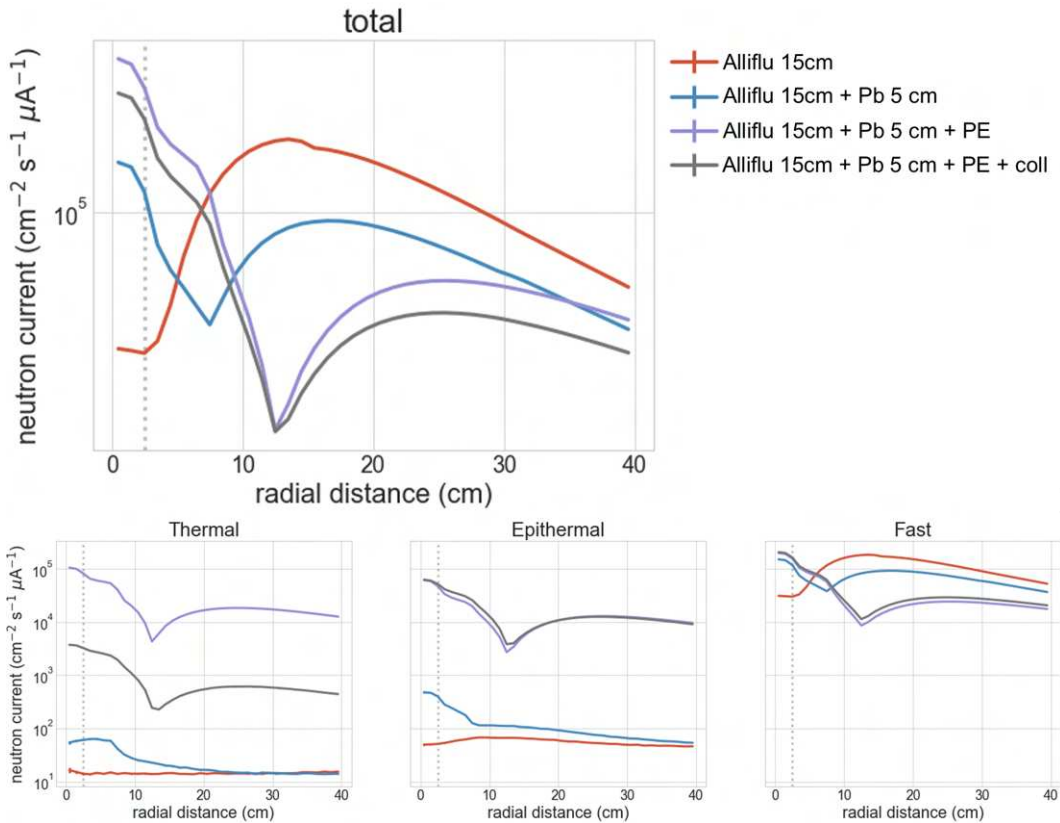


Figure B.2: Radial trend of the current per unit area, per μA of proton current at the beam-port. The upper plot shows the total neutron current, the 3 plots below represent the current for the thermal, epithermal and fast components. Red line: without BSA structure; blue line: with 5 cm of Pb; purple line: with 5 cm of Pb and PE shield; grey line: with 5 cm of Pb, PE shield and borated PE as collimator. All the layouts have 15 cm of Alliflu. Tallies were obtained at the beam-port.

distance. The second row of plots are the current in disks crowns of increasing radii at fixed distances (0, 20, 40, 60 and 100 cm). It emerges that the collimation obtained is not sufficient, since already at 20 cm from the beam-port there is no difference between the current calculated in the beam area and in the outer crowns of increasing radius.

Finally, Figure B.4 shows the neutron spectrum for the four layouts mentioned above, integrated in the beam cross section area. The plots show that the materials around the *Alliflu* core help to increase the total flux in the beam (the red line is lower than the others) and PE helps to concentrate neutrons in the epithermal part of the spectrum.

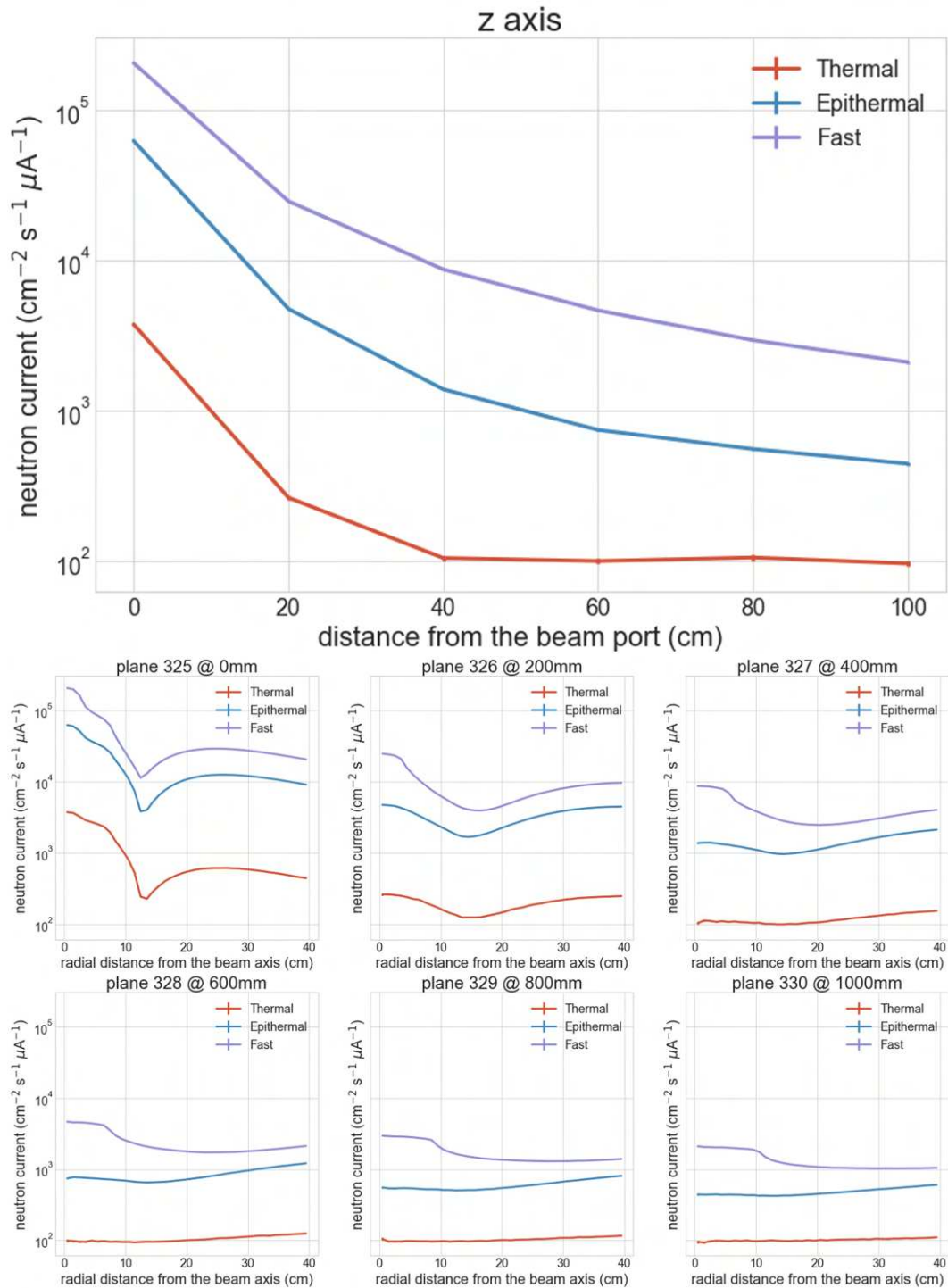


Figure B.3: Current per unit area per μA of proton current at the beam-port. Configuration with 15 cm of Alliflu, 5 cm of Pb and borated collimator. In the upper plot, current as a function of the distance from the beam-port for fast (purple), epithermal (blue) and thermal (red) neutrons. The following plots show the radial trend of the current with respect to the center of the beam for different distances from the collimator port

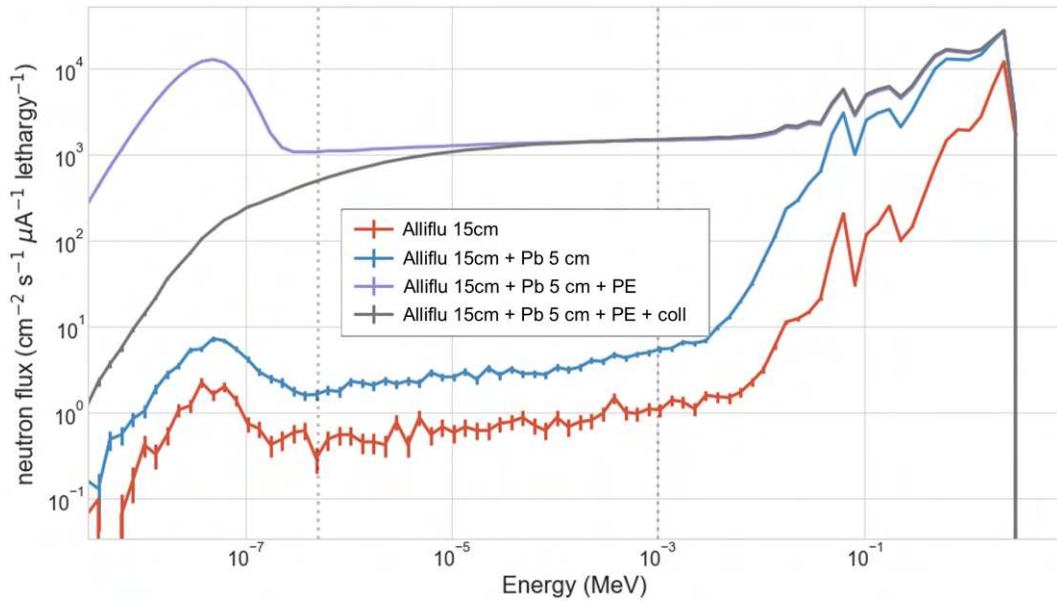


Figure B.4: Neutron spectrum per μA of proton current at the beam-port. The lines represent the different variants of this configuration. All layouts have 15 cm of Alliflu. Red line: with no BSA; blue line: with 5 cm of Pb; purple line: with 5 cm of Pb and PE screen; grey line: with 5 cm of Pb, PE around the cylinder and collimator of borated PE

Conclusions

This configuration allowed to study the effect of the materials, showing the need for a higher collimation, especially if the detector is placed away from the beam-port, as in the case of DIAMON. The prototype was further optimized to reach this goal. The collimator of borated PE at the beam-port must be suitably modulated to absorb the neutrons which are not useful for the generation of the desired neutron beam. For these reasons we modified the prototype as described in the next section.

B.2 Second configuration

Figure B.5 shows the second configuration, again setting the length of *Alliflu* at 15 cm as a representative case, and matching the lengths of the reflector and of the moderator. Compared to the previous geometry, we kept the thickness of the reflector fixed (5 cm, the thickness that guarantees the best neutron reflection ratio in the *Alliflu* core), while we varied the thickness of the PE shell between 5 and 25 cm. The collimator was also enlarged and lengthened to 10 cm. As before, normal PE was used as shielding material, while in the collimator we used borated PE enriched with the 5% in mass of natural boron.

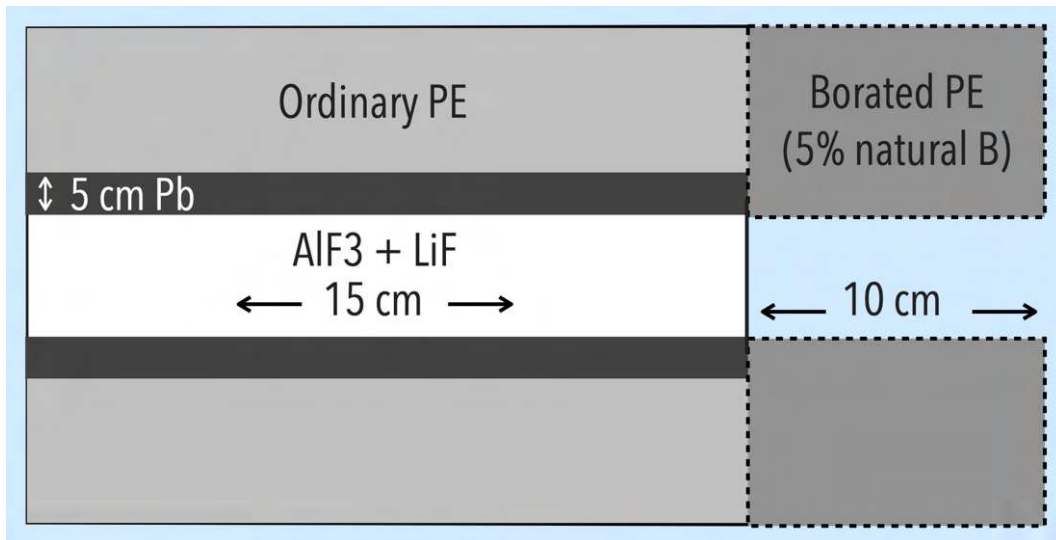


Figure B.5: Representation (not to scale) of the second configuration tested for the BSA prototype (vertical section parallel to the forward direction of neutrons from the Be target)

Results

Figure B.6 shows the radial trend of the current at the beam-port with 15 cm long *Alliflu* and 5 cm thick Pb surrounding it. As screen, we considered the thickest one: 25 cm of ordinary PE. The plots compare the open-beam (no moderator, no BSA), the BSA without moderator (5 cm-thick Pb reflector, 25 cm-thick shield and 10 cm long collimator) and the BSA with 15 cm of moderator. Compared to the previous configuration, the beam is now much more collimated.

Figure B.7, reporting the current for the BSA+moderator, shows how the collimation, good at the beam-port, is still not optimal as the distance increases, in fact it already degrades at a distance of 20 cm from the beam-port. This could be a problem when using the DIAMON detector, which in previous experiments was placed at 130 cm from the beam-port.

To conclude, Figure B.8 shows the neutron spectrum. The red line is the open beam, without any BSA. The blue line is the spectrum of the BSA prototype layout without *Alliflu* core. In this configuration, a very high fast spectral component is obtained at the beam-port. If we now consider the spectrum when inserting the *Alliflu* core in the BSA prototype (purple line), the fast component is significantly moderated, without a substantial decrease of the epithermal component.

Conclusions

Compared to the first configuration, the second BSA prototype guarantees a better collimation of neutrons at the beam-port. This would allow to place the detector in that position in order to better measure the energy spectrum of the neutron

B.2. Second configuration

field, with less contamination from scattered neutrons. Furthermore, it is now clearly visible how *Alliflu* affects the shape of the spectrum: by measuring the spectrum with the central part of the BSA prototype filled with increasing thickness of *Alliflu*, it is possible to evaluate the moderation properties of this material. Moreover, a validation of the simulations can be obtained.

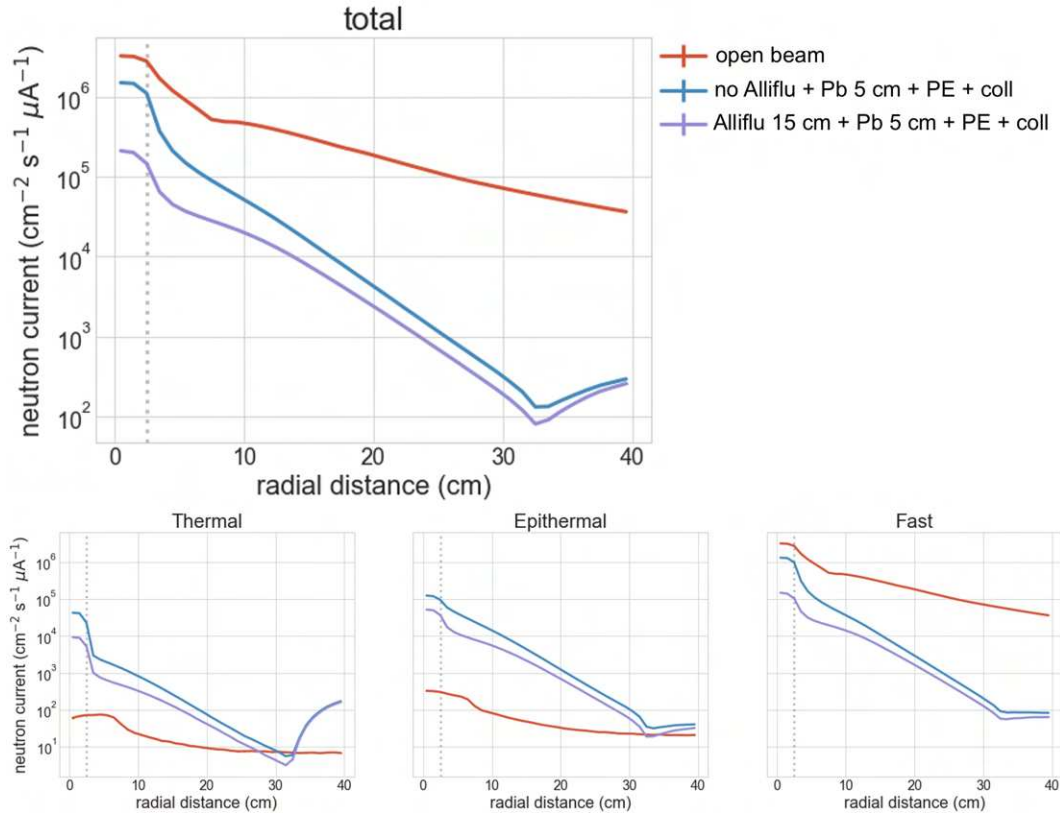


Figure B.6: Radial trend of the current per unit area per μA of proton current at the beam-port. The first plot shows the total neutron current, the next 3 plots represent the current for the thermal, epithermal and fast components. Red line: open beam (without *Alliflu*, reflector and screen); blue line: without *Alliflu*, with 5 cm of Pb reflector, 25 cm of PE screen and collimator in borated PE; purple line: with 15 cm of *Alliflu*, 5 cm of Pb reflector, 25 cm of PE screen and collimator in borated PE

These studies indicates that for the BSA prototype, in addition to variable thicknesses of *Alliflu*, are needed:

- Pb cylindrical shell, 25 cm long, 5 cm thick and hole of 5 cm diameter
- Borated PE cylinder, 65 cm diameter, perforated in the center (5 cm diameter hole), with length at least 10 cm
- Perforated PE cylinder, with 25 cm length and 65 cm diameter, and perforated in the center (hole with 15 cm diameter)

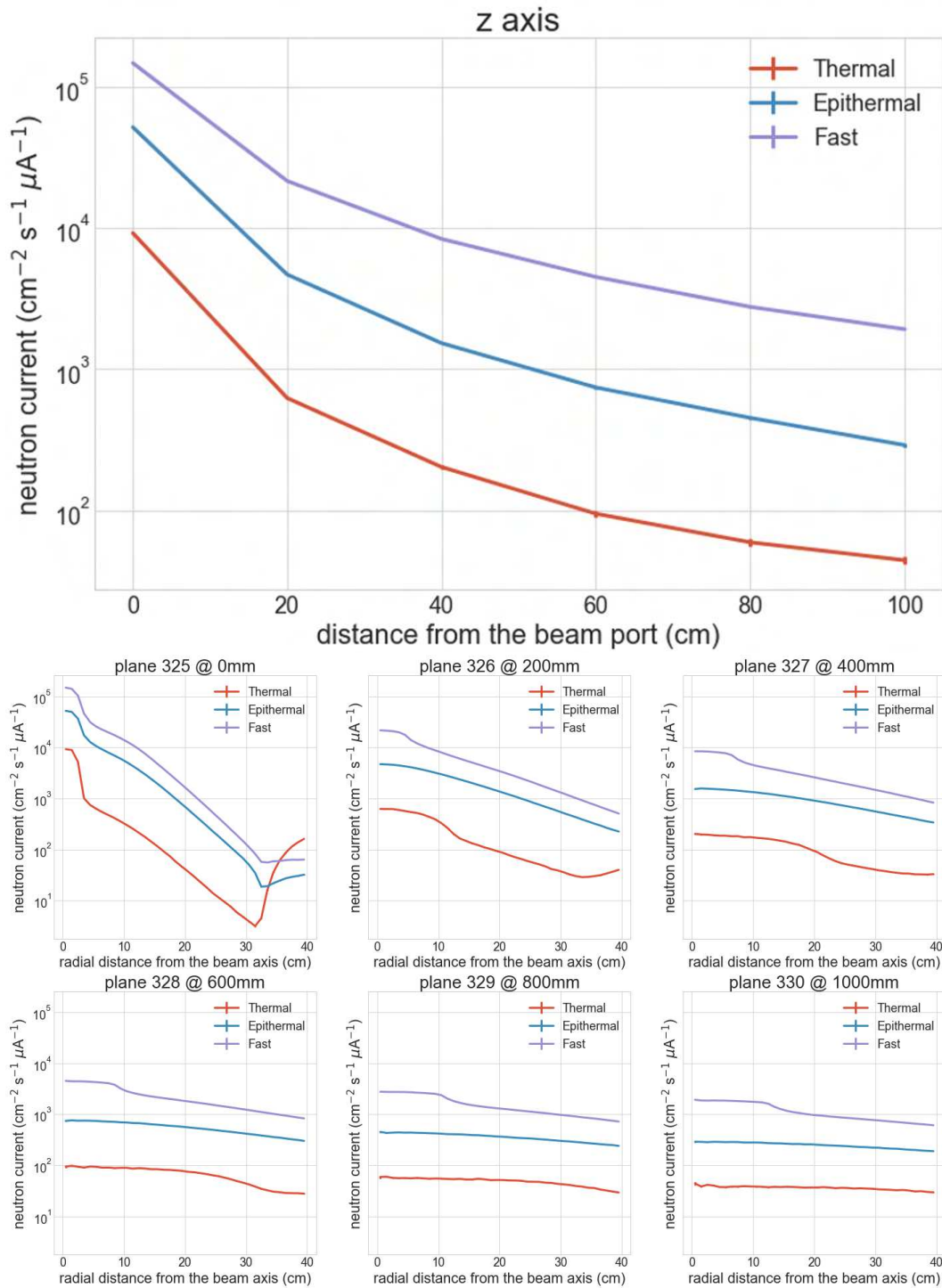


Figure B.7: Current per unit area per μA of proton current at the beam-port with 15 cm of Alliflu, 5 cm of Pb and 25 cm of shield. The first plot shows the current as a function of the distance from the beam-port for fast (purple line), epithermal (blue line) and thermal (red line) neutrons. The plots below show the radial trend of the current with respect to the center of the beam for increasing distances

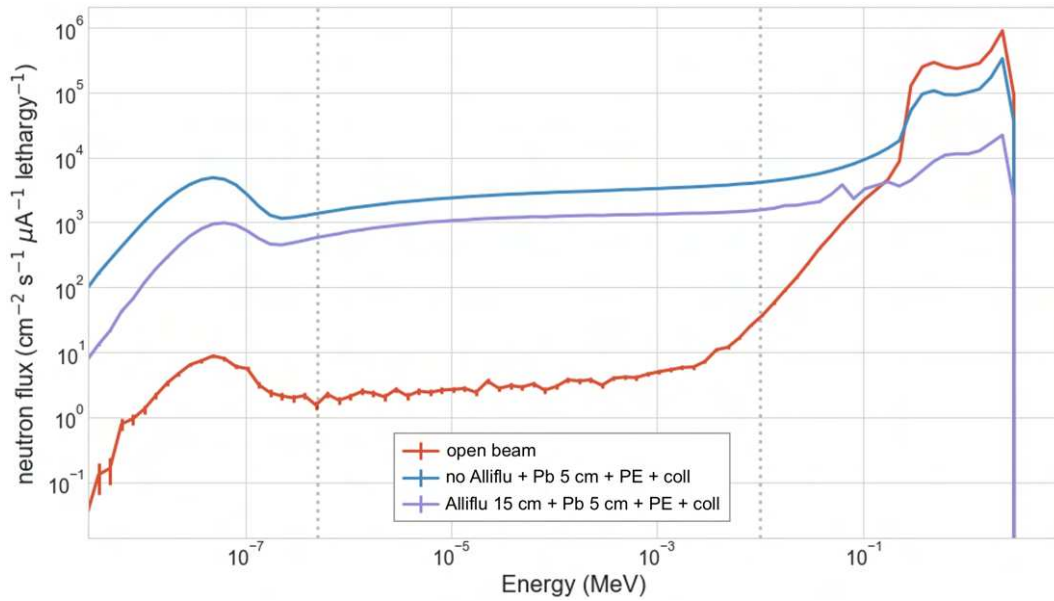


Figure B.8: Neutron spectrum per μA of proton current at the beam-port. Red line: open beam (without Alliflu, reflector and screen); blue line: without Alliflu, with 25 cm of PE screen, 5 cm of Pb reflector and collimator in borated PE; purple line: with 15 cm of Alliflu, with 25 cm of PE screen, 5 cm of Pb reflector and collimator in borated PE

B.3 Third configuration

To further improve the performance of the prototype, we modified the structure of the second configuration by studying different lengths of the borated PE collimator.

Furthermore, instead of using a borated PE shell, we tested a 1 cm-thick layer of borated PE interposed between the Pb reflector and the ordinary PE screen. The outer diameter of the ordinary PE layer was left unchanged with respect to the second configuration: we tested also in this case thicknesses of 10, 15, 20 and 25 cm around the reflector, but divided into an innermost layer of 1 cm of borated PE, and one outermost layer of 9, 14, 19 and 24 cm respectively of ordinary PE. The simulations were carried out with or without the presence of this intermediate borated layer.

The best configuration resulted the one with a total PE thickness of 25 cm, of which the innermost layer of 1 cm is of borated polyethylene.

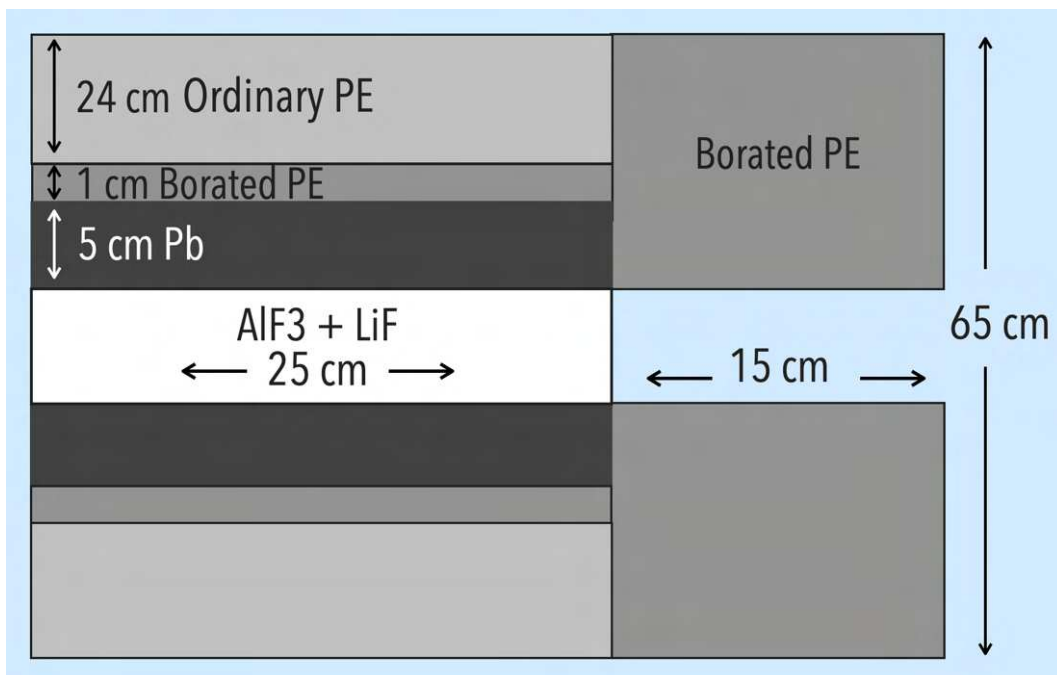


Figure B.9: Representation (not to scale) of the third configuration tested for the BSA prototype

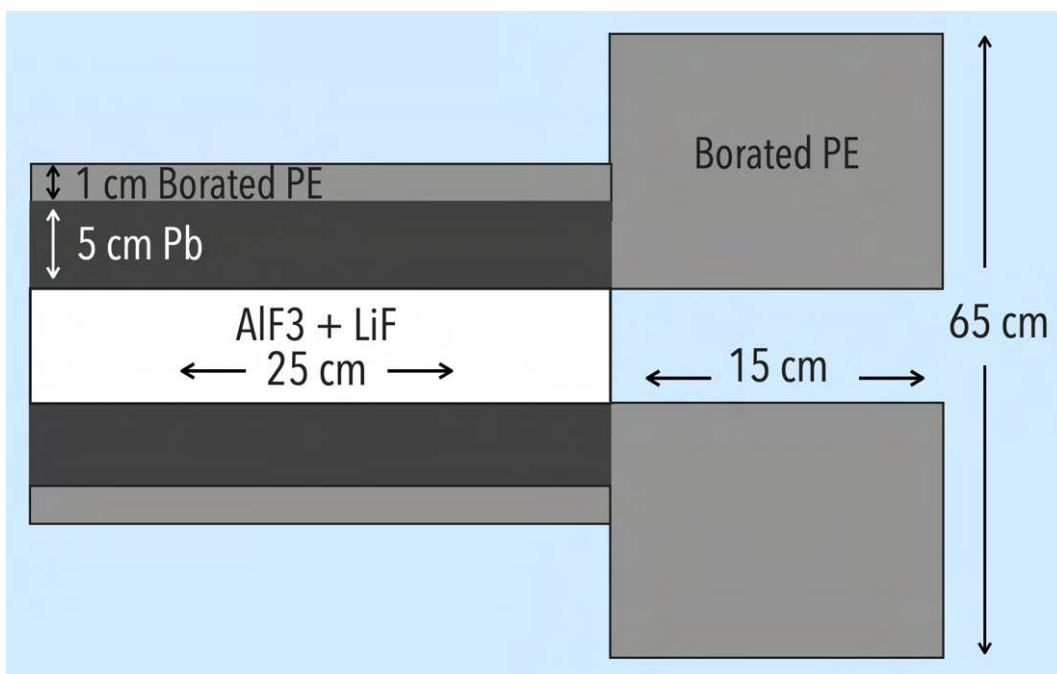


Figure B.10: Representation (not to scale) of the third configuration tested for the BSA prototype, without PE screen

B.3. Third configuration

Figure B.9 shows therefore the third configuration, with the length of the borated PE collimator increased to 15 cm based on the optimization obtained. On the basis of this configuration, 7 PE discs with a thickness of 2.5 cm were purchased, for a total of 17.5 cm in length, in order to obtain 15 cm also considering possible material losses due to machining. The upstream part, including the Pb reflector and the cylindrical shells of borated and ordinary PE, has been lengthened to 25 cm to allow the housing of a larger quantity of *Alliflu*, currently available.

We investigated in detail the effect of the ordinary PE shell, to quantify the advantage derived from its presence. Therefore, starting from the configuration of Figure B.9, those represented in Figures B.10 and B.11 were also simulated: respectively without ordinary PE shell and without ordinary PE shell but with the presence of an extension of Pb as an additional reflector in the area for the target housing (in this area we are limited by the size of the target cooling system which requires a larger diameter, see Figure 3.1).

We verified that the extension of the Pb reflector does not produce significant advantages, therefore only the results related to the configuration of Figure B.10 are reported, in order to show the effect of the PE shell.

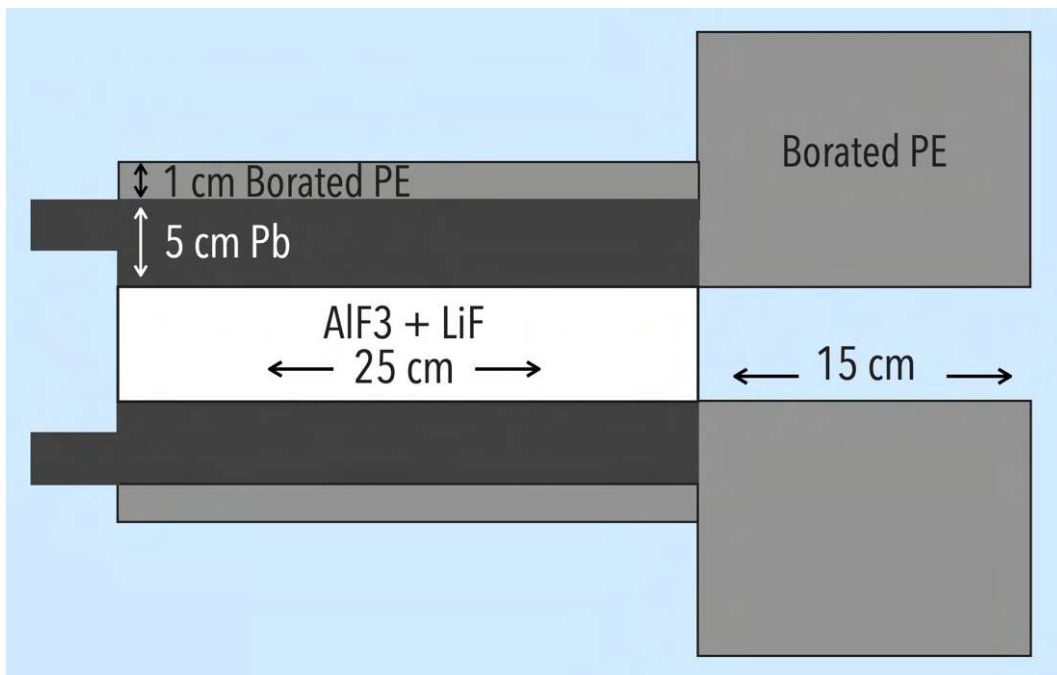


Figure B.11: Representation (not to scale) of the third configuration tested for the BSA prototype, without PE screen but with an additional Pb reflector around the target

Results

Figure B.12 shows the radial trend of the neutron current at the beam-port for the third configuration (Figure B.9).

The following figures illustrate the effect of the presence of the PE screen: Figure B.13 compares the collimation with and without PE screen (with the 1 cm shell of borated PE), showing the radial trend of the neutron current at the beam-port for the configurations in Figure B.9 and in Figure B.10, with and without 25 cm of *Alliflu*. Here the red line shows the effect of 25 cm of *Alliflu* alone. Figure B.14 shows the neutron spectra at the beam-port and at a distance of 80 cm from it, for each layout and for the situation with *Alliflu* only.

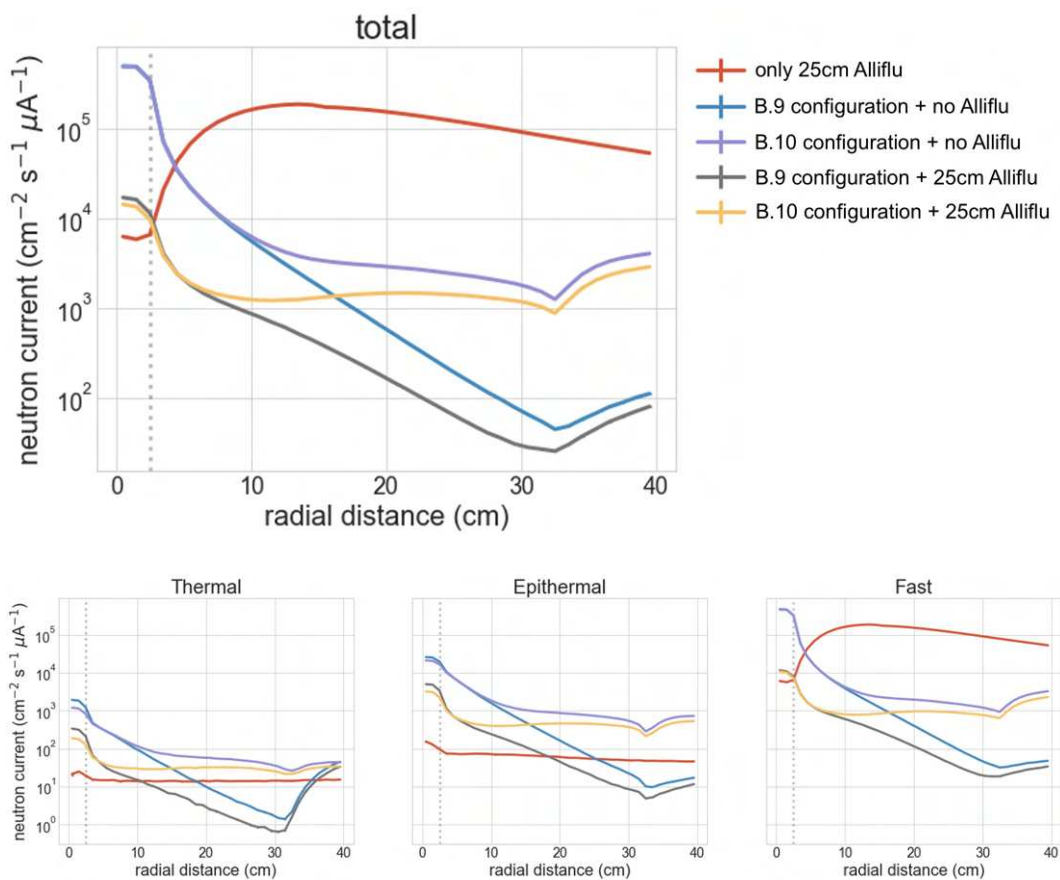


Figure B.13: Radial trend of the neutron current (tallied at the beam-port) per unit area per μA of proton current. The plots show the comparison between: 25 cm of *Alliflu* alone (red line), complete configuration of Figure B.9 with ordinary PE shell (blue line: without *Alliflu*; gray line: with 25 cm of *Alliflu*) and configuration of Figure B.10 without ordinary PE shell but with 1 cm of borated PE (purple line: without *Alliflu*; yellow line: with 25 cm of *Alliflu*). In the upper plot the total current, in the following the energy components separated

B.3. Third configuration

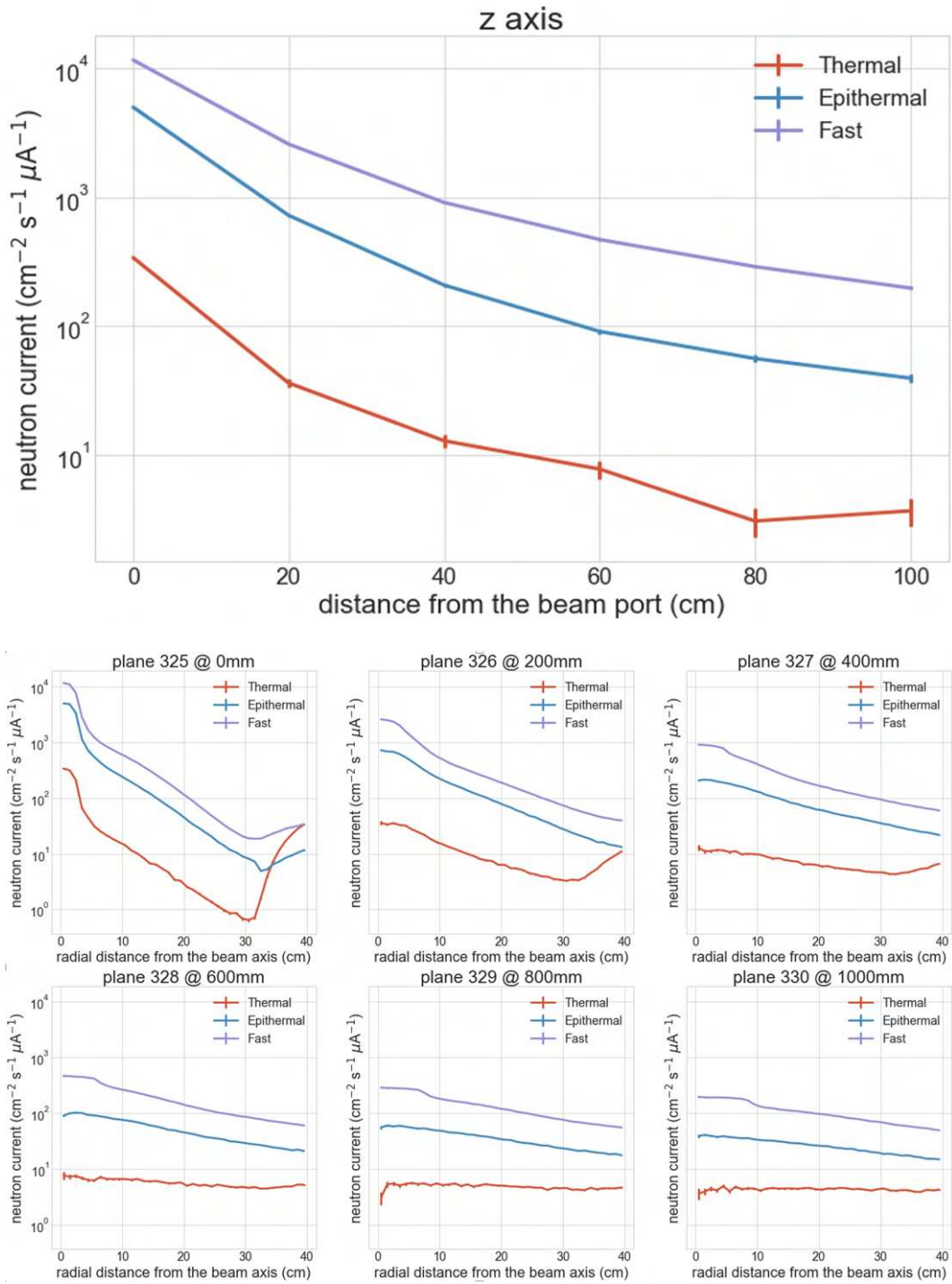


Figure B.12: Radial trend of the neutron current per unit area per μA of proton current associated to the configuration of Figure 18: complete configuration with Alliflu 25 cm long, shell of borated PE 1 cm thick, shell of ordinary PE 24 cm thick, final collimator of borated PE 15 cm long

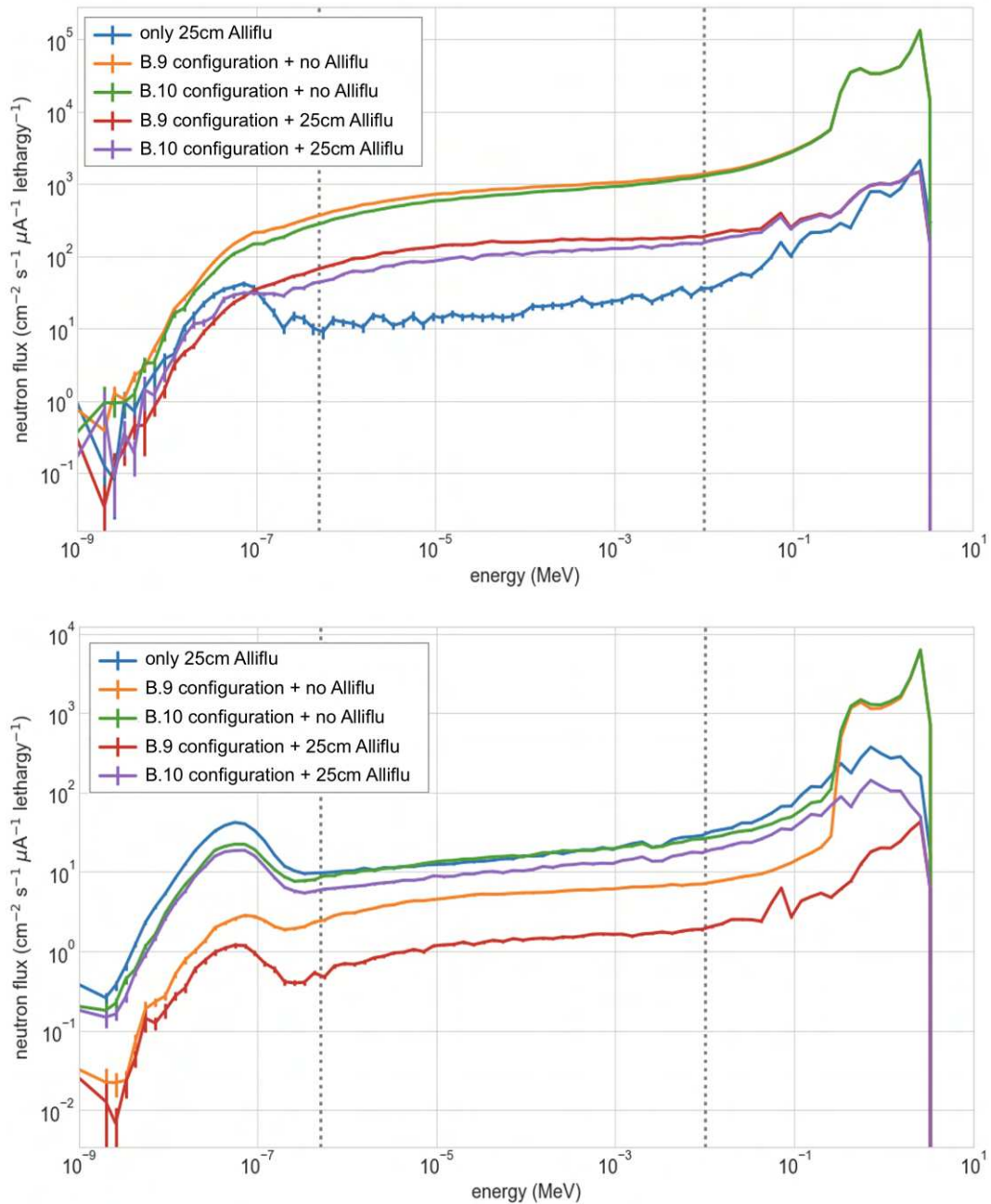


Figure B.14: Neutron spectra (in log-log representation) at the beam-port (upper plot) and at a distance of 80 cm from it (lower plot). The configurations of Figures B.9 and B.10 are compared along with the situation with only 25 cm of Alliflu. BSA with borated PE and ordinary PE is represented by the orange line (without Alliflu) and red line (with 25 cm of Alliflu); the BSA with only a borated PE shell is represented by the green (without Alliflu) and purple lines (with 25 cm of Alliflu)

Conclusions

The presence of the PE outermost shell does not produce substantial differences at the beam-port with or without the *Alliflu* core, but at a distance of 80 cm the effect is interesting: without PE, *Alliflu* produces a substantial change in the detected spectra only in the fast part, while with PE a more pronounced modification of the spectrum is achieved even in the epithermal part, which is reduced by a factor of 2 but with a higher suppression in the fast area. In this sense, the prototype corresponds to the effect of the clinical BSA, which has precisely the purpose of lowering the contamination of fast neutrons, harmful to the patient, without depressing the epithermal flux which is instead important for the treatment.

The usefulness of the PE screen appears evident in the comparison between the situations with or without the *Alliflu* core. Figure B.15 show the ratios of the neutron fluxes with no *Alliflu* or with 25 cm of *Alliflu* as a function of the distance from the beam-port. The flux ratios are shown for each energy component (thermal, epithermal and fast neutrons) and with or without the presence of the PE screen (thus for the layouts of Figure B.9 and Figure B.10). It can be noted that, with the only exception of the epithermal component in close proximity to the beam-port, the lines related to the presence of the PE screen are always higher than the corresponding lines without PE. This indicates how the PE shell helps to detect the effect of *Alliflu* on the neutron spectra.

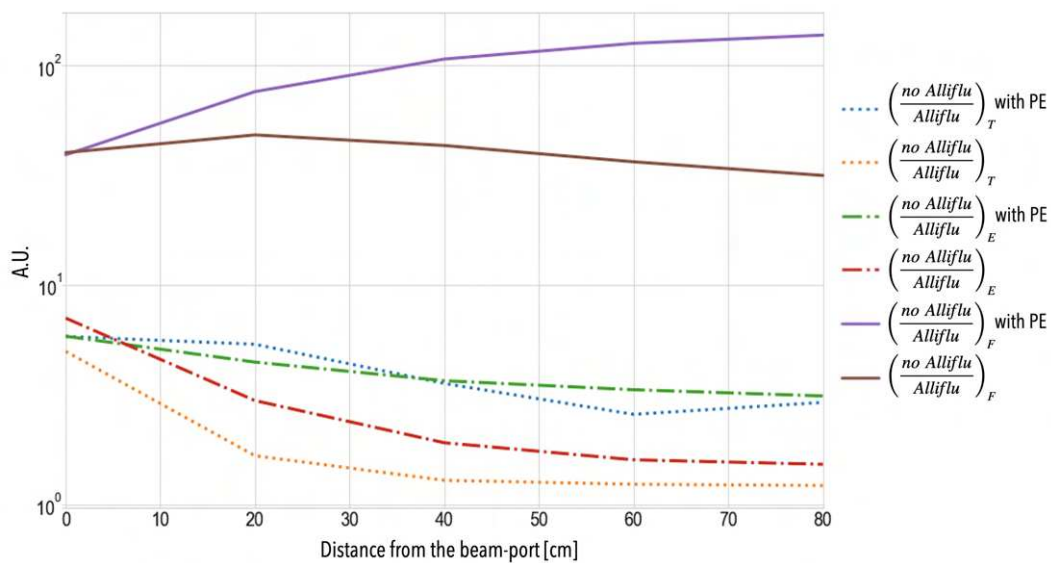


Figure B.15: Ratios of the neutron fluxes with no *Alliflu* or with 25 cm of *Alliflu* as a function of the distance from the beam-port. For each component (thermal, epithermal and fast) the ratios are shown with or without the presence of the PE outermost shell around the reflector, thus comparing the situations of Figure B.9 and Figure B.10

To program the measurements, we therefore planned to proceed with a first experimental run with no PE screen, in which the measurement refers to a situation more similar to that of clinical BSA (higher epithermal component). Another run of measurements will be carried out in 2022 adding the outermost PE shell, in order to obtain more differentiated data on the whole neutron spectrum.

B.4 Summary and final configuration

A very high number of Monte Carlo simulations was run to test different layouts of the BSA prototype for the measurements at LNL, of which only a portion has been described here. The main steps of the design of the BSA prototype have been 3 different configurations, each one of them was tested in different variants to identify the best geometry for our purposes. Table B.1 lists the three phases of the design, with the amount of related simulations carried out and a summary of the associated outcomes.

The third configuration resulted to meet our expectations both for the collimation and for the effect of the different materials in moderating the neutrons. The configuration built at the INFN Mechanical Workshop for the measurements described in this thesis is the one reported in Figure B.10, *without* the PE screen that will be added later for other future experiments.

Table B.1: Summary of the different phases of the design of the BSA prototype with simulations carried out with MCNP6

Phase	Simulations	Tallies	Outcomes
first	65	16380	First studies about the contribution of the BSA on the spectrum. Selection of the thickness of the Pb (5 cm cylindrical shell). Verified the necessity to add material around the moderator to absorb the scattered neutrons and insert a collimator.
second	18	4536	A 25 cm thick PE cylindrical shell around the BSA is sufficient to moderate most of the scattered neutrons. Collimator in borated PE useful to eliminate the thermal contribution to the beam-port
third	24	6048	Elimination of the small thermal contribution remained at the end of the second phase: solved by adding a 1 cm thick cylindrical shell between the layers of Pb and PE. Elongation of the final part and verification of the effect of the outermost polyethylene layer

Bibliography

- [1] WHO (World Health Organization) (2020) *WHO report on cancer: setting priorities, investing wisely and providing care for all*, World Health Organization 2020. <https://apps.who.int/iris/handle/10665/330745>
- [2] NCI (US National Cancer Institute) website, accessed on 17 July 2020. <https://www.cancer.gov>
- [3] IARC (International Agency for Research on Cancer) website, accessed on 17 July 2020. <https://www.iarc.who.int>
- [4] Barth R.F., Vicente M.G., Harling O.K., Kiger W.S.III, Riley K.J., Binns P.J., Wagner F.M., Suzuki M., Aihara T., Kato I. and Kawabata S. (2012) *Current status of Boron Neutron Capture Therapy of high grade gliomas and recurrent head and neck cancer*, *Radiation Oncology* 7(146):1-21. <https://doi.org/10.1186/1748-717X-7-146>
- [5] Allen B.J. (1983) *The Neutron Capture Process* in: Böckhoff K.H. (eds) *Nuclear Data for Science and Technology*, Springer. https://doi.org/10.1007/978-94-009-7099-1_154
- [6] Sauerwein W.A.G., Bet P.M., Wittig A. (2012) *Drugs for BNCT: BSH and BPA* in: Sauerwein W., Wittig A., Moss R., Nakagawa Y. (eds) *Neutron Capture Therapy*, Springer. <https://doi.org/10.1007/978-3-642-31334-9>
- [7] Soloway A.H., Barth R.F., Gahbauer R.A., Blue T.E. and Goodman, J.H.J. (1997) *The rationale requirements for the development of boron neutron capture therapy of brain tumors*, *Journal of Neuro-Oncology*. 33:9-18. <https://doi.org/10.1023/A:1005753610355>
- [8] Bortolussi S., Liu Y.-H. and Porras I., (2021) *Boron Neutron Capture Therapy: From Nuclear Physics to Biomedicine*, *Biology* 10:370. <https://doi.org/10.3390/biology10050370>

- [9] Hanif F., Muzaffar K., Perveen K., Malhi S. and Simjee S. (2017) *Glioblastoma Multiforme: A Review of its Epidemiology and Pathogenesis through Clinical Presentation and Treatment*, Asian Pacific Journal of Cancer Prevention, 18(1):3-9. <https://doi.org/10.22034/APJCP.2017.18.1.3>
- [10] Moss R.L. (2014) *Critical review, with an optimistic outlook, on Boron Neutron Capture Therapy (BNCT)*, Applied Radiation and Isotopes 88:2-11, <https://doi.org/10.1016/j.apradiso.2013.11.109>.
- [11] Kawabata S., Suzuki M., Hirose K., Tanaka H., Kato T., Goto H., Narita Y. and Miyatake S-I. (2021) *Accelerator-based BNCT for patients with recurrent glioblastoma: a multicenter phase II study*, Neuro-Oncology Advances 3(1):vdab067. <https://doi.org/10.1093/noajnl/vdab067>
- [12] Malouff T. D., Seneviratne D. S., Ebner D. K., Stross W. C., Waddle M. R., Trifiletti D. M. and Krishnan S. (2021) *Boron neutron capture therapy: A review of clinical applications*, Frontiers in oncology 11:351. <https://doi.org/10.3389/fonc.2021.601820>
- [13] Godwin J.T., Farr L.E., Sweet W.H. and Robertson J.S. (1955), *Pathological study of eight patients with glioblastoma multiforme treated by neutron capture therapy using boron 10*. Cancer, 8:601-615. [https://doi.org/10.1002/1097-0142\(1955\)8:3<601::AID-CNCR2820080326>3.0.CO;2-R](https://doi.org/10.1002/1097-0142(1955)8:3<601::AID-CNCR2820080326>3.0.CO;2-R)
- [14] Kreiner A.J. (2012) *Accelerator-Based BNCT* in: Sauerwein W., Wittig A., Moss R., Nakagawa Y. (eds) *Neutron Capture Therapy: Principles and Applications*, Springer-Verlag Berlin Heidelberg. <https://doi.org/10.1007/978-3-642-31334-9>
- [15] Postuma I., González S.J., Herrera M., Provenzano L., and Ferrarini M., Magni C., Protti N., Fatemi S., Vercesi V., Battistoni G., Anselmi-Tamburini U., Hao Liu Y., Kankaanranta L., Koivunoro H., Altieri S. and Bortolussi S. (2002) *A Novel Approach to Design and Evaluate BNCT Neutron Beams Combining Physical, Radiobiological, and Dosimetric Figures of Merit*, Biology, 10(3):174. <https://doi.org/10.3390/biology10030174>
- [16] Postuma I. (2015) *Clinical application of accelerator-based Boron Neutron Capture Therapy: optimization of procedures, tailoring of a neutron beam and evaluation of its dosimetric performance*, Ph.D. Thesis, University of Pavia. <https://doi.org/10.13140/RG.2.1.3539.3680>
- [17] German R.M. (2001) *Sintering*, in: Jürgen Buschow J.K.H., Cahn R.W., Flemings M.C., Ilshner B., Kramer E.J., Mahajan S., Veyssi re P. (eds) *Encyclopedia of Materials: Science and Technology*, Elsevier. <https://doi.org/10.1016/B0-08-043152-6/01542-4>
- [18] Olevsky E.A. and Dudina D.V. (2018) *Field-Assisted Sintering - Science and Applications*, Springer. <https://doi.org/10.1007/978-3-319-76032-2>

BIBLIOGRAPHY

- [19] Lee G., Manière C., McKittrick J. and Olevsky E.A. (2019) *Electric current effects in spark plasma sintering: From the evidence of physical phenomenon to constitutive equation formulation*, Scripta Materialia 170:90-94. <https://doi.org/10.1016/j.scriptamat.2019.05.040>
- [20] Greenberg R.R., Bode P., De Nadai Fernandes E.A. (2011) *Neutron activation analysis: A primary method of measurement*, Spectrochimica Acta Part B: Atomic Spectroscopy, 66(3-4):193-241, <https://doi.org/10.1016/j.sab.2010.12.011>
- [21] Alloni D., Prata M., Salvini A., Ottolenghi A. (2015) *Neutron flux characterisation of the Pavia TRIGA Mark II research reactor for radiobiological and microdosimetric applications*, Radiation Protection Dosimetry 166(1-4):261-5. <https://doi.org/10.1093/rpd/ncv291>
- [22] LENA, Laboratorio di Energia Nucleare Applicata (1999) *Rapporto finale di sicurezza*, Technical report
- [23] EG&G ORTEC, *GammaVision* software version 5.10, ORTEC website accessed on 27 July 2021. <https://www.ortec-online.com/products/application-software/gammavision>
- [24] Jacob P., Debertain K., Miller K., Roed J., Saito K. and Sanderson D. (1994). *2. Basic Principles of Gamma-Ray Spectrometry*, Journal of the International Commission on Radiation Units and Measurements, vol.os27(2):4-14. <https://doi.org/10.1093/jicru/os27.2.4>
- [25] IUPAC (1997) *Compendium of Chemical Terminology, 2nd ed. (the "Gold Book")*, compiled by A.D. McNaught and A. Wilkinson, Blackwell Scientific Publications. Online version (2019-) created by S. J. Chalk. <https://doi.org/10.1351/goldbook>
- [26] Verheijke M.L. (1994) *Relation between the Høgdahl convention and the modified Westcott formalism for (n,γ) reactions with a pure 1/v_n cross-section behavior*, Journal of Radioanalytical and Nuclear Chemistry 183:293-299. <https://doi.org/10.1007/BF02037998>
- [27] Di Luzio M., Oddone M., Prata M. Alloni D., D'Agostino G. (2017) *Measurement of the neutron flux parameters f and α at the Pavia TRIGA Mark II reactor*, Journal of Radioanalytical and Nuclear Chemistry 312:75-80. <https://doi.org/10.1007/s10967-017-5191-4>
- [28] k_0 -Nuclear Data Subcommittee of k_0 -International Scientific Committee (2016) *Database of recommended k_0 -data*, accessed on 30 November 2018. www.kayzero.com/k0naa/k0naaorg/Nuclear_Data_SC/Entries/2016/1/11_New_k0-data_Library_2015.html

- [29] Mughabghab S.F. (2003) *Thermal neutron capture cross sections resonance integrals and g-factors (INDC(NDS)-440)*, International Atomic Energy Agency (IAEA). <http://www-nds.iaea.org/reports/indc-nds-440.pdf>
- [30] Magni C., Ferrarini M., Postuma I., Protti N., Fatemi S., Gong C., Anselmi-Tamburini U., Vercesi V., Battistoni G. and Bortolussi S. *Neutron activation and dosimetry studies for a clinical facility of Boron Neutron Capture Therapy*, Il Nuovo Cimento, accepted June 2021
- [31] Goorley T, James M, Booth T, Brown F, Bull J, Cox L.J., Durkee J., Elson J., Fensin M., Forster R.A., Hendricks J., Hughes H.G., Johns R., Kiedrowski B., Martz R., Mashnik S., McKinney G., Pelowitz D., Prael R., Sweezy J., Waters L., Wilcox T. and Zukaitis T. (2012) *Initial MCNP6 Release Overview* Nuclear Technology 180:3 298-315. <https://doi.org/10.13182/NT11-135>
- [32] Agosteo S., Colautti P., Esposito J., Fazzi A., Introini M.V. and Pola A. (2011) *Characterization of the energy distribution of neutrons generated by 5 MeV protons on a thick beryllium target at different emission angles*, Applied Radiation and Isotopes 69(12):1664-1667. <https://doi.org/10.1016/j.apradiso.2011.03.015>
- [33] Spierings A.B., Schneider M. and Eggenberger R. (2011) *Comparison of Density Measurement Techniques for Additive Manufactured Metallic Parts*, Rapid Prototyping Journal 17:380-386. <https://doi.org/10.1108/135525411111156504>
- [34] METTLER TOLEDO website, accessed on 27 July 2021. <https://www.mt.com/int/en/home.html>
- [35] Wang W., Sain M., Cooper P.A. (2006) *Study of moisture absorption in natural fiber plastic composites*, Composites Science and Technology 66(3-4):379-386. <https://doi.org/10.1016/j.compscitech.2005.07.027>.
- [36] Fratelli Galli[®] Laboratory & Industrial solutions website, accessed on 27 July 2021. <https://www.galli2europe.com/en/laboratory-ovens-industrial/>
- [37] ASTM (American Society for Testing and Materials) International website, accessed on 21 July 2021. <https://www.astm.org/>
- [38] Melnik L.A. and Krysenko D.A. (2019) *Ultrapure Water: Properties, Production, and Use*, Journal of Water Chemistry and Technology 41:143-150. <https://doi.org/10.3103/S1063455X19030020>
- [39] Gong Y., Grant D.J.W., Brittain H.G. (2007) *Principles of Solubility in: Augustijns P. and Brewster M.E. (eds) Solvent Systems and Their Selection in Pharmaceuticals and Biopharmaceuticals*, Springer New York. https://doi.org/10.1007/978-0-387-69154-1_1

BIBLIOGRAPHY

- [40] Technology Catalysts International (2004) *Delivery of Poorly Soluble or Poorly Permeable Drugs* report, 5th edition. <https://technology-catalysts.com/>
- [41] Vernon-Parry K. D. (2000) *Scanning electron microscopy: an introduction*, III-Vs Review, 13(4):40-44 [https://doi.org/10.1016/S0961-1290\(00\)80006-X](https://doi.org/10.1016/S0961-1290(00)80006-X)
- [42] Ul-Hamid A. (2018) *Sample Preparation in: A Beginners' Guide to Scanning Electron Microscopy*, Springer Cham. https://doi.org/10.1007/978-3-319-98482-7_8
- [43] BUEHLER GmbH Manuals, accessed 21 July 2021. <https://www.yumpu.com/en/document/view/4577440/buehlerr-alpha-beta-vectortm-grinder-buehler-gmbh>
- [44] Cressington Scientific Instruments UK website, accessed on 21 July 2021. <https://www.cressington.com/>
- [45] TESCAN website, accessed on 21 July 2021. <https://www.tescan.com/product/sem-for-materials-science-tescan-mira/>
- [46] Goldstein J.I., Newbury D.E., Michael J.R., Ritchie N.W.M., Scott J.H.J. and Joy D.C. (2018) *Scanning electron microscopy and x-ray microanalysis* 4th edition, Springer. <https://doi.org/10.1007/978-1-4939-6676-9>
- [47] WAB-GROUP website, accessed on 27 July 2021. <https://www.wab-group.com/en/mixing-technology/3d-shaker-mixer/product/turbula/>
- [48] FRITSCHE website, accessed on 27 July 2021. <https://www.fritsch-international.com/sample-preparation/milling/planetary-mills/details/product/pulverisette-7-premium-line/>
- [49] INSTRON website accessed 28 September 2021 <https://instron.com>
- [50] Służalec A. (1992) *Stress-Strain Curve* in: *Introduction to Nonlinear Thermomechanics: Theory and Finite-Element Solutions*, Springer London. <https://doi.org/10.1007/978-1-4471-1906-7>
- [51] Bortolussi S., Protti N., Ferrari M., Postuma I., Fatemi S., Prata M., Ballarini F., Carante M.P., Farias R., González S.J., Marrale M., Gallo S., Bartolotta A., Iacoviello G., Nigg D. and Altieri S. (2018) *Neutron flux and gamma dose measurement in the BNCT irradiation facility at the TRIGA reactor of the University of Pavia*, NIM-B 414:113-120. <https://doi.org/10.1016/j.nimb.2017.10.023>.
- [52] Di Luzio M., D'Agostino G., Oddone M. and Salvini A. (2019) *Vertical variations of flux parameters in irradiation channels at the TRIGA Mark II reactor of Pavia*, Progress in Nuclear Energy 113. <https://doi.org/10.1016/j.pnucene.2019.01.025>

- [53] Keaton J.R. (2018) *Young's Modulus* In: Bobrowsky P.T., Marker B. (eds) *Encyclopedia of Engineering Geology. Encyclopedia of Earth Sciences Series*, Springer, Cham. https://doi.org/10.1007/978-3-319-73568-9_298
- [54] Stefanini A.M., Fortuna G., Lunardi S. and Ricci R.A. (1995) *The Laboratori Nazionali di Legnaro*, Nuclear Physics News 5:2(9-22). <https://doi.org/10.1080/10506899508223918>
- [55] RAYLAB s.r.l. website url <https://www.raylab.solutions/>
- [56] Agosteo S., Fazzi A., Introini M.V., Lorenzoli M. and Pola A. (2016) *A telescope detection system for direct and high resolution spectrometry of intense neutron fields*, Radiation Measurements 85:1-17. DOI: <https://doi.org/10.1016/j.radmeas.2015.12.005>
- [57] Parisi G. (2019) *AlF₃-moderated neutron flux characterization by means of experiments and Monte Carlo simulations for BNCT applications*, Master Thesis, Politecnico di Torino
- [58] Parisi G., Pola A., Bortot D., Mazzucconi D., D'Angelo G., Magni C., Postuma I., Bortolussi S., Protti N., Altieri S., Anselmi-Tamburini U., Vercesi V. and Agosteo, *Development of the ACSpect neutron spectrometer: technological advance and response against an accelerator-based neutron beam* Radiation Measurements, submitted June 21
- [59] Pola A., Rastelli D., Treccani M., Pasquato S. and Bortot D. (2020) *DIAMON: A portable, real-time and direction-aware neutron spectrometer for field characterization and dosimetry*, Nuclear Instruments and Methods in Physics Research Section A: Accelerators, Spectrometers, Detectors and Associated Equipment 969(164078). DOI: <https://doi.org/10.1016/j.nima.2020.164078>
- [60] Valsecchi J. (2014) *Thermal and Epithermal neutron beam tailoring for BNCT research at CN proton accelerator of INFN Legnaro National Laboratories*, MSc Thesis, University of Pavia
- [61] Agosteo S., D'Angelo G., Fazzi A., Para A.F., Pola A. and Zotto P. (2007) *Neutron spectrometry with a monolithic silicon telescope*, Radiation Protection Dosimetry. 2007;126(1-4):210-7. <https://doi.org/10.1093/rpd/ncm044>
- [62] Sang In K., Bong Hwan K., Jang Lyul K. and Jung Il L. (2015) *A review of neutron scattering correction for the calibration of neutron survey meters using the shadow cone method*, Nuclear Engineering and Technology 47(7): 939-944. <https://doi.org/10.1016/j.net.2015.07.005>
- [63] Howard W.B., Grimes S.M., Massey T.N., Al-Quraishi S.I., Jacobs D.K., Brient C.E. and Yanch J.C. (2001) *Measurement of the Thick-Target ⁹Be(p,n) Neutron Energy Spectra*, Nuclear Science and Engineering 138:2,145-160. <https://doi.org/10.13182/NSE01-A2206>

- [64] Esposito J., Colautti P., Fabritsiev S., Gervash A., Giniyatulin R., Lomasov V.N., Makhankov A., Mazul I., Pisent A., Pokrovsky A., Rumyantsev M., Tanchuk V. and Tecchio L. (2009) *Be target development for the accelerator-based SPES-BNCT facility at INFN Legnaro*, Applied Radiation and Isotopes 67(7–8):S270-S273. <https://doi.org/10.1016/j.apradiso.2009.03.085>
- [65] Magni C., Postuma I., Ferrarini M., Protti N., Fatemi S., Gong C., Anselmi-Tamburini U., Vercesi V., Battistoni G., Altieri S. and Bortolussi S. (2020) *Design of a BNCT irradiation room based on proton accelerator and beryllium target*, Applied Radiation and Isotope 165(109314). <https://doi.org/10.1016/j.apradiso.2020.109314>
- [66] Ferrari A., Sala P.R., Fassò A., Ranft J. (2005) *FLUKA: a multi-particle transport code*, CERN-2005-10 (2005), INFN/TC_05/11, SLAC-R-773. <https://doi.org/10.2172/877507>
- [67] Sato T., Iwamoto Y., Hashimoto S., Ogawa T., Furuta T., Abe S., Kai T., Tsai P.-E., Matsuda N., Iwase H., Shigyo N., Sihver L. and Niita K. (2018) *Features of Particle and Heavy Ion Transport code System (PHITS) version 3.02*, Journal of Nuclear Science and Technology. 55:1-7. <https://doi.org/10.1080/00223131.2017.1419890>
- [68] Chu S.Y.F., Ekström S.Y.F. and Firestone R.B., *The Lund/LBNL Nuclear Data Search*, version 2.0. <http://nucleardata.nuclear.lu.se/toi/>
- [69] Bortolussi S., Postuma I., Protti N., Provenzano L., Ferrari C., Cansolino L., Dionigi P., Galasso O., Gasparini G., Altieri S., Miyatake S-I. and González S. (2017) *Understanding the potentiality of accelerator based-boron neutron capture therapy for osteosarcoma: Dosimetry assessment based on the reported clinical experience* Radiation Oncology 12. <https://doi.org/10.1186/s13014-017-0860-6>
- [70] Leone J., Furler M., Oakley M., Caracappa P., Wan, B., and Xu X G. (2005) *Dose Mapping Using MCNP5 Mesh Tallies*, Health Physics 88(2):S31-S33. <https://doi.org/10.1097/01.HP.0000147793.62405.4c>
- [71] Woodward H.Q., White D.R. (1986) *The composition of body tissues*, British Journal of Radiology, 59:1209–19. <https://doi.org/10.1259/0007-1285-59-708-1209>
- [72] Hanaoka K., Watabe T., Naka S., Kanai Y., Ikeda H., Horitsugi G., Kato H., Isohashi K. and Shimosegawa E. (2014) *FBPA PET in boron neutron capture therapy for cancer: Prediction of (^{10}B) concentration in the tumor and normal tissue in a rat xenograft model* EJNMMI Research 4(70). <https://doi.org/10.1186/s13550-014-0070-2>

- [73] Shimosegawa E., Isohashi K., Naka S., Horitsugi G. (2016) *Assessment of ^{10}B concentration in boron neutron capture therapy: Potential of image-guided therapy using ^{18}F BPA PET* *Annals of Nuclear Medicine*. <https://doi.org/10.1007/s12149-016-1121-8>
- [74] Hendricks J.S. (1980) *Calculation of cell volumes and surface areas in MCNP*, LA-8113-MS report. <https://doi.org/10.2172/5724266>.
- [75] Heidenreich P.A., Kapoor J.R. (2014) *Radiation induced heart disease*, *Heart* 2009;95:252-258. <http://dx.doi.org/10.1136/hrt.2008.149088>
- [76] Selwyn A.P. (1983) *The cardiovascular system and radiation*, *Lancet* Jul16;2(8342):152-4. [https://doi.org/10.1016/s0140-6736\(83\)90130-7](https://doi.org/10.1016/s0140-6736(83)90130-7)
- [77] Yusuf S.W., Sami S., Daher I.N. (2011) Radiation-induced heart disease: a clinical update, *Cardiology Research and Practice* 2011(317659):9. <https://doi.org/10.4061/2011/317659>
- [78] Heidenreich P.A., Hancock S.L., Lee B.K., Mariscal C.S. and Schnittger I. (2003) *Asymptomatic cardiac disease following mediastinal irradiation* *Journal of the American College of Cardiology* Aug20;42(4):743-9. [https://doi.org/10.1016/s0735-1097\(03\)00759-9](https://doi.org/10.1016/s0735-1097(03)00759-9)
- [79] Jacobse J.N., Duane F.K., Boekel N.B., Schaapveld M., Hauptmann M., Hooning M.J., Seynaeve C.M., Baaijens M., Gietema J.A., Darby S.C., van Leeuwen F.E., Aleman B. and Taylor C. W. (2019) *Radiation Dose-Response for Risk of Myocardial Infarction in Breast Cancer Survivors*, *International Journal of Radiation Oncology, Biology, Physics*, 103(3):595–604. <https://doi.org/10.1016/j.ijrobp.2018.10.025>
- [80] Fowler J.F. (1989) *The linear-quadratic formula and progress in fractionated radiotherapy*, *British Journal of Radiology* 62(740):679-94. <https://doi.org/10.1259/0007-1285-62-740-679>
- [81] ICRP (2003) *Relative Biological Effectiveness (RBE), Quality Factor (Q), and Radiation Weighting Factor (w_R)* ICRP Publication 92. *Ann. ICRP* 33 (4). <https://www.icrp.org/publication.asp?id=ICRP%20Publication%2092>
- [82] Coderre J. and Morris G. (1999) *The Radiation Biology of Boron Neutron Capture Therapy*, *Radiation Research* 151(1):1-18. <https://doi.org/10.2307/3579742>
- [83] González S.J. and Santa Cruz G.A. (2012) *The photon-isoeffective dose in boron neutron capture therapy*, *Radiation Research* Dec;178(6):609-21. <https://doi.org/10.1667/RR2944.1>
- [84] González S.J., Pozzi E.C.C., Monti Hughes A., Provenzano L., Koivunoro H., Carando D.G., Thorp S.I., Casal M.R., Bortolussi S., Trivillin V.A., Garabalino

BIBLIOGRAPHY

- M.A., Curotto P., Heber E.M., Santa Cruz G.A., Kankaanranta L., Joensuu H. and Schwint A.E. (2017) *Photon iso-effective dose for cancer treatment with mixed field radiation based on dose-response assessment from human and an animal model: clinical application to boron neutron capture therapy for head and neck cancer*, *Physics in Medicine and Biology* 62(20):7938-7958. <https://doi.org/10.1088/1361-6560/aa8986>
- [85] Muhammad W., Hussain A. and Maqbool M. (2017) *Basic Concepts in Radiation Dosimetry*, in: *An Introduction to Medical Physics*, Maqbool M. (editor), Springer. https://doi.org/10.1007/978-3-319-61540-0_2
- [86] Attix F.H. (1986) *Introduction to Radiological Physics and Radiation Dosimetry*, Wiley ed. <https://doi.org/10.1002/9783527617135>
- [87] Barschall H.H., Chadwick M.B., Jones D.T.L., Meulders J.P., Schuhmacher H. and Young P.G. (2000) *ICRU Report 63*, *Journal of the International Commission on Radiation Units and Measurements Volume os32(2)*. <https://doi.org/10.1093/jicru/os32.2.Report63>
- [88] Goorley J.T., Kiger W.S. III and Zamenhof R.G. (2002) *Reference Dosimetry Calculations for Neutron Capture Therapy with Comparison of Analytical and Voxel Models*, *Medical Physics*, 29(2):145-56. <https://doi.org/10.1118/1.1428758>
- [89] ICRP, International Commission on Radiation Protection (2010) *Conversion Coefficients for Radiological Protection Quantities for External Radiation Exposures*, ICRP Publication 116, *Ann. ICRP* 40(2-5). <https://www.icrp.org/publication.asp?id=icrp%20publication%20116>
- [90] Burlin T.E., Bengtsson G., Chilton A.B., Drexler G., Harvey J.R., Portal G., Thomas R.H. and Wagner S.R. (1988) *ICRU Report 43*, *Journal of the International Commission on Radiation Units and Measurements Volume os22(2)*. <https://doi.org/10.1093/jicru/os22.2.Report43>
- [91] Wyckoff H.O., Allisy A., Fränz H., Jennings W.A., Kellerer A.M., Lidén K. and Rossi H.H. (1980) *ICRU Report 33*, *Journal of the International Commission on Radiation Units and Measurements, Volume os17(2)*. <https://doi.org/10.1093/jicru/os17.2.Report33>
- [92] ICRP (2007) *The 2007 Recommendations of the International Commission on Radiological Protection*, ICRP Publication 103. *Ann. ICRP* 37 (2-4). <https://www.icrp.org/publication.asp?id=ICRP%20Publication%20103>
- [93] Oberhofer M. (1991) *Advances in Radiation Protection*, Kluwer Academic Publishers. <https://www.springer.com/gp/book/9780792312321>
- [94] Pelliccioni M. (1989) *Fondamenti Fisici della Radioprotezione*, Pitagora Editrice Bologna

- [95] Ratliff H.N., Matsuda N., Abe S., Miura T., Furuta T., Iwamoto Y., Sato T. (2020) *Modernization of the DCHAIN-PHITS activation code with new features and updated data libraries*, Nuclear Instruments and Methods in Physics Research Section B: Beam Interactions with Materials and Atoms, 484:29-41. <https://doi.org/10.1016/j.nimb.2020.10.005>
- [96] Kreiner A.J., Bergueiro J., Cartelli D., Baldo M., Castell W., Asoia J.G, Padulo J., Suárez Sandín J.C., Igarzabal M., Erhardt J., Mercuri D., Valda, Minsky D.M., Debray M.E., Somacal H.R., Capoulat M.E., Herrera M.S, del Grosso M.F., Gagetti L., Anzorena M.S., Canepa N., Real N., Gun M. and Tacca H. (2016), *Present status of Accelerator-Based BNCT*, Reports of Practical Oncology & Radiotherapy 21(2):95-101. <https://doi.org/10.1016/j.rpor.2014.11.004>
- [97] Orecchia R., Zurlo A., Loasses A., Krenqli M., Tosi G., Zurrída S., Zucali P. and Veronesi U. (1998) *Particle beam therapy (hadrontherapy): basis for interest and clinical experience* European Journal of Cancer Mar;34(4):459-68. [https://doi.org/10.1016/s0959-8049\(97\)10044-2](https://doi.org/10.1016/s0959-8049(97)10044-2)
- [98] Sigmund P. (2006) *Particle Penetration and Radiation Effects: General Aspects and Stopping of Swift Point Charges*, Springer-Verlag Berlin Heidelberg. <https://doi.org/10.1007/3-540-31718-X>
- [99] Scharadt D., Elsässer T. and Schulz-Ertner D. (2010) *Heavy-ion tumor therapy: Physical and radiobiological benefits*, Reviews of Modern Physics 82(1):383-425. <https://doi.org/10.1103/RevModPhys.82.383>
- [100] Mizoe J-e., Hasegawa A. Jingu K., Takagi R., Bessyo H., Morikawa T., Tonoki M., Tsuji H., Kamada T., Tsujii H. and Okamoto Y. (2012) *Results of carbon ion radiotherapy for head and neck cancer*, Radiotherapy and Oncology 103(1):32-37. <https://doi.org/10.1016/j.radonc.2011.12.013>
- [101] Koivunoro H., Kankaanranta L., Seppälä T., Haapaniemi A., Mäkitie A., and Joensuu H. (2019) *Boron neutron capture therapy for locally recurrent head and neck squamous cell carcinoma: An analysis of dose response and survival*, Radiotherapy and Oncology, 137, 153-158. <https://doi.org/10.1016/j.radonc.2019.04.033>
- [102] Suzuki Minoru (2020) *Boron neutron capture therapy (BNCT): a unique role in radiotherapy with a view to entering the accelerator-based BNCT era*, International journal of clinical oncology,25(1):43-50. <https://doi.org/10.1007/s10147-019-01480-4>
- [103] Wang L-W., Liu Y-W H., Chou F-I. and Jiang S-H. (2018) *Clinical trials for treating recurrent head and neck cancer with boron neutron capture therapy using the Tsing-Hua Open Pool Reactor*, Cancer Communications,38(1) 37. <https://doi.org/10.1186/s40880-018-0295-y>

BIBLIOGRAPHY

- [104] Aihara T, Morita N, Kamitani N, Kumada H, Ono K, Hiratsuka J, Harada T. (2014) *BNCT for advanced or recurrent head and neck cancer*, Applied Radiation and Isotopes, 12-5. <https://doi.org/10.1016/j.apradiso.2014.04.007>
- [105] Burnet N. G., Thomas S. J., Burton K. E. and Jefferies, S. J. (2004) *Defining the tumour and target volumes for radiotherapy*, Cancer imaging: the official publication of the International Cancer Imaging Society, 4(2):153–161. <https://doi.org/10.1102/1470-7330.2004.0054>
- [106] Kato I., Ono K., Sakurai Y., Ohmae M., Maruhashi A., Imahori Y., Kirihata M., Nakazawa M., Yura Y. (2004) *Effectiveness of BNCT for recurrent head and neck malignancies*, Applied Radiation and Isotopes 61(5), 1069-73. <https://doi.org/10.1016/j.apradiso.2004.05.059>
- [107] Zaider M. and Hanin L. (2011) *Tumor control probability in radiation treatment*, Medical Physics 38(2):574-83. <https://doi.org/10.1118/1.3521406>
- [108] Heber E.M., Trivillin V.A., Nigg D.W., Itoiz M.E., Gonzalez B.N., Rebagliati R.J., Batistoni D., Kreimann E.L. and Schwint A.E. (2006) *Homogeneous boron targeting of heterogeneous tumors for boron neutron capture therapy (BNCT): chemical analyses in the hamster cheek pouch oral cancer model*, Archives of Oral Biology 51(10):922-9. <https://doi.org/10.1016/j.archoralbio.2006.03.015>
- [109] Coderre J.A., Makar M.S., Micca P.L., Nawrocky M., Liu H.B., Joel D.D., Slatkin D.N. and Amols H.I. (1993) *Derivations of relative biological effectiveness for the high-LET radiations produced during Boron Neutron Capture irradiations of the 9L rat gliosarcoma in vitro and in vivo*, International Journal of Radiation Oncology, Biology, Physics 27:1121-1129. [https://doi.org/10.1016/0360-3016\(93\)90533-2](https://doi.org/10.1016/0360-3016(93)90533-2)
- [110] Brenner D.J., Hlatky L.R., Hahnfeldt P.J., Huang Y. and Sachs R.K. (1998) *The linear-quadratic model and most other common radiobiological models result in similar predictions of time-dose relationships*, Radiation Research 150(1):83-91. <https://doi.org/10.2307/3579648>
- [111] PYTHON™ website, accessed on 20 September 2021. <https://www.python.org>
- [112] González S.J., Carando D.G., Santa Cruz G.A. and Zamenhof R.G. (2005) *Voxel model in BNCT treatment planning: performance analysis and improvements*, Physics in Medicine and Biology 50:441-458. <https://doi.org/10.1088/0031-9155/50/3/004>
- [113] Gonzalez S.J., Santa Cruz G.A. and Yam C.S. (2003) *NCTPlan The new PC version of MacNCTPlan improvements and validation of the treatment planning system* AATN 2001: 28 Annual meeting of the Argentine Association of Nuclear Technology.

- [114] Provenzano L. (2020) *Research and development in BNCT for the treatment of new pathologies*, PhD Thesis, Universidad de San Martín, Buenos Aires, Argentina
- [115] Suzuki M., Kato I., Aihara T., Hiratsuka J., Yoshimura K., Niimi M., Kimura Y., Ariyoshi Y., Haginomori S., Sakurai Y., Kinashi Y., Masunaga S., Fukushima M., Ono K., Maruhashi A. (2014) *Boron neutron capture therapy outcomes for advanced or recurrent head and neck cancer*, Journal of Radiation Research 1;55(1):146-53. <https://doi.org/10.1093/jrr/rrt098>
- [116] Kankaanranta L., Seppälä T., Koivunoro H., Saarilahti K., Atula T., Collan J., Salli E., Kortensniemi M., Uusi-Simola J., Välimäki P., Mäkitie A., Seppänen M., Minn H., Revitzer H., Kouri M., Kotiluoto P., Seren T., Auterinen I., Savolainen S. and Joensuu H. (2012) *Boron neutron capture therapy in the treatment of locally recurred head-and-neck cancer: final analysis of a phase I/II trial*, International Journal of Radiation Oncology, Biology, Physics 1;82(1):e67-75. <https://doi.org/10.1016/j.ijrobp.2010.09.057>
- [117] Heber E., Kueffe P., Lee M., Hawthorne M., Garabalino M., Molinari A., Nigg D., Bauer W., Monti Hughes A., Pozzi E., Trivillin V. and Schwint A.E. (2012) *Boron delivery with liposomes for boron neutron capture therapy (BNCT): Biodistribution studies in an experimental model of oral cancer demonstrating therapeutic potential*, Radiation and environmental biophysics 51:195-204. <https://doi.org/10.1007/s00411-011-0399-0>
- [118] Pedrosa-Rivera M., Praena J., Porras I., Ruiz-Magaña M.J. and Ruiz-Ruiz C. (2020) *A simple approximation for the evaluation of the photon iso-effective dose in Boron Neutron Capture Therapy based on dose-independent weighting factors* Applied Radiation and Isotopes 157:109018. <https://doi.org/10.1016/j.apradiso.2019.109018>
- [119] Morris G.M., Coderre J.A., Hopewell J.A., Micca P.L., Nawrocky M.M., Liu H.B. and Bywaters A. (1994) *Response of the central nervous system to boron neutron capture irradiation: evaluation using rat spinal cord model*, Radiotherapy and Oncology 32(3):249-255. [https://doi.org/10.1016/0167-8140\(94\)90024-8](https://doi.org/10.1016/0167-8140(94)90024-8)
- [120] Monti-Hughes A., Aromando R.F., Pérez M.A., Schwint A.E. and Itoiz M.E. (2015) *The hamster cheek pouch model for field cancerization studies* Periodontology2000 67:292-311. DOI:<https://doi.org/10.1111/prd.12066>
- [121] Bentzen S.M., Constine L.S., Deasy J.O., Eisbruch A., Jackson A., Marks L.B., Ten Haken R.K. and Yorke E.D. (2010) *Quantitative Analyses of Normal Tissue Effects in the Clinic (QUANTEC): An Introduction to the Scientific Issues*, International Journal of Radiation Oncology*Biophysics*Physics 76(3) Supplement. DOI: <https://doi.org/10.1016/j.ijrobp.2009.09.040>

- [122] Kato I., Fujita Y., Maruhashi A., Kumada H., Ohmae M., Kirihata M., Imahori Y., Suzuki M., Sakrai Y., Sumi T., Iwai S., Nakazawa M., Murata I., Miyamaru H. and Ono K. (2009) *Effectiveness of boron neutron capture therapy for recurrent head and neck malignancies* Applied Radiation and Isotopes, 67(7-8):S37-S42. <https://doi.org/10.1016/j.apradiso.2009.03.103>
- [123] Kankaanranta L., Seppälä T., Koivunoro H., Saarilahti K., Atula T., Collan J., Salli E., Kortensniemi M., Uusi-Simola J., Välimäki P., Mäkitie A., Seppänen M., Minn H., Revitzer H., Kouri M., Kotiluoto P., Seren T., Auterinen I., Savolainen S. and Joensuu H. (2012) *Boron neutron capture therapy in the treatment of locally recurred head-and-neck cancer: final analysis of a phase I/II trial*, International Journal of Radiation Oncology* Biology* Physics, 82(1):e67-e75. <https://doi.org/10.1016/j.ijrobp.2010.09.057>
- [124] Wang LW, Chen YW, Ho CY., Hsueh Liu YW., Chou FI., Liu YH., Liu HM., Peir JJ., Jiang SH., Chang CW., Liu CS., Lin KH., Wang SJ., Chu PY., Lo WL., Kao SY. and Yen SH. (2016) *Fractionated boron neutron capture therapy in locally recurrent head and neck cancer: a prospective phase I/II trial*, International Journal of Radiation Oncology* Biology* Physics, 95(1):396-403. <https://doi.org/10.1016/j.ijrobp.2016.02.028>
- [125] González S.J., Carando D.G. *A general tumour control probability model for non-uniform dose distributions*, Mathematical medicine and biology: a journal of the IMA Jun;25(2):171-84. <https://doi.org/10.1093/imammb/dqn012>
- [126] Rwigema J.C., Heron D.E., Ferris R.L., Andrade R.S., Gibson M.K., Yang Y., Ozhasoglu C., Argiris A.E., Grandis J.R. and Burton S.A. (2011) *The impact of tumor volume and radiotherapy dose on outcome in previously irradiated recurrent squamous cell carcinoma of the head and neck treated with stereotactic body radiation therapy*, American Journal of Clinical Oncology. <https://doi.org/10.1097/COC.0b013e3181e84dc0>
- [127] Perotti Bernardini G., Bortolussi S., Koivunoro H., Provenzano L., Ferrari C., Cansolino L., Postuma I., Grenman R., Kankaanranta L., Joensuu H. and González S.J. *Comparison of photon isoeffective dose models based on in-vitro and in in-vivo radiobiological data for head and neck cancer* (under preparation) - internal communication
- [128] Drzymala R.E., Mohan R., Brewster L., Chu J., et al. (1991) *Dose-volume histograms*, International Journal of Radiation Oncology, Biology, Physics 21(1):71-8. [https://doi.org/10.1016/0360-3016\(91\)90168-4](https://doi.org/10.1016/0360-3016(91)90168-4)
- [129] Kessel H., Hennicke J., Kirchner R. and Kessel T. (2010) *Spark Plasma Sintering (FAST/SPS) of Novel Materials - Taking the Next Step Forward to Industrial Production* in: *Advanced Processing and Manufacturing Technologies for Structural and Multifunctional Materials IV*, Tatsuki Ohji, Sanjay Mathur, Mrityunjay Singh (eds), Wiley. <https://doi.org/10.1002/9780470944066.ch12>

- [130] SIRAS S.a.S. website <https://www.sirasoleodinamica.it/>
- [131] TECNEL s.r.l. website <http://www.tecnelpv.it/>
- [132] Esposito J., Bettoni D., Boschi A., Calderolla M., Cisternino S., Fiorentini G., Keppel G., Martini P., Maggiore M., Mou L., Pasquali M., Pranovi L., Pupillo G., Rossi Alvarez C., Sarchiapone L., Sciacca G., Skliarova H., Favaron P., Lombardi A., Antonini P., Duatti A. (2019) *LARAMED: A Laboratory for Radioisotopes of Medical Interest*, *Molecules* 24(1):20. <https://doi.org/10.3390/molecules24010020>
- [133] Skliarova H., Cisternino S., Cicoria G., Cazzola E., Gorgoni G., Marengo M. and Esposito J. (2020) *Cyclotron solid targets preparation for medical radionuclides production in the framework of LARAMED project*, *Journal of Physics Conference Series* 1548(012022). <https://doi.org/10.1088/1742-6596/1548/1/012022>
- [134] Cisternino S., Anselmi-Tamburini U., Magni C., Bortolussi S., Vercesi V. and Esposito J. (2021) *Spark Plasma Sintering machine for LARAMED project: updates*, INFN-LNL Report 262, LNL (Legnaro National Laboratories of INFN) Annual Report 2020. <http://www.lnl.infn.it/~annrep>

List of Publications

- Postuma I., González S.J., Herrera M., Provenzano L., Ferrarini M., Magni C., Protti N., Fatemi S., Vercesi V., Battistoni G., Anselmi-Tamburini U., Hao Liu Y., Kankaanranta L., Koivunoro H., Altieri S. and Bortolussi S., “A Novel Approach to Design and Evaluate BNCT Neutron Beams Combining Physical, Radiobiological and Dosimetric Figures of Merit”, *Biology* 2021, 10, 174, Feb. 21
- Postuma I., Sommi P., Vitali A., Shu D., di Martino G., Cansolino L., Ferrari C., Ricci V., Magni C., Protti N., Fatemi S., Anselmi-Tamburini U., Bortolussi S. and Altieri S., “Colocalization of tracks from boron neutron capture reactions and images of isolated cells”, *Applied Radiation and Isotopes*, vol. 167 (109353), Jan. 21
- Magni C., Postuma I., Ferrarini M., Protti N., Fatemi S., Gong C., Anselmi-Tamburini U., Vercesi V., Battistoni G., Altieri S. and Bortolussi S., “Design of a BNCT irradiation room based on proton accelerator and beryllium target”, *Applied Radiation and Isotopes*, vol. 165 (109314), Nov. 20
- Fatemi S., Gong C., Bortolussi S., Magni C., Postuma I., Bettelli M., Benassi G., Zambelli N., Zappettini A., Tang X.B., Altieri S. and Protti N., “Innovative 3D sensitive CdZnTe solid state detector for dose monitoring in Boron Neutron Capture Therapy (BNCT)”, *Nuclear Instruments and Methods in Physics Research*, vol. 936 (pages 50-51), Aug. 2019
- Altieri S., Fatemi S., Bortolussi S., Magni C., Postuma I. and Protti N., “Preliminary Monte Carlo study of CZT response to BNCT (n+ γ) background”, *Il Nuovo Cimento* 41 C (208), May 2019
- Bortolussi S., Postuma I., Protti N., Fatemi S., Magni C., González S. and Altieri S., “EP-1885 Neutron beam design and dosimetric evaluation for accelerator-based Boron Neutron Capture Therapy”, poster-ESTRO-28, Abstract in Radiotherapy and Oncology, April 2019 133:S1024

- Magni C., “Studi di radioprotezione per il progetto di una sala di trattamento di Boron Neutron Capture Therapy (BNCT) basata su acceleratore”, in “Radiazioni - Ricerca e Applicazioni”, vol XXI n. 2 e 3, 2018

- Fatemi S., Gong C., Bortolussi S., Magni C., Postuma I., Tang X., Altieri S. and Protti N., “Preliminary Monte Carlo simulations of a SPECT system based on CdZnTe detectors for real time BNCT dose monitoring”, Conference paper (2018 IEEE Nuclear Science Symposium and Medical Imaging Conference (NSS/MIC))

- Fatemi S., Bortolussi S., Magni C., Postuma I., Bettelli M., Benassi G., Zambelli N., Zappettini A., Altieri S. and Protti N., “Prompt gamma tomography for BNCT-SPECT: a feasibility study using small animal phantoms”, Conference paper (2018 IEEE Nuclear Science Symposium and Medical Imaging Conference (NSS/MIC))

- Fatemi S., Abbene L., Principato F., Buttacavoli A., Auricchio N., Caroli E., Basili A., Zambelli N., Benassi G., Bettelli M., Zanettini S., Zappettini S., Bortolussi S., Magni C., Postuma I., Altieri S. and Protti N., “High performance 3D CZT spectro-imager for BNCT-SPECT: preliminary characterization”, Conference paper (2018 IEEE Nuclear Science Symposium and Medical Imaging Conference (NSS/MIC))

Reports:

- Cisternino S., Anselmi-Tamburini U., Magni C., Bortolussi S., Vercesi V. and Esposito J., “Spark Plasma Sintering machine for LARAMED project: updates”, INFN-LNL (Legnaro National Laboratories) Annual Report 2020

- Bortolussi S., Magni C., Postuma I., Protti N., Altieri S., Anselmi-Tamburini U., Vercesi V., Agosteo S., Pola A., Parisi G., Bortot D., Mazzucconi D., D’Angelo G., “Measurements of Neutron Spectra from Be(p,n) Reaction After Crossing Lithiated AlF₃ Moderator”, INFN-LNL (Legnaro National Laboratories) Annual Report 2019

Accepted:

- Magni C., Ferrarini M., Postuma I., Protti N., Fatemi S., Gong C., Anselmi-Tamburini U., Vercesi V., Battistoni G., Bortolussi S., “Neutron activation and dosimetry studies for a clinical facility of Boron Neutron Capture Therapy”, Il Nuovo Cimento, accepted June 2021

Submitted:

- Parisi G., Pola A., Bortot D., Mazzucconi D., D’Angelo G., Magni C., Postuma I., Bortolussi S., Protti N., Altieri S., Anselmi-Tamburini U., Vercesi V. and Agosteo S. “Development of the ACSpect neutron spectrometer: technological advance and response against an accelerator-based neutron beam” submitted to Radiation Measurements, June 21

- Magni C., “How radiation protection issues influence the design of a clinical facility for accelerator-based Boron Neutron Capture Therapy”, full-paper contribution for IRPA15, 15th International Congress of the International Radiation Protection Association, submitted to Journal of Radiological Protection, Apr 21

In progress:

- Magni C. et al., “Alliflu: a novel material for the Beam Shaping Assembly of an AB-BNCT clinical facility”

- Magni C. et al., “Multi-code Monte Carlo simulations for the treatment room of an accelerator-based Boron Neutron Capture Therapy clinical facility”

- Bortolussi S. et al., “Comparison of Carbon-ion treatment and BNCT in a clinical case of Head and Neck tumour”